Infinitely Disordered Critical Behavior in Higher Dimensional Quantum Systems

Ph.D. Dissertation

István Kovács

Advisor: Prof. Ferenc Iglói, D.Sc.
Consultant: Prof. emer. Péter Szépfalusy, D.Sc.
Institute for Solid State Physics and Optics
Wigner Research Centre for Physics
Hungarian Academy of Sciences

Eötvös Loránd University
Faculty of Science

Physics Doctoral School
Head of School: Prof. Ferenc Csikor, D.Sc.

Statistical Physics, Biophysics and
Physics of Quantum Systems Ph.D. Program
Program leader: Prof. Jenő Kürti, D.Sc.

Budapest, 2012

Contents

Introduction

Phase transitions are among the most striking phenomena of nature. While continuously changing the temperature, the physical properties of the system display a sudden change at a classical phase transition. At a continuous phase transition the degrees of freedom become macroscopically correlated at the critical point, thus the emerging singularities are powerful manifestations of *collective phenomena*. In this thesis we are going to study continuous *quantum phase transitions*, driven by quantum, rather than thermal fluctuations, originating from Heisenberg's uncertainty principle at $T = 0$. The most impressive property of continuous phase transitions is their universality: the critical behavior is insensitive to microscopic details, depending only on global characteristics, such as the number of spatial dimensions, the range of interactions and the symmetries of the system. Consequently, it is often sufficient to study a simplified model instead of a realistic system in order to obtain its critical properties. Since spatial inhomogeneity — modeled by time-independent, *quenched* disorder — is an inevitable feature of realistic systems, the question arises: Do we have to incorporate also quenched disorder in the models of critical phenomena, or is it just one of the irrelevant microscopic details? In fact, quenched disorder may dramatically change the critical behavior known in the *clean*, disorder-free system. A paradigmatic example of this phenomena is the quantum Ising model, known as the random transverse-field Ising model (RTIM) when supplemented with quenched disorder in the strength of the couplings. The quantum Ising model shows already in one dimension a second order phase transition, which belongs to the universality class of the two dimensional classical Ising model. Although the critical behavior is exactly known from Onsager's solution [1], it is not appropriate to describe the phase transition under the more realistic, disordered conditions. The shocking result is that in the presence of (even the weakest) quenched disorder, the critical behavior is completely different from the behavior of the clean model. The interplay between the emerging correlations and disorder fluctuations results in strong singularity of the thermodynamic quantities, as well as both the spatial and dynamical correlation functions. The profound effect of disorder extends also outside the critical point, in the so called Griffiths-phases, where the dynamical correlations are still long-ranged, in contrast to short-ranged spatial correlations.

Besides the quantum Ising model, there are many other physical systems, where disorder influences strongly the critical behavior, such as the one-dimensional Hubbard model [2], the Mott metal-insulator transition in 2D [3], diffusion in a random potential [4], localization of a random polymer at an interface [5], random exclusion process [6–8], trap models [9, 10], driven lattice gases and reaction diffusion models [11, 12], coarsening dynamics of classical spin

chains [13], quantum spin chains, ladders and higher dimensional quantum spin systems. For a detailed review see [14]. In the understanding of critical phenomena in disordered quantum systems the strong disorder renormalization group (SDRG) method played a crucial role. After the early works by McCoy and others [15–19], Fisher used the method to obtain exact analytical results for the one dimensional RTIM [20, 21]. As the most important finding, the critical point is described by an *infinite disorder fixed point* (IDFP), in which the strength of disorder grows without limits during renormalization [22], thus becomes dominant over quantum fluctuations. The fixed point found in 1D is characterized by ultraslow dynamical behavior, independent of the strength and form of the original disorder. Unfortunately, the application of the method in higher dimensions requires expensive numerical calculations, limited to small system sizes in 2D with relatively low accuracy [23–27]. The results show clear evidence of IDFP behavior in agreement with independent Monte Carlo simulations [28, 29]. In three dimensions, which is connected to real quantum magnets, no quantitative results have been published before us. Analysis of the numerical RG trajectories led to the conclusion that the critical behavior in this case is probably controlled by an IDFP [26], but no estimates about the critical exponents are available. In four and higher dimensions no numerical studies have been performed so far. The most exciting open question in the field is, whether the IDFP behavior is present in all higher dimensional systems, or the phenomena is a low-dimensional peculiarity, not existing above an upper critical dimension. In order to answer this question, our main goal is to determine the critical exponents and scaling functions in higher dimensions.

In addition, a major challenge in the theory of quantum phase transitions is to understand the characteristics, which are absent in classical physics. The *entanglement* of a subsystem with the rest of the system [30] is a prominent example, being extensively studied in various systems. Generally, it is also an interesting open question, how to quantify the entanglement in a general quantum state. However, in a pure state, e.g. in a non-degenerate ground state the *entanglement entropy* is known to be a good choice. In contrast to classical physics, the subsystem — containing for example only one spin — may be in multiple states also if the whole system has a unique wave function. We can imagine the entanglement entropy as the log-number of possible states of the subsystem (with a significant probability).

As a basic result in 1D, the entanglement entropy diverges logarithmically with the size of the subsystem at the critical point, with a universal prefactor [31–33]. Among several consequences, this can be used as a general tool to locate the critical points of 1D systems. Namely, even without knowing the nature of the phases and the correct order parameters characterizing them, we can find the critical points just by studying the entanglement entropy. Unfortunately, due to technical difficulties, there is almost complete lack of results on the entanglement entropy in higher dimensional interacting systems. An exception is the RTIM, where the SDRG method also permits the calculation of the entanglement entropy [34]. So far, the application of the method only succeeded up to two spatial dimensions, providing however conflicting interpretations due to small achievable system sizes [24, 27]. Thus, we also attempt to clarify the behavior of the entanglement entropy in the ground state of the RTIM in higher dimensions.

Although the dissertation uses the notions of the RTIM, a large class of other random quantum and classical stochastic systems are in the same universality class with an order parameter having a discrete symmetry [35, 36]. An extensively studied example is the nonequilibrium phase-transition of the Contact Process, which is a simple model of infection spreading [37]. Due to the similarity of the SDRG equations, our results can be readily applied also for this case.

The structure of the thesis is the following. First, we give a brief overview about the possible effects of disorder on classical and quantum phase transitions in Chapter 1, together with the most important theoretical approaches. In the thesis we apply the SDRG method, which is introduced in 1D and extended for higher dimensions in Chapter 2. Here we also present our own results, which led to a more efficient numerical SDRG algorithm. Earlier results and open questions regarding the IDFP behavior in higher dimensions are summarized in Chapter 3, including our results for ladders between 1D and 2D. In Chapters 4, 5 and 6 we present our numerical results for hypercubic lattices in 2, 3 and 4D. As the first step of our analysis, in Chapter 4 we describe how the critical point is located through the definition of finite-size critical points within the frame of the SDRG method. In addition to the accurate location of the critical point, our analysis also yields estimates for the ν correlation length exponent. The magnetic critical behavior around the critical point is studied in Chapter 5. In Chapter 6 we analyze the dynamical scaling both at and around the critical point. In order to gain further information about the upper critical dimension of the problem, we also carry out our analysis for Erdős-Rényi random graphs in Chapter 7, corresponding to the infinite dimensional limit. The open questions concerning the critical behavior of the entanglement entropy are addressed in Chapter 8 with our efficient cluster counting algorithm, described in the Appendix. Our results are summarized in Chapter 9.

The thesis is based on the following publications:

- I. A. Kovács and F. Iglói (2009) Critical behavior and entanglement of the random transverse-field Ising model between one and two dimensions, *Phys. Rev. B* **80**, 214416. `arXiv:0909.4442` Ref. [38]
- I. A. Kovács and F. Iglói (2010) Renormalization group study of the two-dimensional random transverse-field Ising model, *Phys. Rev. B* **82**, 054437. `arXiv:1005.4740` Ref. [39]
- I. A. Kovács and F. Iglói (2011) Infinite-disorder scaling of random quantum magnets in three and higher dimensions, *Phys. Rev. B* **83**, 174207. `arXiv:1010.2344` Ref. [40]
- I. A. Kovács and F. Iglói (2011) Renormalization group study of random quantum magnets, *J. Phys.: Condens. Matter* **23** 404204. `arXiv:1109.4267` Ref. [41]
- I. A. Kovács and F. Iglói (2012) Universal logarithmic terms in the entanglement entropy of 2d, 3d and 4d random transverse-field Ising models, *Europhysics Letters* **97**, 67009. `arXiv:1108.3942` Ref. [42]

In the thesis the following abbreviations are used:

IDFP	Infinite Disorder Fixed-Point
RG	Renormalization Group
RTIM	Random Transverse-field Ising Model
SDRG	Strong Disorder Renormalization Group

Chapter 1

Phase transitions in the presence of quenched disorder

'In the study of sciences, examples are
no less educational than rules.'
Sir Isaac Newton

1.1 Classical and quantum phase transitions

Examples of phase transitions can be found in various fields from the every-day examples of melting ice and paramagnet-to-ferromagnet transition of iron to the more exotic superfluid-insulator transition, also expanding the classical borders of physics, for instance in the complexity of algorithms, spreading of infections and financial crises. As a paradigmatic example of quantum magnets, we consider the transverse-field Ising model, with ferromagnetic ($J > 0$) interactions, given by the following Hamiltonian

$$\mathcal{H} = -J \sum_{\langle ij \rangle} \sigma_i^x \sigma_j^x - h \sum_i \sigma_i^z \ , \tag{1.1}$$

in terms of the Pauli-matrices, $\sigma_i^{x,z}$. Here i and j are sites of a d dimensional lattice with linear extension L. Quantum mechanics enters the scene via the non-commuting operators σ_i^x and σ_i^z for non-zero values of the h transverse magnetic field, while for $h = 0$ we recover the classical d dimensional Ising model. For large J couplings, the spins align in the x-direction, leading to a ferromagnetic, ordered phase with a spontaneous magnetization, m. The magnetic order can be destroyed by both thermal or quantum fluctuations, tuned by the T temperature or h transverse-field. This latter tends to destabilize the order by turning the spins out of the x to the z-direction. The resulted phase diagram is illustrated in Fig. 1.1 in higher ($d > 1$) dimensions[1]. With increasing quantum fluctuations, the phase transitions happens at lower and lower $T_c(h) \geq 0$ temperatures, until at $h = h_c$, the phase transition occurs at

[1] In $d = 1$, the transverse-field Ising model orders only for $T = 0\,\mathrm{K}$, thus the ferromagnetic region is restricted to the $T = 0\,\mathrm{K}$, $h < h_c$ line.

zero temperature. While using the $t = (T - T_c(h))/T_c(h)$ reduced temperature as the control parameter, one recovers the well-known critical behavior of the d dimensional classical Ising model for $h < h_c$ [43]. In terms of the renormalization group approach, the Ising fixed-point at $h = 0$ is attractive for the whole critical line with $T_c(h) > 0$. However, at $h = h_c$ a *quantum phase transition* takes place at $T = 0$, displaying a new kind of critical behavior, where quantum effects become dominant.

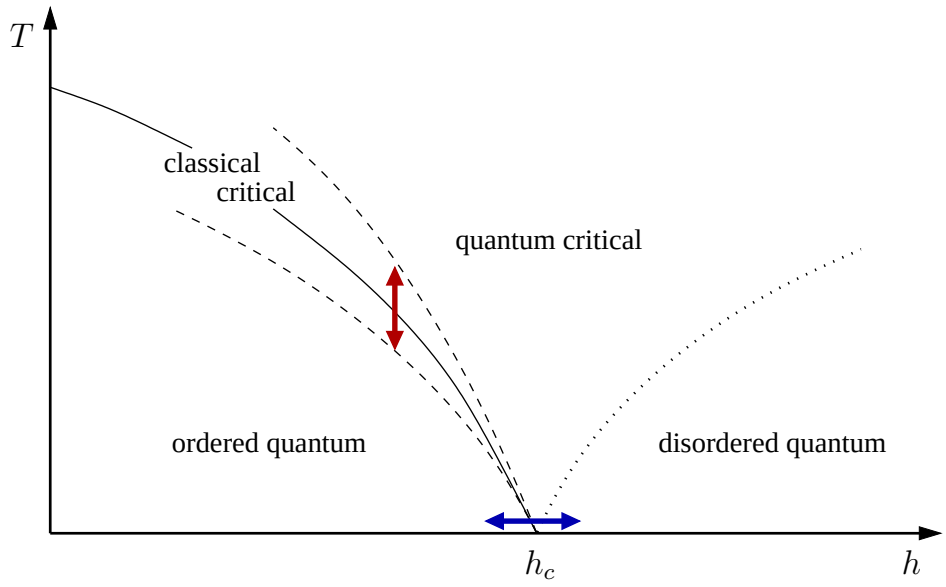

Figure 1.1: Schematic phase diagram of the transverse-field Ising model in higher dimensions. The classical and quantum phase transitions are illustrated by red ($T > 0\,\mathrm{K}$) and blue ($T = 0\,\mathrm{K}$) arrows between the ordered (ferromagnetic) and disordered (paramagnetic) phases. The dashed lines indicate cross-over behavior between different regimes.

Quantum phase transitions are among the fundamental problems of modern physics, the properties of which are studied in solid state physics, quantum field-theory, quantum information and statistical mechanics [44, 45]. There is a huge variety of experimental scenarios in which quantum phase transitions play an important role, among others rare-earth magnetic insulators [46], heavy-fermion compounds [47, 48], high-temperature superconductors [44, 49–51] and two-dimensional electron gases [52, 53].

In the following we restrict our studies to the vicinity of the quantum phase transition point at $T = 0\,\mathrm{K}$. The quantum critical behavior can be conveniently studied as the function of the $\delta = (h - h_c)/h_c$ control parameter. The critical exponents can be introduced analogously to the classical ($T_c(h) > 0\,\mathrm{K}$) case with $t \leftrightarrow \delta$. In the thermodynamic limit of $L \to \infty$ the magnetization vanishes continuously, as

$$m \sim \delta^{\beta} \tag{1.2}$$

for $\delta \geq 0$, while the ξ correlation length diverges as

$$\xi \sim |\delta|^{-\nu} , \tag{1.3}$$

as the function of the δ control parameter. However, in a numerical study one considers finite systems at $\delta = 0$ instead, in which case the magnetization vanishes as

$$m \sim L^{-x} \,, \tag{1.4}$$

with a critical exponent of $x = \beta/\nu$.

Generally, the quantum critical point also influences the finite temperature characteristics of the system in a wide region of the parameter space known as the *quantum critical region*, as illustrated in Fig. 1.1. Interestingly, one can also give an estimate for the border of the classical region by comparing the smallest energy gap $\epsilon = \hbar\omega$ to the thermal energy scale $k_{\mathrm{B}}T$. As an example of critical slowing down, the time-scale corresponding to the smallest excitation energy as $\tau \sim 1/\epsilon$ diverges at the critical point[2], as

$$\tau \sim \xi^z \,, \tag{1.5}$$

where z stands for the dynamical exponent [54–56]. Therefore, quantum mechanics is relevant for large scales, if $\hbar\omega \gg k_{\mathrm{B}}T$, corresponding to $\delta \gg T^{1/z\nu}$. Consequently, quantum mechanics becomes more and more stressed at lower temperatures, and becomes dominant at $T = 0\,\mathrm{K}$, where the classical region vanishes.

Quantum phase transitions in d dimensions are also related to $d+1$ dimensional classical phase transitions at finite temperature, but with a strong anisotropy. The extra spatial dimension in the classical system corresponds to the imaginary time (inverse temperature) dimension in the quantum system. This quantum-classical correspondence holds generally as shown by various ways, including the path integral formalism [57] and the Suzuki-Trotter formalism [58,59]. In this latter case the $Z = \mathrm{Tr}\, e^{-\frac{\hat{\mathcal{H}}}{k_{\mathrm{B}}T}}$ partition function is expressed as

$$Z = \mathrm{Tr} \lim_{\Delta\tau \to 0} \left(1 - \Delta\tau \hat{\mathcal{H}}\right)^{\frac{1}{k_{\mathrm{B}}T\Delta\tau}} \,. \tag{1.6}$$

Up to linear order in $\Delta\tau$, each $\left(1 - \Delta\tau\hat{\mathcal{H}}\right)$ term in this expression is equivalent to the transfer matrix in a classical $d+1$ dimensional system from a d dimensional layer to the next layer. The corresponding classical model is highly anisotropic, having much stronger couplings between the layers, than inside a layer. The transverse-field Ising model at $T = 0\,\mathrm{K}$ is equivalent to an infinite 2D Ising system with strong anisotropy. However, for the Ising model such anisotropy is irrelevant at the critical point [60,61], thus the transverse-field Ising model belongs to the universality class of the 2D homogeneous Ising model. Note that the temperatures of the quantum and classical models are not the same. While the temperature of the quantum system determines the size of the classical system in the imaginary time direction, the temperature of the classical system is analogous to the transverse-field in the quantum system.

[2] With other words, τ is the characteristic time scale on which the magnetization of the system turns over, also known as the dynamical correlation length.

1.2 Quenched disorder and the random transverse-field Ising model

The inhomogeneity (or disorder) present in condensed matter systems usually changes very slowly compared to the time scale on which the system is studied. The corresponding theoretical limit is known as *quenched disorder*, where randomness is completely time-independent. Glasses surrounding us are every-day life examples of this setting. The presence of quenched disorder in a system can give rise to completely new phenomena, like for instance the aging behavior in glassy systems [62, 63] or the Anderson localization [64].

Unlike in the case of glasses and spin-glasses, where frustration plays a crucial role, quenched disorder alone — without frustration — may have dramatic effects on the critical behavior, which became well understood in many one-dimensional systems by now. Our main goal is to understand the consequences of quenched disorder in the higher dimensional RTIM, defined by the Hamiltonian:

$$\mathcal{H} = -\sum_{\langle ij \rangle} J_{ij}\sigma_i^x\sigma_j^x - \sum_i h_i\sigma_i^z \ . \tag{1.7}$$

In contrast to Eq. (1.1), the $J_{ij} \geq 0$ couplings — and similarly the $h_i > 0$ transverse-fields — are now independent and identically distributed random variables. The quantum to classical mapping also works for the RTIM, leading to a 2D classical Ising model with layered randomness [65, 66]. This is known as the McCoy-Wu model and was the subject of intensive studies [15–19].

The RTIM has several experimental realizations, including order-disorder ferroelectrics ($K(H_xD_{1-x})_2PO_4$) [67–70], mixed hydrogen bonded ferroelectrics ($Rd_{1-x}(NH_4)_xH_2PO_4$) [71], quasi-1D Ising systems ($CoNb_2O_6$) [72] and dipolar magnets ($LiHo_xY_{1-x}F_4$). For a more extensive list, see [73].

Among these the most data is available about the $LiHo_xY_{1-x}F_4$ compound [74–77]. For $T < 11$K only the ground state doublet is populated, well described by Ising spins with $S = 1/2$. Between the Ising spins there is a dipole-coupling, thus the interaction is long-ranged. Applying a magnetic field H_t transverse to the Ising axis splits the ground-state doublet, therefore it acts as an effective transverse field of strength $h \sim H_t^2$ due to Zeeman interaction in second order of perturbation theory [78], for $H_t < 20$kOe. However, the quantum critical point is around a stronger $H_t \sim 50$kOe magnetic field, where the perturbation theory is not adequate [79]. Furthermore, the transverse field also induces a random longitudinal field [80–82] via the off-diagonal terms of the dipolar interaction, therefore there are several open questions both theoretically and experimentally about the rich low-temperature behavior of this compound. The observed exotic phenomena include 'spectral hole burning', entangled magnetic dipoles, quantum annealing, the quantum glass phase and the possible existence of an 'anti-glass' phase [79]. Recent experiments found strong evidence of Griffiths-singularities in the behavior of the susceptibility in this compound [83, 84], while studying its properties in the classical regime. The detailed effects of disorder may hopefully also in the quantum regime be discovered in the near future with the developed techniques.

In the theoretical investigations the interactions in the RTIM are generally assumed to be

short-ranged. While the properties of the system are tuned with the x parameter in the experiments, in the calculations it is more convenient to change the distributions of the J_{ij} couplings and the h_i transverse fields instead. For random ferromagnets we have $J_{ij} > 0$, whereas for spin-glasses — observed experimentally for e.g. $x = 0.167$ — there are both ferro- and antiferromagnetic couplings. This latter problem is very challenging, since the corresponding quantum state is the result of an interplay between quantum and disorder fluctuations, strong correlations and frustration. However, if the system is governed by an IDFP — as in the 1D RTIM —, then frustration becomes irrelevant [26], thus also the quantum spin-glass is expected to be governed by the critical exponents of the RTIM.

1.3 Essential features of infinitely disordered critical behavior

Before going into details about the theoretical approaches and results concerning the RTIM, let we briefly list here the most important properties of an IDFP.

- **Strong dynamical anisotropy:** The z dynamical exponent (introduced in Eq. (1.5)) is formally infinitely large. In other words, this corresponds to an *ultraslow*, so called *activated* dynamics: the dynamical processes, such as autocorrelations for random magnets take place in a logarithmic time-scale, characterized by a new ψ exponent as

$$\ln \tau \sim L^{\psi} \,, \tag{1.8}$$

  where L is the linear size of the system.

- **Broad distribution of physical quantities:** Physical quantities have a broad distribution even on a logarithmic scale. As a consequence, typical and average values are different and generally involve different type of singularities leading to a lack of self-averaging.

- **Dominant effect of rare regions:** The average value of a physical quantity is generally dominated by rare events (or rare regions of a large sample). In a rare event the physical quantity has a value of $\mathcal{O}(1)$ and to obtain the critical singularities it is generally enough to determine the fraction of rare events. Therefore calculations at these extraordinary infinite disorder fixed points are often comparatively 'easier', than at a conventional random fixed point characterized by a finite z dynamical exponent.

1.3.1 Classical example: Sinai walk in 1D

As mentioned already in the Introduction, there are also classical stochastic systems, described by an IDFP behavior. In order to illustrate this, let we consider the Sinai walk in 1D, which is a random walk in a random Brownian potential [85–90]. For recent reviews about the many developments in this field see [91–94]. The Sinai model appears in various contexts, among

others in the dynamics of domain-walls in the classical random field Ising chain [14] and the unzipping of DNA in the presence of an external force [95–98]. Remarkably, the Sinai walk is also intimately related to the 1D RTIM, as we discussed in e.g. [14] and [99].

The discrete model is defined on a lattice, where a particle at site i has a $w_{i,i+1} = \omega_i$ jumping probability to the right and a $w_{i,i-1} = 1-\omega_i$ to the left. The ω_i values are independent random numbers from the interval $(0,1)$. The random walk is recurrent only for $\overline{\ln \omega_i} = \overline{\ln(1-\omega_i)}$, which corresponds to the critical point. The control parameter is given by $\delta \sim \overline{\ln \omega_i} - \overline{\ln(1-\omega_i)}$. For $\delta > 0$ the particle moves to the right, while for $\delta < 0$ it moves to the left.

The homogeneous system shows usual diffusion at the critical point, with $\langle x(t)^2 \rangle \sim t$, where $z = 2$ and $\langle \dots \rangle$ stands for the ensemble average over different realizations. In strong contrast to this, in the presence of disorder ultraslow diffusion is found with $\overline{\langle x(t)^2 \rangle} \sim (\ln t)^4$ [87]. Here z is formally infinitely large, leading to a finite $\psi = 1/2$ exponent in Eq. (1.8). For small $\delta \neq 0$, anomalous diffusion is found with a δ-dependent finite $z(\delta) \sim 1/\delta$ dynamical exponent: $\langle x^2 \rangle \sim t^{2z}$. This type of scaling is a manifestation of the Griffiths-phase effects, discussed in the next section.

To gain more insight into the critical behavior with $\delta = 0$, it is useful to introduce another characteristic length scale as follows. The second important length $y(t) = x_1(t) - x_2(t)$ represents the distance between two *independent* particles diffusing in the same disordered sample from the same initial condition. In contrast to the clean case, where $y(t) \sim x(t) \sim \sqrt{t}$, complete localization is found in the disordered case for $\delta = 0$. This is manifested in the fact that the $y(t)$ variable remains finite even in the limit of $t \to \infty$, which is known as the Golosov-localization [100]. The reason behind this behavior is the existence of arbitrarily large rare regions, which acts like effective traps for the particles. These dominant traps in a given sample can be explicitly constructed with the strong disorder renormalization group method [14].

1.4 Theoretical methods to study the effects of quenched disorder

The broad field of disordered systems was the subject of intensive studies during the last 60 years, leading to various specific methods, for reviews see [101–105]. After briefly summarizing the main methods for disordered systems in this section, we show, why disorder-dependent real space RG procedures, especially, the strong disorder RG approaches are ideal tools to study systems in which disorder dominates at large scales over quantum, thermal, or stochastic fluctuations.

Historically, the first example was the Dyson-Schmidt method [106, 107], providing exact results for one dimensional systems, described by infinite products of random transfer matrices [103]. We also used this method recently to study the scaling of one dimensional quantum models in the off-critical region in [108] and in the M.Sc. thesis [99].

Since the pioneering work of Dyson a wide variety of methods developed, which may be classified into two categorizes. On the one hand there are approaches, which start by averaging

over disorder [109]. Besides the well-known replica method [102], there exist other approaches as well, such as the supersymmetric method [110] and the dynamical method [111]. After averaging over disorder, there are no more spatial heterogeneities, but the resulted homogeneous system contains new effective interactions. Intuitively, it is not surprising that we have to pay a huge price (e.g. replica symmetry breaking) for this initial simplification, if the system shows highly heterogeneous behavior on large scales. On the other hand, there are approaches which try to grasp directly the spatial heterogeneities of disorder, like certain famous arguments and various real-space renormalizations. We will now discuss both of them in more details.

1.4.1 Scaling arguments for disordered systems

The arguments which have played a great role in the understanding of disordered systems, may be divided into two classes based on the underlying idea.

Characterizing the importance of rare regions

In a disordered system there is an exponentially small, but nonzero probability for finding an arbitrarily large region having only strong couplings. These rare, strongly coupled regions may play a dominant role due to their very slow relaxation[3], leading to singular free-energy contributions. The resulted Griffiths singularities can be found outside the critical point, in the so called Griffiths-phases. In a classical equilibrium phase transition rare regions induce very slow dynamical relaxation [112–114], as well as essential singularities for the statics [115]. Even so, the generated thermodynamic singularities are so weak in this case that they possibly never become clearly observable [116]. However, we should not think that classical systems can not be interesting from this point of view. Non-equilibrium phase transitions, as for instance the Contact Process, may be much more sensitive to (uncorrelated) quenched disorder, than equilibrium models, as shown in [11, 12, 117–123].

In quantum systems the Griffiths effects are considerably stronger. This enhancement is due to the infinite size of the strongly coupled regions in the extra (imaginary time) dimension of the corresponding $d+1$ dimensional classical model, leading to even slower dynamics [124]. In the RTIM several thermodynamic quantities — including the average susceptibility — diverge even outside the critical point, where the correlation length is already finite. These singularities are connected to the behavior of the ϵ_L energy gap of the system with linear size, L.

- In the disordered Griffiths-phase (paramagnetic phase of the RTIM): A low-energy excitation is associated to a rare region of size ℓ, having $\sim \ell^d$ strong bonds and being locally in the ordered phase. Such a rare region appears with an exponentially small probability: $p(\ell) \sim \exp(-\alpha \ell^d)$ and the corresponding excitation energy is also exponentially small [14]: $\epsilon(\ell) \sim \exp(-\sigma \ell^d)$. The typical size of the largest rare region, ℓ^*, in a finite system with L^d sites follows from the relation: $L^d p(\ell^*) = \mathcal{O}(1)$. Consequently, the smallest excitations

[3]For instance, the flipping of the magnetization in such a strongly coupled region requires the coherent change over a large volume.

are typically $\epsilon_L = \epsilon(\ell^*)$, leading to

$$\epsilon_L \sim L^{-z} \,, \tag{1.9}$$

with a continuously varying $z = \dfrac{\sigma}{\alpha} d$ dynamical exponent.

- In the ordered Griffiths-phase (ferromagnetic phase of the RTIM): as following from a renormalization group argument [14], the effect of rare regions is generally smaller in the ordered phase, where there is also a giant magnetization cluster in the system. The excitation energy in the ordered phase is given by

$$\epsilon_L \sim \exp(-\sigma(\ln L)^{1/d}). \tag{1.10}$$

  Although in 1D we recover qualitatively the same scaling as in the disordered Griffiths-phase, in higher dimensions the difference is more stressed.

We shall study these scaling forms for the higher dimensional RTIM in Chapter 6.

There is another related approach, the Lifshitz argument [125–128], which allows to predict the essential singularities of the density of states near spectrum edges. The idea consists in identifying the disorder configurations that support states in this energy region and in estimating the probabilities of these favorable configurations. Indeed, both arguments are based on the notion of rare events: in any infinite configuration of disorder, there exist arbitrarily large ordered domains with exponentially small probabilities with a possibly large impact on the behavior.

So far we have assumed that these dominant rare regions preserve the sharpness of the phase transition. In the case of the RTIM and also in classical equilibrium continuous phase transitions, the transition remains sharp, because these special regions have finite extensions, thus can not undergo a true phase transition. The situation changes, when studying *correlated* randomness in d_r dimensions, which is above the d_l *lower critical dimension* of the system. For the RTIM $d_l = 1$, thus disordered regions with $d_r \geq 1$ are needed to destroy the sharp phase transition resulting in a so called *smeared phase transition* [129, 130].

While we are primarily interested in the effects of time-independent, quenched disorder, we have to mention the opposite limit of *annealed disorder*. In this case the time scale of the measurements is much longer, than the relaxation time of the disorder, thus randomness is effectively uncorrelated in time. Being less correlated, annealed disorder has a much weaker effect on phase transitions, unless introducing strong spatial correlations. Interestingly, spatially correlated annealed disorder can lead to analogous behavior to the case of spatially uncorrelated quenched disorder, with interchanged role of space and time directions, known as temporal Griffiths-phases [131].

Applying the law of large numbers

So far we have considered the arguments focusing on extreme events occurring in disordered systems. In contrast to these approaches, the following arguments refer to the *typical* fluctuations (of size $\sim \sqrt{N}$) for the sum of a large (N) number of independent random variables.

As an example, the Imry-Ma argument [13] allows to predict the presence of domain walls at zero temperature in random field systems, by balancing the local energy fluctuations from the random fields with the energy cost of domain walls. Interestingly, these results were in disagreement with the field theoretical approaches [132] in all orders of perturbation theory [133, 134] as well as with the supersymmetric formalism [135]. The rigorous studies [136, 137] finally confirmed the Imry-Ma argument, which illustrates that simple heuristic arguments may grasp the essence of physics, not easily detected by more formal methods.

An other important example for this type of arguments is the theorem by Aizenman and Wehr [138], which covers the rounding of first-order phase transitions by quenched disorder: *in 2D, arbitrarily weak (continuous) disorder softens the phase transition to second order.* Even more is true, since there is also a constraint on the possible value of the critical exponents, showed by Chayes et al. [139]: *The space fluctuations of disorder imply in d dimensions that the ν correlation length exponent of the disordered system should satisfy the bound of $\nu \geq 2/d$.*

But how to know, whether quenched disorder is relevant at the critical point of a given system? Harris found the following criterion for the perturbative stability of a non-disordered, clean fixed-point [140]: *Quenched disorder is* irrelevant*, if the correlation length exponent of the* clean *model, ν_c, fulfills the following inequality: $\nu_c \geq 2/d$.*

The criterion can be obtained by perturbative derivation from field theory in the weak disorder limit, however, the underlying physical argument is relatively simple: Due to randomness, the strength of the couplings may locally deviate from the critical value in a correlated region, with size ξ. As a consequence, the δ control parameter is shifted locally according to the relative strength of the fluctuations, given by the central limit theorem as $\delta \sim \xi^{d/2}/\xi^d \sim \xi^{-d/2}$. However, according to Eq. (1.3), a nonzero δ value restricts the correlation length as $\xi' \sim |\delta|^{-\nu_c}$. The shift in δ is irrelevant if this limit is larger, than the actual value of ξ:

$$\xi \leq \xi' \sim \xi^{\frac{d\nu_c}{2}} \,, \tag{1.11}$$

which yields the criterion: $1 \leq d\nu_c/2$.

To check the Harris-criterion for the RTIM, we need the ν_c correlation length exponent of the clean model in d dimensions, which is the same as the ν_c exponents of the classical Ising model in $d+1$ dimensions:

- $d = 1$: $\nu_c = 1$ according to Onsagers's exact solution [1], thus weak disorder is relevant.
- $d = 2$: $\nu_c \approx 0.6301(4)$ in accordance with results from high temperature series expansions and Monte Carlo calculations [43], thus weak disorder is relevant.
- $d \geq 3$: the clean model shows mean-field behavior with $\nu_c = 1/2$ in all $d \geq 3$ dimensions. This fact formally induces the following result: weak disorder is relevant in the quantum case for $d = 3$, marginal in $d = 4$ and irrelevant for $d > 4$. However, more care is needed in this case [26] due to broken hyperscaling, related to the emergence of a dangerously irrelevant variable. While studying the relevance of a new variable — such as the strength of the disorder — at this fixed point it is not guaranteed to be appropriate to first treat

the dangerously irrelevant variable only, prior to the effects of disorder. To the best of our knowledge, a complete analysis of this case is still missing.

In contrast to the wide applicability of the Harris-criterion, there is an increasing number of interesting cases, where it seems to be violated [141–143].

Altogether, the Harris-criterion is an important starting point while investigating the effects of *weak* quenched disorder in a given model, however , in practice more detailed results are needed about the system, e.g.:

- What happens, for strong initial disorder if weak randomness is found to be irrelevant?
- If weak disorder is found to be relevant, then is the behavior conventional with a finite z, or governed by an IDFP?
- What are the critical exponents of the emerging random fixed points?

Although the shown probabilistic arguments help to understand the physics, it is difficult to go beyond the qualitative results and answer these quantitative questions. To make some progress while remaining in the same spirit, the most natural idea is to consider real space renormalizations.

1.4.2 Renormalization group treatment of disordered systems

During renormalization, starting from the parameters of the original Hamiltonian, new effective parameters are successively generated, until a fixed point is reached. Meanwhile, the strength of the disorder may

- decrease, until zero. In this case disorder is irrelevant, thus the universal critical properties are unchanged and described by the clean fixed point. Even so, the location of the critical point is shifted, while the amplitudes of the physical quantities are altered as well.
- reach a finite value, corresponding to a new, disordered fixed point with 'conventional scaling' characterized by a new set of (traditional) critical exponents.
- increase without limits. This case corresponds to the already mentioned infinitely disordered behavior at an IDFP, discussed in more details in Chapter 3. In this case the ratio of two neighboring effective couplings tends to ∞ (or 0), while not only the critical exponents but also the scaling forms change compared to the clean critical point.

It is a priori a hard question, which scenario occurs in a given model. The answer may also depend on the form and strength of the applied disorder. The only reliable general approach is to calculate the critical properties of the model with some suitable method applying the chosen form of disorder and check the results.

Block renormalizations based on the Migdal-Kadanoff idea [144,145] are the most frequently applied RG procedures for disordered systems. Among the many applications, we can find the Potts model [146], the diluted ferromagnet [147], random-field systems [104], random quantum

spin chains [148–150], the random contact process [151] and spin-glasses [152–162]. In the latter case, a great novelty is the chaotic character of the RG trajectories [161,163–168]. In the block RG the system is treated in a homogeneous way, characterized by a Gaussian distribution, whose variance is renormalized during the transformation. Thence, the block RG yields only a rather approximative picture for a strongly disordered system, with large spatial heterogeneities and strongly non-Gaussian behavior.

For specific models there are also results with other RG methods. For instance, there exists a field theoretical functional RG method [169] for models of interfaces in random media. The introduction of disorder in the 2D XY model — which shows a Kosterlitz-Thouless type transition in the clean case — leads to a so called 'Coulomb gas' RG [170].

Another important example is the 'droplet theory' [171–173] for finite dimensional spin-glasses, originating from the phenomenological RG of McMillan [174]. In the formulation of Bray and Moore [175], the basic idea is that the probability distribution of the generated effective couplings at scale L converges towards a non-Gaussian fixed form, having a width, which scales as $\sim L^y$. Remarkably, in 3D the y droplet exponent is positive, corresponding to broadening distributions.

For antiferromagnetic Heisenberg quantum spin chains with $S = 1/2$ Ma, Dasgupta and Hu presented an RG method in 1979 [176,177], which treats the system in an inhomogeneous way. In strong contrast to the usual block RG, where the degrees of freedom are simultaneously eliminated in each block, here in each step the degree of freedom is eliminated with the largest local energy scale to obtain an effective theory at lower energies.

1.4.3 The general strong disorder renormalization group approach

The Ma-Dasgupta-Hu RG approach has actually remained not well known and not well understood during many years, considered only as an approximate procedure, without control. For the RTIM it was Daniel Fisher [20, 21], who first used this method in 1994 and solved analytically the RG equations in 1D, obtaining exact critical exponents and scaling functions. Fisher showed that the critical behavior in 1D is governed by an IDFP — for both the antiferromagnetic Heisenberg chain [178] and the RTIM [20,21] —, where the SDRG method becomes asymptotically exact. Besides the exact critical exponents and scaling functions, he also computed observables that are unknown for the corresponding clean model. As an example, we mention the explicit scaling function describing the magnetization as a function of the external field in the critical region. He also showed the exactness of the obtained results by a direct comparison to the rigorous methods existing for the disordered 2D McCoy-Wu model [15–19].

Following Fisher's results, intensive research started, first in random quantum models and then in classical disordered systems. In all models the various strong disorder RG procedures are based on the same idea: at large scale, disorder dominates with respect to both thermal and quantum fluctuations. In all fields studied so far, the SDRG results provided new insights into the physics and helped to interpret the existing numerical findings. This does not mean that it is easy to apply the SDRG method. On the first hand, it is not evident for a general

random systems, how to construct explicitly the SDRG rules. On the other hand, the form of singularities at the critical point may generally depend also on the strength of disorder. In these cases combined numerical and analytical studies are needed to identify the type of the random fixed point. For a comprehensive review see [14].

At this point we note that it may be hard to observe the IDFP behavior, without being aware of its existence. For instance, the published numerical results typically involve disorder averaged quantities, without noting the potentially broad (or even broadening) width of the underlying distributions. Indeed, disorder averaged quantities always present the 'risk' to be dominated by rare events, giving a false idea about the typical behavior. For instance, in the Sinai model presented in Section 1.3.1, the $\langle x(t)^2 \rangle$ width is a very natural observable in numerical simulations. The result that $\langle x(t)^2 \rangle$ diverges for large times could be interpreted as an absence of localization. Whereas we know that the distance between two independent particles in the same sample remains a finite random variable at infinite time, corresponding to a very strong localization. Even if we are interested in disorder averaged quantities, typically a huge number of random realizations is needed in order to gain reliable estimates, being dominated by rare realizations occurring with a low probability. Also the widely applicable classical and quantum Monte Carlo simulations have to face serious challenges due to the ultraslow dynamics at an IDFP.

In conclusion, there are good reasons to apply the SDRG method whenever disorder heterogeneities determine the dominant state of the system. Numerically, the goal is then to build explicitly the dominant state of the system for a large number of different realizations. To implement this program, it is now necessary to specify the computational methods to carry out the renormalization calculations.

Chapter 2

Strong disorder RG for the RTIM

.

'Elegance is not a dispensable luxury but a quality
that decides between success and failure.'
Edsger Wybe Dijkstra

As a starting point, we introduce the SDRG method for the one dimensional RTIM in this chapter. After summarizing the results in 1D, we discuss the possible extensions for higher dimensional systems. Finally, an effective alternative SDRG algorithm is presented, which opened the way for our investigations in higher dimensional systems.

2.1 Recapitulating the SDRG results for the RTIM in 1D

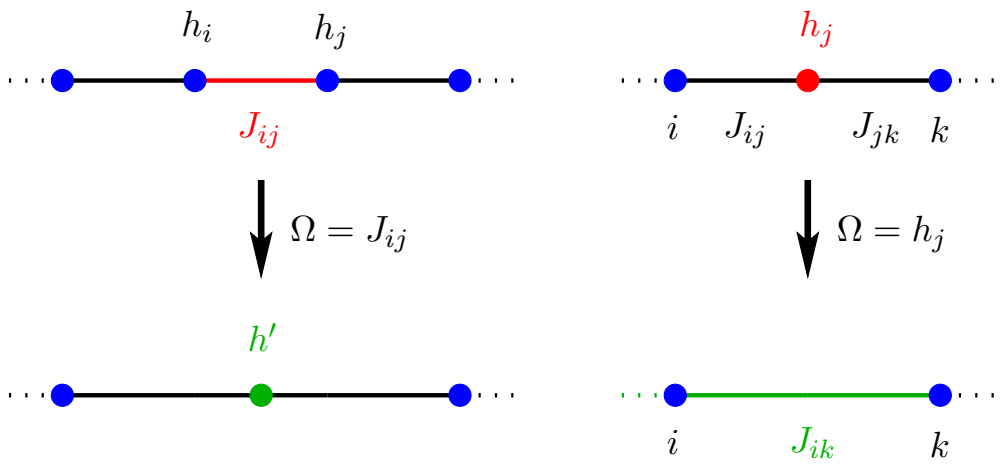

Figure 2.1: Illustration of the decimation steps of the strong disorder renormalization group method in 1D: 'J-decimation' (left) and 'h-decimation' (right).

The SDRG procedure can be imagined as an algorithm in the 'energy space' [26]. In each step the largest local parameter of the Hamiltonian, $\Omega = \max\{J_{ij}, h_i\}$ is decimated out, while

new effective parameters are generated perturbatively. The two RG steps to be considered, are sketched in Fig. 2.1 for a one dimensional system.

- $\Omega = J_{ij}$ (J-decimation): the local Hamiltonian has the form of $\mathcal{H}_{ij} = -J_{ij}\sigma_i^x\sigma_j^x - h_i\sigma_i^z - h_j\sigma_j^z$, including the neighboring spins. Typically $J_{ij} \gg h_i, h_j$, thus the largest energy levels of $\mathcal{H}_{ij}$ are separated by a large gap of $\approx 2J_{ij}$ from the low lying levels, as illustrated in Fig. 2.2. As a consequence, the high energy states can be neglected without significantly altering the low-energy physics. The low lying states are considered as the states of an effective spin with moment $\mu' = \mu_i + \mu_j$ (initially $\mu_i = 1, \forall i$) in an effective transverse field given by

$$h' = \frac{E_1 - E_0}{2} \approx \frac{h_i h_j}{J_{ij}} \,. \tag{2.1}$$

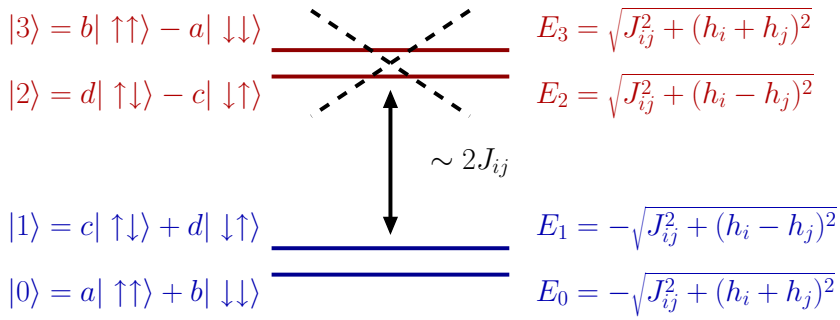

Figure 2.2: Illustration of the energetics of the J-decimation step during the SDRG method, see text for explanation.

- $\Omega = h_i$ (h-decimation): If the largest term is an external field, $h_j \gg J_{ij}, J_{jk}$, then the ground state of the spin is separated by a large gap of $2h_j$ from the excited state, thus the spin is effectively 'frozen' into its ground state. Having a negligible contribution to the magnetization and susceptibility, this spin can be decimated out from the system. However, its $-J_{ij}\sigma_i^z\sigma_j^z - J_{jk}\sigma_j^z\sigma_k^z$ interaction terms lead to a weak effective J_{ik} coupling between the neighboring sites. The value of J_{ik} can be obtained by a second-order degenerate perturbational calculation:

$$J_{ik} \approx \frac{J_{ij}J_{ik}}{h_j}. \tag{2.2}$$

  There is also a simpler way to obtain this result, with an $h \leftrightarrow J$ substitution in Eq. (2.1), corresponding to the self-duality of the critical RTIM in 1D [179].

The renormalization steps are repeated: at each step one more site is eliminated and the energy scale is continuously lowered. For a finite system the renormalization is stopped at the last site, where we keep the energy-scale, Ω, and the total moment, μ, as well as the structure of the clusters. Since the couplings and the transverse fields are dual variables in 1D, the quantum critical point is located at the self-duality point [180],

$$\delta = \overline{\ln h} - \overline{\ln J} = 0 \,. \tag{2.3}$$

In an infinitely large system the topology of the system is preserved in 1D, only the values of the couplings and transverse-fields evolve during the SDRG method. Let we denote the distribution of the J couplings at the energy scale Ω as $R(J,\Omega)$, and similarly for the h transverse-fields as $P(h,\Omega)$. For an infinitesimaly change of the energy scale $\Omega \to \Omega - \mathrm{d}\Omega$, the RG flow equations of the distributions can be written in closed form as illustrated for $R(J,\Omega)$:

$$R(J,\Omega-\mathrm{d}\Omega) = \Bigg\{ R(J,\Omega) + \mathrm{d}\Omega P(\Omega,\Omega) \int_0^\Omega \mathrm{d}J_{ij} \int_0^\Omega \mathrm{d}J_{jk} R(J_{ij},\Omega) R(J_{jk},\Omega) \\ \left[\delta\left(J - \frac{J_{ij}J_{jk}}{h_j} \right) - \delta\left(J - J_{ij}\right) - \delta\left(J - J_{jk}\right) \right] \Bigg\} \left\{ 1 - \mathrm{d}\Omega \left[P(\Omega,\Omega) + R(\Omega,\Omega) \right] \right\}^{-1} . \quad (2.4)$$

The delta functions on the right hand side stand for the generated new coupling and the decimated old couplings in an h-decimation step. The last term ensures normalization of the distribution. A similar equation holds for $P(h,\Omega)$, which can be simply obtained from the $J \leftrightarrow h$ duality of the variables. By expanding $R(J,\Omega-\mathrm{d}\Omega)$ and $P(h,\Omega-\mathrm{d}\Omega)$ by $\mathrm{d}\Omega$ we arrive at the following integro-differential equation system

$$\frac{\mathrm{d}R}{\mathrm{d}\Omega} = R(J,\Omega)\left[P(\Omega,\Omega) - R(\Omega,\Omega)\right] - P(\Omega,\Omega)\int_J^\Omega \mathrm{d}J' R(J',\Omega) R(\frac{J}{J'}\Omega,\Omega)\frac{\Omega}{J'}, \quad (2.5)$$

$$\frac{\mathrm{d}P}{\mathrm{d}\Omega} = P(h,\Omega)\left[R(\Omega,\Omega) - P(\Omega,\Omega)\right] - R(\Omega,\Omega)\int_h^\Omega \mathrm{d}h' P(h',\Omega) P(\frac{h}{h'}\Omega,\Omega)\frac{\Omega}{h'}, \quad (2.6)$$

which should be solved with the initial form of the J and h distributions as initial conditions.

This problem was solved analytically both at the critical point [20,21] and in the off-critical region, in the Griffiths-phases [181]. As a clear indication of IDFP behavior, the distribution of the log-couplings broadens during the SDRG process at the critical point, thus the ratio of two neighboring couplings either tends to 0 or ∞. Consequently, the approximations made by the perturbative derivation of the SDRG rules become asymptotically exact at large scales. The SDRG results have been also successfully tested against independent analytical [15–19] and numerical calculations [182–184]. As the main result, the critical point in 1D can be characterized by the following 3 independent critical exponents:

$$\nu(1\mathrm{D}) = 2, \qquad x(1\mathrm{D}) = \frac{3-\sqrt{5}}{4}, \qquad \psi(1\mathrm{D}) = \frac{1}{2}. \quad (2.7)$$

As we mentioned in Eq. 1.3, ν describes the divergence of the correlation length as the function of δ. The $m = \mu/L^d$ magnetization vanishes with the system size with the exponent x, see Eq. (1.4). As for the Sinai model in Eq. 1.8, the dynamics is described by an activated form of $\ln\Omega \sim L^\psi$, with the same value of the ψ exponent. In the numerical applications, μ and Ω are measured simultaneously for each random sample, being related at the critical point as $\ln\Omega \sim \mu^{1/\phi}$. Here ϕ is the golden ratio in $d = 1$

$$\phi(1\mathrm{D}) = \frac{1+\sqrt{5}}{2} . \quad (2.8)$$

generally given by $\phi = (d-x)/\psi$ in d dimensions. Further details about the scaling results for $d > 1$ can be found in the next chapter.

By analyzing the RG flow of the distributions, it turned out that the SDRG method yields exact results also outside the critical point — in the Griffiths-phases — as far as dynamical quantities are concerned. As an example, the probability of a $h_i = \Omega$ field with a similarly large J coupling — such that $\alpha\Omega < J < \Omega$, where $0 < \alpha < 1$ — goes to zero [20, 21, 181]. This justifies the approximations made during the derivation of the SDRG rules, namely, that all the neighboring couplings are negligible while decimating h_i. In contrast to the critical point, in the Griffiths-phases the spatial correlation length is already finite, thus the results obtained for static quantities (which are characterized by this finite length scale) are only approximate, but getting better and better closer to the critical point.

It is interesting to see that such a simple set of RG rules may successfully capture the essence of the non-trivial critical behavior present in the 1D model. A natural question is, whether one can proceed similarly in higher dimensions, especially in $d = 3$, which is connected to the majority of experiments. In order to study the existence of an IDFP, the SDRG rules need to be extended for $d > 1$.

2.2 SDRG rules for the higher dimensional RTIM

The SDRG method was extended in [26] for higher dimensions, as illustrated in Fig. 2.3 for both J- and h-decimations. During an h-decimation step, the decimated spin may have now several neighbors, thus we generate a new J coupling between each pair of them. There is another difference compared to the one dimensional case. There can be occasions, at which a new J coupling is generated to a space, where one already exists. The widely accepted, usual solution to this problem is the application of the *maximum rule* [24–27]:

- J-decimation: if the sites i and j were connected to a spin a, we apply the maximum rule as $J' = \max[J_{ai}, J_{aj}]$;
- h-decimation: if sites a and b are already connected by a coupling, J_{ab}, than the maximum of them is taken as $\max[J_{ab}, J'_{ab}]$.

We should note here that there is another simple solution, the application of a *sum rule*, where the sum of the two couplings is taken. The use of the maximum rule is justified if the renormalized couplings have a very broad distribution, which is indeed the case at an IDFP. In this case, the two couplings involved are typically very different in their magnitudes, thus their sum is close to their maximum. Consequently, both rules become asymptotically exact at this point.

Although the sum rule may seem to be more natural, it is not evidently closer to grasp the real physics. Indeed, during the initial stages of the RG calculations it may happen that the two couplings at the same place are similar in their magnitudes. With the sum rule this may lead to the rather unphysical result that by eliminating the largest energy scale in the

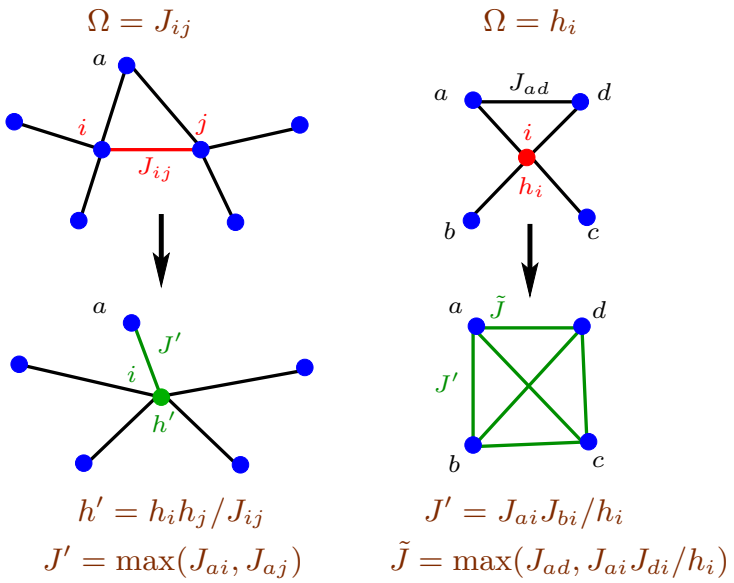

Figure 2.3: Illustration of the decimation steps of the strong disorder renormalization group method in higher dimensions, supplemented by the maximum rule: 'J-decimation' (left) and 'h-decimation' (right).

system, we generate an even larger one. This makes the individual RG steps inconsistent and may alter significantly the initial RG trajectories. Naturally we know that the consequent treatment of the problem would be the recalculation of the perturbative analysis incorporating also the involved J couplings if these are non negligible. As we shall see in the next section, the degree (number of neighbors) of a site increases rapidly during the SDRG process in higher dimensions, thus we should be ready in this case to adaptively incorporate a varying number of couplings to the perturbative analysis. Furthermore in this case not only the energy levels and states are needed, but also an effective local spin system, comprised from more than one spins and their interaction terms. Clearly, this would be a rather challenging future project, thus in the following we try to grasp the essence of the physics with the maximum rule, similarly to earlier studies [24–27].

Remarkably, the maximum rule is not only the simplest consistent extension of the SDRG algorithm to higher dimensions, but it also offers several benefits for the numerical evaluation, as discussed in the next section.

2.2.1 The way towards a more efficient algorithm

If the system is not strictly one dimensional — e.g. a ladder with a finite width ($w > 1$) — the topology is changing considerably during the RG process and therefore one relies on numerical implementations of the RG procedure. In strong contrast to the chain, the ladders become in fact complete graphs early during the RG process, thus the maximum rule is intensively used. Even so, the critical singularities of ladders are identical to those of a chain. However, from the w-dependence of the amplitudes we deduced cross-over functions and estimated the singularities of the 2D system through finite size scaling (for details see [38] and Section 3.3).

The fact that the maximum rule gives back for ladders precisely the exact results known for the chains, indicates also that the extension of the RG steps for higher dimensional systems was correct, including the maximum rule as well.

If the sample is isotropic, say a 2D lattice with size $L \times L$, the numerical application of the naive algorithm is limited to relatively small systems. More dangerous steps in this respect are the h-decimations, during which numerous new couplings are generated and — as a result — sites with large number of links are formed. This way our system will be transformed soon into an almost fully connected graph, having $\mathcal{O}(N^2)$ edges. Consequently at any further decimation step one needs to perform $\mathcal{O}(N^2)$ operations, which leads to a $t \sim \mathcal{O}(N^3)$ performance in time.

Using the maximum rule in the approach, however, offers several ways to speed up the procedure. The first advantage of the maximum rule follows from the fact that in this case the average couplings are weaker than for the alternative sum rule. As a consequence the critical point of the system is at considerably lower values of h, than for the sum rule. Therefore less h-decimations have to be performed in the vicinity of the critical point, which speeds up the calculation. The second and more important consequence of the maximum rule is that a large number of bonds will never be participating in the renormalization process. These latent bonds are in such a local environment that after decimating a nearby site or bond a stronger new coupling is generated to the same edge. This way the original latent bond disappears without participating in the renormalization. We gave an efficient technique to filter out these irrelevant bonds, which led to a considerable improvement of the algorithm in 2D [39].

We have also noticed that the renormalization trajectory is not unique in this case. In order to show this, we define the set of *local maxima*, which are not smaller than any of its neighboring terms. Considering a coupling J_{ij}, it is a local maximum, provided $J_{ij} \geq h_i$, $J_{ij} \geq h_j$, and $J_{ij} \geq J_{ik}$, $\forall k$, as well as $J_{ij} \geq J_{lj}$, $\forall l$. Similarly a transverse field, h_i, is a local maximum, if $h_i \geq J_{ij}$, $\forall j$. These local maxima can be decimated independently, the renormalization performed in any sequence gives the same final result.

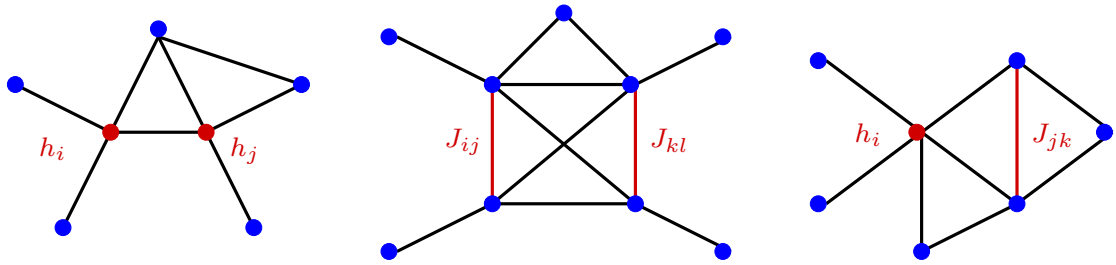

Figure 2.4: Illustration of the three relative configurations of the local maxima, which has to be considered to prove the independence of local maxima decimations.

To outline the proof of this statement first we mention that two local maxima can not be in nearest neighbor position and if these are more remote than next-nearest neighbors, then the statement is trivially fullfiled. Special care is needed if the two local maxima are next-nearest neighbors having one or more edges in common, as illustrated in Fig. 2.4. Considering the three different cases separately (two local h-maxima; two local J-maxima; one local h-maximum and one local J-maximum) with direct calculation one can show that the decimations of local

maxima indeed commute. This is also true in 1D[1], thus instead of searching before each SDRG step for the globally maximal term in the system, we can perform the algorithm in parallel, or even while term by term generating the random sample. Generally, one should not follow the *'decimation of the largest term in each step'* principle, instead it is possible to optimize for the computational time of the renormalization trajectory, which goes over in some order of the local maxima. For details in 2D see [39].

Unfortunately, these achievements were still not enough to study three and higher dimensional systems. But this was not the end of the story, after tedious investigations a new, efficient algorithm was found, presented in the next section.

2.3 Our improved SDRG algorithm

The improved algorithm works by merely deleting couplings (and changing the strength of the remaining ones), without generating new couplings at all. The results of our algorithm are identical to that of any naïve implementation of the SDRG method (having also the maximum rule) for any finite graphs, say with N sites and E edges. However, we gain considerable time in performance: while the naïve method works in $t \sim \mathcal{O}(N^3)$ time, the improved algorithm requires only $t \sim \mathcal{O}(N \log N + E)$ running time. There is also a difference in the memory requirements, being $\mathcal{O}(N^2)$ for the naïve implementation and $\mathcal{O}(N + E)$ for the improved algorithm. For d-dimensional lattices, and Erdős-Rényi graphs, where $E \sim N$, the speed-up factor is roughly N^2.

Having this performance at hand we could go much beyond earlier studies and treat systems up to (two times[2]) $\sim 4 \times 10^6$ sites in all dimensions. Here we note that the results presented in this thesis required ~ 100 CPU-years of calculation with our improved algorithm, while the same process would need $\sim 10^{13}$ times more computational time and $\sim 10^6$ times more memory with the naïve SDRG algorithm.

In the following, we give a detailed description of the improved algorithm. Without restricting generality, we assume that $J_{ij} \leq 1, \forall i, j$. In the improved algorithm we concentrate on the transverse fields, the decimation of which being the most dangerous in respect of the performance of the algorithm. Our strategy is to avoid any h-decimation during the renormalization. For this purpose we divide the sites into two classes by labeling them as 'active' or 'inactive'. Initially, a site with locally maximal transverse-field is labeled as *inactive* with $l_i = 1$, whereas all the remaining sites are labeled as *active*, with $l_i = 0$. Between neighboring sites i and j we define a new quantity $d_{ij} \geq 0$ in the log-energy space, as:

$$d_{ij} = -\ln J_{ij} + \frac{l_i}{2} \ln h_i + \frac{l_j}{2} \ln h_j. \tag{2.9}$$

[1]Due to the symmetric role of the couplings and transverse fields in 1D, it is sufficient for J_{ij} to be a *weak local maximum*: $J_{ij} \geq h_i$, $J_{ij} \geq h_j$ in this case.

[2]As discussed in Chapter 4, from technical reasons we shall always study replicated systems with all the sites doubled.

d_{ij} may be conveniently illustrated as a *distance* between the sites[3]. Having a locally maximal external field, thus inactive site, k, between i and j and decimating it out the RG rules lead to the additivity property: $\tilde{d}_{ij} = d_{ik} + d_{kj}$. According to the maximum rule in the original J variables, this distance is compared with the existing value of d_{ij} and their *minimum* is taken. Generally, the true distance between i and j, denoted by δ_{ij} is given by the shortest path which goes over the inactive sites. It is easy to see that decimating out all or a subset of inactive sites is equivalent to find in the original problem the shortest paths among the non-decimated sites which go through the decimated sites. This is a well known graph-theoretical problem [185] for which efficient numerical algorithms are available. So far we have only considered the h-decimation steps.

The opposite limiting case, in which only J-decimations occur, is equivalent to an other well known graph theoretic problem, the *minimum spanning tree* problem [185] with link weights $w_{ij} = -\ln J_{ij} \geq 0$. In this case the sites are fused together, and the value of the effective transverse field is given by $\ln h = W + \sum \ln h_i$, where W is the total weight of the minimum spanning tree. During the SDRG method both J and h decimation steps occur, which leads to a combined algorithm of the shortest path and minimum spanning tree finder methods.

In order to formulate this combined algorithm, we have to concentrate to the active sites, and define for each active site a *range* in the log-energy space as

$$r_i = -\ln h_i. \tag{2.10}$$

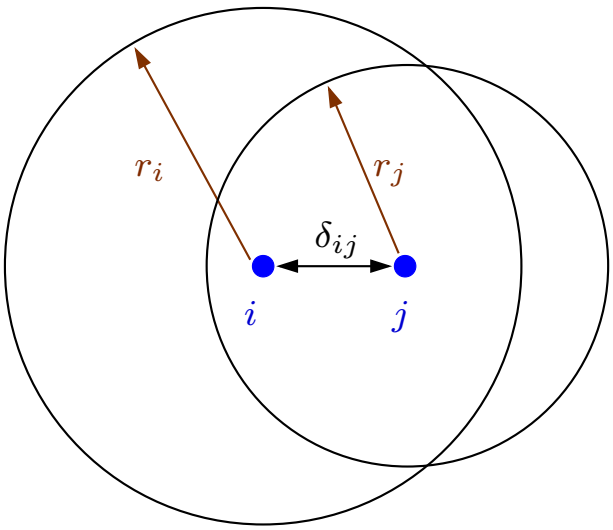

Figure 2.5: The improved algorithm is formulated over a set of new, distance-like variables, which is based on the properties of the system in the 'energy space'. During the method we compare the r_i and r_j ranges of the active sites with the δ_{ij} distances between them, see text.

In the improved algorithm we compare the ranges of the active sites with the δ_{ij} true distance measured between them as illustrated in Fig 2.5. In this respect two possibilities may happen.

[3]Although the geometrical picture is rather expressive, the triangle inequality is generally not fulfilled for the d_{ij} distances, thus these do not form a true metric.

- If two active sites (i and j) can mutually reach each other (such that $\delta_{ij} \leq r_i$ and $\delta_{ij} \leq r_j$), then i and j are fused together into an effective active site, with a new range of

$$\tilde{r} = r_i + r_j - \delta_{ij}. \tag{2.11}$$

  This means that the new effective range is the sum of the individual ranges minus the *cost* to connect them. The distance measured from this effective site to another site, say k, is simply given by $\min(d_{ik}, d_{jk})$.

- If an active site can not reach any other active site within its r_i range (such that $r_i < \delta_{i,j}, \forall j$), then it is turned to 'inactive'. Consequently, we set its weight to $l_i = 1$ and update the distances, $d_{ij}, \forall j$, according to Eq. (2.9). There is no way for an inactive site to become active again in the process.

In the above mentioned renormalization steps, which can be used in arbitrary order, the number of active sites in the system is reduced by one. Repeating these decimation rules we arrive to a system having only inactive sites and no further fusion steps take place. The complete cluster-structure including the excitation energies is readily encoded in this configuration, which can be extracted without further renormalization steps. In any case the final result of the improved algorithm is identical to that obtained by the naïve SDRG algorithm.

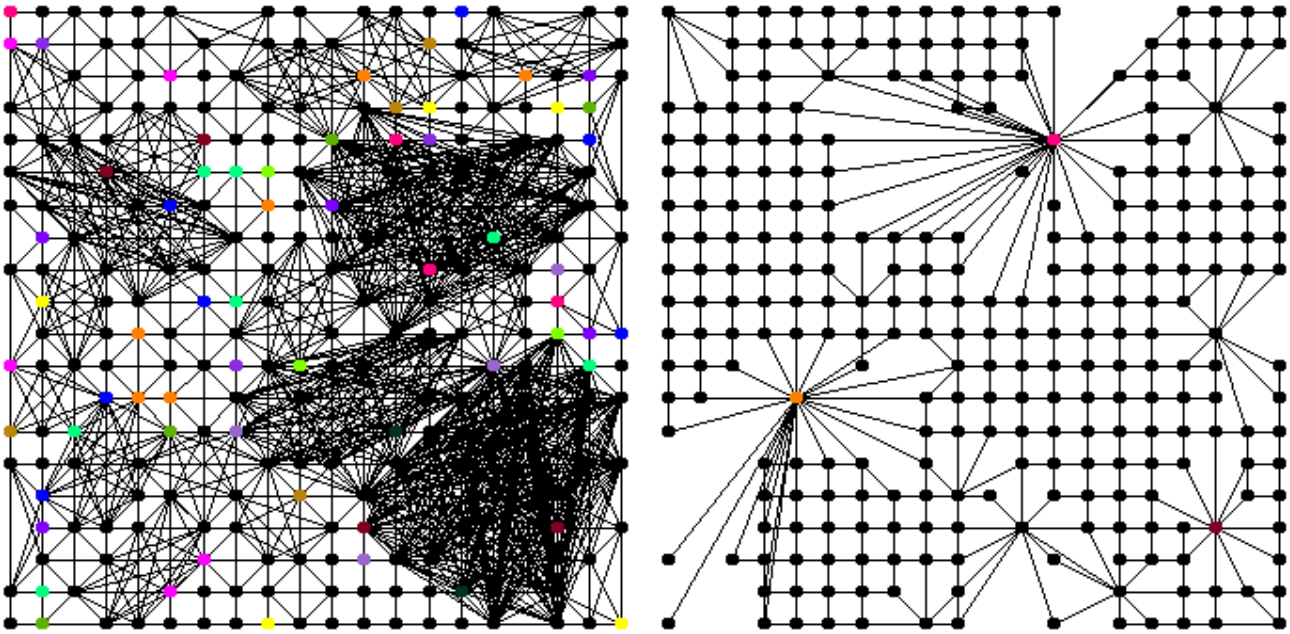

Figure 2.6: Snapshots of the naïve (left) and improved (right) SDRG algorithms for the same critical $N = 20 \times 20$ sample with box-h disorder (see Section 3.4) and open boundary conditions, where 40% of the spins is decimated out. While in the naïve algorithm numerous new couplings are generated, leading to a running time of $t \sim \mathcal{O}(N^3)$, in the improved algorithm we merely delete sites, thus $t \sim \mathcal{O}(N \log N)$. The colors reflect the h values of initially locally maximal sites.

In practice one should measure the δ_{ij} true distances between the active sites as effectively as possible. This can be done from a selected site i by Dijkstra's method [185]. In each step

of Dijkstra's algorithm the nearest site is explored to i, which has not been explored yet, until the range, r_i, is reached.

Although the renormalization steps of the algorithm can be performed in any order, in practice it is more efficient to apply an algorithm, which works simultaneously for all the active sites. This means that we carry out the exploration of the shortest path from all the active sites in parallel. In this case it is sufficient to follow the shortest paths only until reaching a length of $r_i/2$ instead of the full r_i range before deactivating a site[4]. In this parallel implementation two active sites are fused together, if their exploration zones overlap. Interestingly, there is no need during these fusion steps for the already explored inactive sites.

Now we can formulate the following conjecture: *a given inactive site can be only explored once during the parallel algorithm, thus after the first occasion, it can be safely removed from the system.*

Let we outline the proof of this essential statement.

- Let we follow, what happens with an i inactive site, which is already explored from an active site, a. As we mentioned earlier, in the fusion steps it plays no role, only its active site is fused into other active sites. However, after inactivating the site a, the studied inactive site i still remains in the system and may be explored from other active sites as well. We wish to show that this *never* happens during the exploration of the *shortest* paths starting from other active sites. In order to prove this, it is sufficient to compare the $d_{xy}^{(i)}$ length of a path through i between to sites (x and y) outside the exploration zone, with a path going directly through a instead, having a length of $d_{xy}^{(a)}$, see Fig. 2.7.

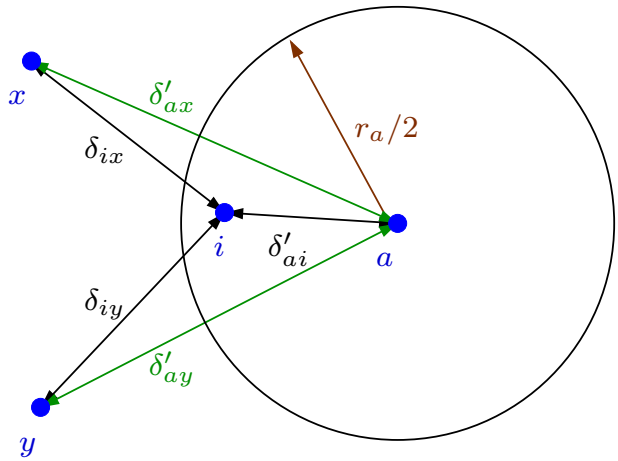

Figure 2.7: There is no need to keep the site i during the parallel SDRG algorithm (see text), because of the fact that $d_{xy}^{(a)} \equiv \delta'_{ax} + \delta'_{ay} < d_{xy}^{(i)} \equiv \delta_{ix} + \delta_{iy}$.

Because of the fact that i is inside the exploration zone of a, while x and y are outside of it: $\delta_{ax} > r_a/2$, $\delta_{ay} > r_a/2$ and $\delta_{ai} < r_a/2$. With the inactivation of site a, its label is set to 1, and its distances are modified as follows: $\delta'_{ax} = \delta_{ax} - r_a/2 > 0$, $\delta'_{ay} = \delta_{ay} - r_a/2 > 0$

[4]This step ensures a speed-up factor of 2^d in d dimensions, while for the infinite dimensional Erdős-Rényi graphs this really yields a boost.

and $\delta'_{ai} = \delta_{ai} - r_a/2 < 0$. Since $d^{(i)}_{xy} \equiv \delta_{ix} + \delta_{iy}$ and $d^{(a)}_{xy} \equiv \delta'_{ax} + \delta'_{ay}$, we find that:

$$d^{(a)}_{xy} < d^{(i)}_{xy} \, . \tag{2.12}$$

Since each inactive site is explored only once, our algorithm is structurally equivalent with Dijkstra's method, having the same time complexity of $\mathcal{O}(N \log N + E)$ on any graphs with N sites and E edges. As an illustration, in Fig. 2.6 we compare the topology of the renormalized systems in the naïve and improved SDRG algorithms at an intermediate step.

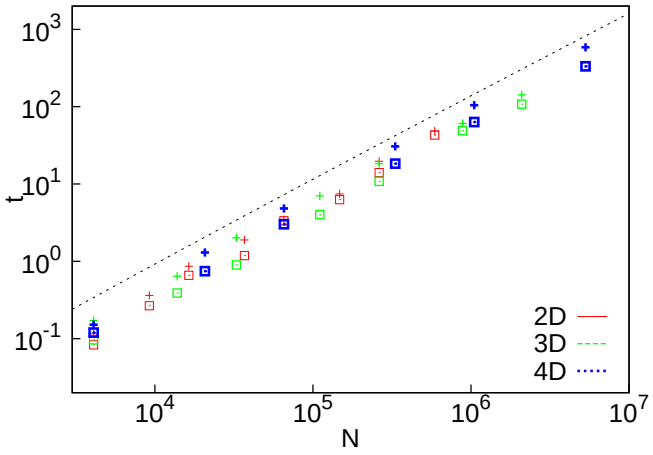

Figure 2.8: Computational time of the algorithm, t (in seconds in a 2.5GHz processor), as a function of the size of the hypercubic systems, N, in a log-log scale for 2D, 3D and 4D. Measurements were made at the critical point for at least 10^4 realizations, with two types of disorder ('fixed-h' + and 'box-h' ⊡, see Section 3.4 for details). The theoretical prediction, $t \sim N \log N$, is indicated by a dashed line. For movies illustrating the algorithms see [186].

We have checked numerically the computational time of the algorithm, t, for 2D, 3D and 4D hypercubic clusters consisting of N sites. The results are shown in Fig. 2.8 for two types of randomness[5]. For a given N and for a given type of disorder the computation time is practically independent of the topology of the cluster and t is well described by the theoretical bound: $\sim N \log N$.

2.3.1 Interpretation as a novel type of percolation

The improved algorithm led to a process, which is also interesting in itself. Although the quantum phase transition presented in the RTIM is often called as a *quantum percolation process* [26, 79], due to similarities in the behavior, the underlying percolation process never became clearly observable. Now, the SDRG algorithm with the maximum rule really transforms it into a novel class of classical percolation process, with positive feedback.

Here we can imagine the sites as individual agents (i.e. computers or neural cells) distributed in a d dimensional space (or over an arbitrary network), having limited resources for communication. Let these agents try to build up a communication network from their resources. If

[5]For Erdős-Rényi graphs the process is even faster, having a lower average degree of 3 in our case.

two agents can mutually connect to each other, then the connection is established and their remaining resources are shared (after subtracting the cost of the connection). This way a positive feedback is built into the process: the larger a connected network becomes, the larger resources it owns to establish further connections[6]. If an agent is unable to establish connections from its own resources, it may still become part of a communication channel by lowering its cost with the amount of its unused resources.

In the end of the next section we show that this percolation process has also a direct interpretation for the Contact Process.

2.4 Our improved SDRG approach for other models

The SDRG approach has been applied for a series of random quantum and classical problems, but restricted mostly for the one dimensional case [14]. In higher dimensions the numerical implementation of the SDRG method for these models has basically the same problems as the naïve algorithm for the RTIM. In these cases one can try to generalize the concept of our improved algorithm. We carried out this generalization of the improved SDRG algorithm for two random quantum models: for the disordered q-state quantum Potts model [36], as well as for the disordered quantum rotor model, which is a standard model of granular superconductors and Josephson arrays [187, 188]. In addition to this, we show the decimation rules for the Contact process.

2.4.1 Disordered q-state quantum Potts model

In this model at each lattice site, i there is a q-state spin variable: $s_i = 1, 2, \ldots, q$ and the Hamiltonian is given by [36]:

$$\mathcal{H} = -\sum_{\langle ij \rangle} J_{ij}\delta(s_i, s_j) - \sum_i \frac{h_i}{q}\sum_{k=1}^{q-1} M_l^k \ . \tag{2.13}$$

Here the first term represents the interaction between the spins and the second term is a generalized transverse field where M_i is a spin-flip operator at site i: $M_i|s_i\rangle = |s_i + 1, \mod q\rangle$. As for the RTIM, what we recover for $q = 2$, the J_{ij} couplings and the h_i transverse-fields are random variables. The SDRG decimation rules are very similar to that of the RTIM and differ only by an extra factor of $\kappa = 2/q$:

- J-decimation: the effective transverse-fields are given by: $h' = \kappa h_i h_j / J_{ij}$;
- h-decimation: the effective couplings are given by: $J_{ik} = \kappa J_{ij} J_{jk} / h_j$.

In the improved algorithm in Sec. 2.3 the distances and ranges in the log-energy space — see Eqs. (2.9), (2.10 and (2.11) — are extended by a constant: $d_0 = \ln(q/2) = -\ln\kappa$, which now

[6]Without this positive feedback, the process is equivalent to the classical percolation at large scales.

read as:

$$d_{ij} = -\ln J_{ij} + \frac{l_i}{2}\ln h_i + \frac{l_j}{2}\ln h_j + d_0, \tag{2.14}$$

$$r_i = -\ln h_i + d_0, \tag{2.15}$$

$$\tilde{r} = r_i + r_j - \delta_{ij} + d_0. \tag{2.16}$$

This generalization works for $2 \leq q < \infty$.

2.4.2 Disordered Josephson junctions

Here we consider disordered bosons with an occupation operator, $\hat{n}_i$, and a phase-variable, φ_i, at site i. The system is described by the following Hamiltonian [187, 188]:

$$\mathcal{H} = -\sum_{\langle ij \rangle} J_{ij}\cos\left(\varphi_i - \varphi_j\right) + \sum_i U_i \hat{n}_i^2 \ , \tag{2.17}$$

with random J_{ij} Josephson couplings and U_i charging energies. The SDRG approach has also been applied to this model resulting in the following RG rules.

- U-decimation: if the strongest parameter in the Hamiltonian is a grain charging energy U_j, then site j is eliminated and effective couplings are generated between the nearest neighbors of j, say i and k. In second-order perturbation calculation this is given by: $J_{ik} = J_{ij}J_{jk}/U_j$.

- J-decimation: if the strongest coupling in the system is a Josephson coupling, J_{ij}, the two sites form a composite site having an effective charging energy, U', which does not depend on the value of J_{ij}, but given by: $\frac{1}{U'} = \frac{1}{U_i} + \frac{1}{U_j}$.

In the improved SDRG algorithm the distances and ranges in Eqs. (2.9) and (2.10) are modified with the substitution $h_i \to U_i$ as:

$$d_{ij} = -\ln J_{ij} + \frac{l_i}{2}\ln U_i + \frac{l_j}{2}\ln U_j, \tag{2.18}$$

$$r_i = -\ln U_i. \tag{2.19}$$

On the contrary the updated range in Eq.(2.11) has a different form now, given by:

$$\tilde{r} = \ln\left[\exp\left(r_i\right) + \exp\left(r_j\right)\right]. \tag{2.20}$$

In fact we have tried out these SDRG steps for this model in 2D and found a finite dynamical exponent, without IDFP behavior. This means that there is no guarantee that the (static) SDRG results are correct. A similar result was obtained very recently by applying the SDRG method (without the maximum rule) with more involved decimation steps, which are up to higher orders of the perturbative calculation correct [189]. The authors claimed that the SDRG method may provide even in this case correct results.

2.4.3 Contact Process

The Contact Process describes the spreading of infections (or computer viruses), which similarly to those responsible for the *common cold*, do not yield any long lasting immunity, thus individuals become susceptible again after infection [37]. The Contact Process is defined on the sites of a lattice or graph, with two possible states: healthy (0) or ill (1). An ill site, i, can infect a neighboring site, j, with a rate λ_{ij}, while it can heal spontaneously with a rate μ_i. This means that healthy sites become infected at a rate proportional to the number of their infected neighbors.

For high healing rates, the infection dies out, while for high infection rates, the illness spreads over the entire system. In between there is a critical point, in nonequilibrium, which belongs to the universality class of directed percolation in the clean case [190, 191], including many other models according to the famous conjecture: *In the absence of any special conservation laws and quenched disorder, continuous phase transitions between an active and a single absorbing state of many particle systems with local interactions and a scalar order parameter are of the directed percolation type.* In spite of the many related models and systems — e.g. catalytic reactions [192], depinning transitions [193], flow of granular matter [194, 195] — the critical exponents of the directed percolation class were only observed in 2007 in the electrohydrodynamic convection of a liquid crystal [196]. It has been argued that earlier experiments were unsuccessful because of the presence of some kind of disorder in the system [197].

The phase transition in the disordered case can be conveniently studied by the SDRG, built up from the following two steps:

- if the largest term is a healing rate, $\Omega = \mu_i$: in this case site i is almost always in the 0 healthy state, thus it can be effectively eliminated from the system, taking into account that it acts as a weak infection channel between its neighbors. If j is an infected neighbor of i, than it infects i with rate λ_{ij}, which may infect an other neighboring site, k with a probability of $\lambda_{ik}/(\mu_i + \lambda_{ik})$. Thus, the effective infection rate is given by

$$\lambda'_{jk} = \frac{\lambda_{ij}\lambda_{ik}}{\mu_i + \lambda_{ik}} \approx \frac{\lambda_{ij}\lambda_{ik}}{\mu_i} \,. \tag{2.21}$$

- if the largest term is an infection rate, $\Omega = \lambda_{ij}$: the two connected sites, i and j are usually both ill or both healthy, thus can be treated as an effective site for long times with a summarized moment $\mu' = \mu_i + \mu_j$. If both sites are ill, their joint healing requires two steps, first the healing of site i with rate μ_i and then the healing of site j, which has a small probability of $\mu_j/(\lambda_{ij} + \mu_j) \approx \mu_j/\lambda_{ij}$. Taking into account also the opposite case, in which site j heals first, we arrive at

$$\mu' = \frac{2\mu_i\mu_j}{\lambda_{ij}} \tag{2.22}$$

These SDRG rules are analogous to the rules seen for the RTIM with $\lambda_{ij} \to J_{ij}$ and $\mu_i \to h_i$, except the factor of 2 in the last case. For the RTIM, the new effective couplings can not be

larger than the decimated ones, however, the prefactor in the Contact Process may lead to increasing terms. For strong enough disorder this effect can be surely neglected, thus in this case the critical behavior is governed by the same IDFP, as for the RTIM. However, the basin of attraction of the fixed point is expected to be smaller, although its precise determination is out of scope of the SDRG, relying on perturbative estimates for the decimation rules. Regarding this question, a more careful analysis is given by Hoyos in [198], where he claims that the SDRG trajectories reach the same IDFP for any weak amount of initial disorder.

In terms of the Contact Process the active sites of the improved algorithm correspond to (mostly) infected sites up to the time scale of the SDRG (defined as $t \sim \Omega^{-1}$), while the inactive sites correspond to (mostly) healthy sites. The essence of dynamics is grasped by the positive feedback of the percolation process described in Sec. 2.3.1 as follows. If two (or more) active sites are able to infect each other mutually before being healthy again, than each of these sites are typically infected at the same time, and it takes much longer until all of them become healthy again.

2.5 Discussion

Let we summarize our findings in this chapter. First, we have introduced the SDRG method, which is conveniently supplemented by the maximum rule in higher dimensional systems, having a running time of $\mathcal{O}(N^3)$ for N sites, with a memory consumption of $\mathcal{O}(N^2)$. After briefly summarizing our algorithmic results about this method (for details see [39]), we introduced our equivalent *improved algorithm*, which maps the problem to a novel type of classical percolation and requires only $\mathcal{O}(N \ln N)$ time and $\mathcal{O}(N)$ memory. We note here that our improved SDRG algorithm significantly simplifies the problem by never generating any new couplings. In the future, this may also possibly lead to an analytical solution in higher dimensional systems. In addition to the RTIM, we have also discussed the application of our improved algorithm for other random quantum models and for the random Contact Process.

Now that we have seen the advantages of the maximum rule, we have to note that several other simplifications have been tried during the years in order to speed up the calculations in higher dimensions. As the general idea, one may try to keep only the $\mathcal{O}(N)$ number of strongest couplings in the system at any stage of the SDRG, for an example see [26]. Such a global filtering technique must be intrinsically wrong at an IDFP due to the large heterogeneities presented in the system. Anyhow, even a local filtering method has to face a serious challenge due to the nature of the decimation steps. While in each step the largest couplings are decimated out, the small couplings — which we try to delete form the system — may become the largest couplings at a later stage of the SDRG, responsible for the physics at that lower energy scale. The only known local method, which overcomes this issue is the applied maximum rule.

Chapter 3

Numerical application of the SDRG method in higher dimensions

At the beginning of this chapter, a brief overview is given about the scaling results at an IDFP in higher dimensions. We also discuss the ground state structure yielded by the SDRG method and its connection to physical quantities. In the rest of this chapter, we prepare for the next chapters by summarizing the available numerical results and open questions in higher dimensions.

3.1 Infinitely disordered scaling in higher dimensions

Before studying the problem numerically (or experimentally), it is important to overview the available theoretical expectations and analytical results. Here we follow the lines of [14]. At an IDFP, the log-energy scale, $\ln \Omega$, scales with the linear size of the system size, L as

$$\ln \left(\Omega_0/\Omega\right) \sim L^{\psi} \ , \tag{3.1}$$

where Ω_0 denotes a reference energy scale. The average spin-spin correlation function is defined as $G(r) = \overline{\langle \sigma_i^x \sigma_{i+r}^x \rangle}$, where $\langle \dots \rangle$ denotes the ground-state average and $\overline{(\dots)}$ stands for the averaging over quenched disorder. The asymptotic value of the correlation function defines the magnetization, m, in the system:

$$\lim_{r \to \infty} G(r) = m^2 \ , \tag{3.2}$$

where $m > 0$ in the ferromagnetic phase and $m = 0$ in the paramagnetic phase. The connected correlation function, $\tilde{G}(r) = G(r) - m^2$, for $r \to \infty$ in the vicinity of the critical point behaves as:

$$\tilde{G}(r) \sim r^{-2x} \exp(-r/\xi) \ , \tag{3.3}$$

where the correlation length, ξ, is divergent at the critical point as:

$$\xi \sim |\delta|^{-\nu} \ . \tag{3.4}$$

Thus at $\delta = 0$ there is a power-law decay of the correlations $G(r) \sim r^{-2x}$, which is related to the fractal structure of the spin clusters. Indeed, the average cluster moment, μ, is related to the energy-scale, Ω as:

$$\mu \sim [\ln(\Omega_0/\Omega)]^{\phi} \ , \tag{3.5}$$

and can be expressed also with the size:

$$\mu \sim L^{d_f} \ . \tag{3.6}$$

Here the fractal dimension of the cluster, d_f, is related to the other exponents as:

$$d_f = \phi\psi = d - x \ . \tag{3.7}$$

The above described critical exponents characterize the behavior at $T = 0$ and longitudinal magnetic field $H = 0$. However, as we mentioned in Section 1.1, these exponents also influence the low-temperature and low-field behavior of the system in the so called quantum critical region. As an example, the low-temperature susceptibility at $H = 0$ can be written in the form of

$$\chi(T) \sim \frac{(\ln T)^{(d-2x)/\psi}}{T} \ , \tag{3.8}$$

while the specific heat is given by

$$C_v(T) \sim (\ln T)^{-d/\psi} \ . \tag{3.9}$$

For a small H longitudinal field we get similar expressions at $T = 0$:

$$\chi(H) \sim \frac{(\ln H)^{-x/\psi}}{H} \ , \tag{3.10}$$

while

$$C_v(H) \sim (\ln H)^{-d/\psi} \ . \tag{3.11}$$

3.2 Structure of the ground state and relation to physical quantities

As the result of the SDRG method, a low-energy effective description is obtained for the original system. During renormalization effective spin clusters are formed, which are then decimated out from the system at a lower energy scale. This way, the renormalized system is built up from non-interacting, independent spin clusters [24, 27, 34], each of which is described by a Greenberger-Horne-Zeilinger state [199] given by $1/\sqrt{2}(|\uparrow\uparrow \ldots \uparrow\rangle + |\downarrow\downarrow \ldots \downarrow\rangle)$. Although the spins inside a spin cluster are equivalent to each other, the spatial structure of the clusters is non-trivial. In strong contrast to the geometrical clusters known for classical percolation, the spin clusters of the RTIM are generally non-contiguous objects. At the critical point the spin

clusters — and the whole system as well — has a fractal structure as illustrated in Fig. 3.1 for 2D. We shall analyze the critical cluster structure in Chapters 5 and 8 in more details.

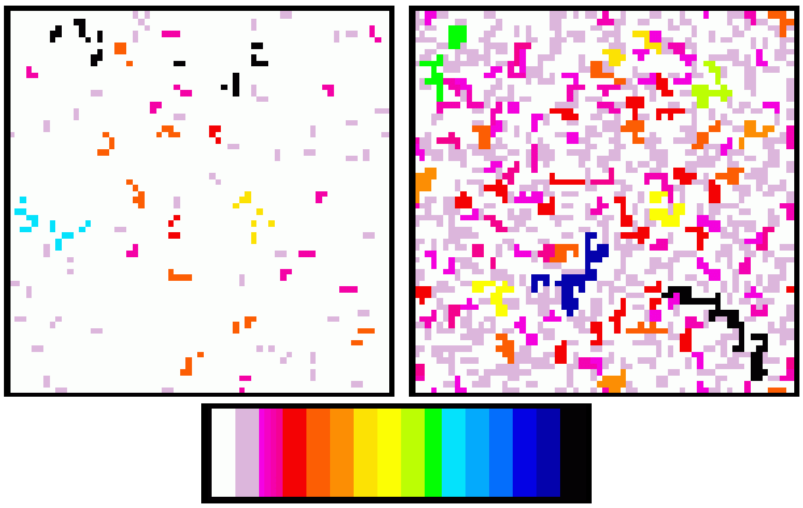

Figure 3.1: The ground state cluster structure obtained by the SDRG method is illustrated for critical 2D RTIM systems at $L = 64$ with box-h (left) and fixed-h (right) disorder, see Sec. 3.4 for details. The size of the clusters is increasing with the color as indicated at the bottom of the figure. The one-site clusters are white, while the points of the largest cluster are black. Although, the clusters are more extended for fixed-h disorder, the same universal behavior is shown in our results.

The physical properties of the system can be obtained from the resulted cluster structure. For instance, the smallest effective external field of the spin clusters is used to give the value of the energy-gap at the critical point, determining the long-time dynamical properties of the system. Similarly, the size of this cluster is applied to define the magnetization of the system at criticality. The extension of these definitions, which is also valid in the off-critical region is given in Chapters 5 and 6.

3.3 From 1D towards 2D

In nature there are materials, which are in a way between two integer dimensions, such as they are built from $(d-1)$-dimensional layers having a finite width, w. Examples are thin films, magnetic multilayers [200] or ladders of quantum spins [201]. One interesting question for such multilayer systems is the properties of critical fluctuations, when the linear extent of the layers, L, goes to infinity. The $(d-1)$-dimensional layered system may also be interesting from the point of view of the d-dimensional system, as we show for the simplest case of ladders corresponding to $d = 2$.

Previous calculations in 2D had a limited accuracy due to small system sizes [23, 25, 26, 28], where both spatial extensions of the system were relatively small, $L \sim 150$ (see Table 3.1). Without having at hand our improved SDRG algorithm, we came to the following idea in 2008.

Table 3.1: Numerical estimates of the critical exponents at the infinite disorder fixed point in 2D. MC: Quantum Monte Carlo simulation; CP: Monte Carlo simulation of the 2D random Contact Process. The exponents, ϕ, denoted by an asterisk are calculated from the scaling relation in Eq. (3.7).

ψ	ϕ	ν	x	method	
0.4(1)	2.5*		1.0	QMC [28]	(1998)
0.42(6)	2.5(4)	1.07(15)	1.0(1)	SDRG [26]	(2000)
0.5	2		0.94	SDRG [25]	(2000)
0.6	1.7	1.25	0.97	SDRG [23]	(2001)
0.51(6)	2.04(28)*	1.20(15)	0.96(2)	CP [29]	(2009)
0.51(2)	1.97(10)*	1.25(3)	0.996(10)	our results [38]	(2009)

Although RTIM ladders with a finite $w \ll L$ width are expected to show 1D behavior[1](see [25] for $w = 2$), from the finite-size scaling of the results with w [202, 203] it may be possible to extrapolate for the 2D behavior without in fact calculating in 2D. By studying ladders with a limited width $1 < w \leq 20$ we could increase the L length up to $L_{\max} = 4096$ with 4×10^4 random realizations[2]. This way we have already reached the limit with L where no further systematic finite-size effects are seen.

The first difficulty, which one encounters, is the problem of precisely locating the critical point for each w. As we discuss in the next chapter in more details, this is a quite challenging task in higher dimensions and the precision of the existing methods was not sufficient. In order to solve this problem, we introduced sample dependent pseudo-critical points. We analyzed the *shift* of the mean value of these transition points and the *width* of the distribution as a function of w, and estimated the exponents $\nu_s(2D)$ and $\nu_w(2D)$. These are found to be identical and given by the correlation-length exponent of the 2D model. At the critical points we studied the scaling form of the magnetization and excitation energies, and found identical critical exponents to the 1D case. However, from the scaling of the prefactors with w, we could gain estimates for the critical exponents in 2D [38], as summarized in the following.

Let us consider a physical observable, A, which at the critical point has the mean value, $A(w, L)$. This quantity scales with the critical exponent of the 2D model, $\alpha(2D)$, as:

$$A(w, L) \sim L^{\alpha(2D)} \tilde{A}(w/L) \tag{3.12}$$

where the scaling function, $\tilde{A}(y)$, for small arguments behaves as:

$$\tilde{A}(y) \sim y^{\alpha(2D)-\alpha(1D)} \tag{3.13}$$

where $\alpha(1D)$ is the critical exponent in the 1D model. Consequently for a finite w, but for

[1]This is only true for systems having a discrete symmetry. For systems having continuous symmetry, such as for Heisenberg antiferromagnetic spin ladders, the low-energy excitations may sensitively depend on the value of w, being gapless for odd w and having a gap for even w [201].

[2]In this case we applied box-h disorder and periodic boundary conditions in both directions.

$L \to \infty$, we have

$$A(w, L) \sim L^{\alpha(1D)} a(w) \tag{3.14}$$

with $a(w) \sim w^{\omega}$ and $\omega = \alpha(2D) - \alpha(1D)$. In general we measure the scaling function $a(w)$ for different widths, estimate the exponent ω and calculate the critical exponent in 2D as: $\alpha(2D) = \alpha(1D) + \omega$. Since the exponents in 1D are exactly known and the correction term, ω, is comparatively small we have obtained quite accurate exponents in 2D. Our estimates for the critical exponents fit to the trend of the previous results in 2D, as shown in Table 3.1. Among these we emphasize the exhaustive Monte Carlo study of the 2D random Contact Process, published recently [29], requiring ~ 40000 CPU-days of calculation for systems up to size 8000×8000.

3.4 Our goals in higher dimensions

Having at hand our improved algorithm, our first aim is to gain accurate estimates for the critical exponents, calculating in 2D. Regarding the 3D system, in an early study the possible presence of an IDFP was expected [26], but no evidence in favour of this conjecture has been presented yet. Also no studies are available about the random contact process in 3D.

In even higher dimensions no results of any kind are known, thus it is a completely open question, if there is an upper critical dimension, d_u, such that for $d < d_u$ infinite disorder scaling works and for $d \geq d_u$ we have conventional random criticality. Furthermore, it is also an open question, whether for $d \geq 2$ the fixed point is universal, not depending on the actual form of initial disorder. In order to answer this question we are going to study also four dimensional, as well as Erdős-Rényi random graphs [204] representing the infinite dimensional limit.

Besides the limited system size, the uncertainties of earlier results arise mainly from two reasons. On the one hand, the location of the critical point is not well known, which may lead to strong systematic errors. In order to suppress this error, we plan to extend our analysis based on the pseudo-critical points applied for ladders. This technique is known as the *doubling method*, and also yields estimates for the correlation-length exponent, as presented in the next chapter. On the other hand, the achievable finite-size estimates of the critical exponents — although asymptotically expected to be disorder-independent — depend strongly on the applied form of disorder for moderate system sizes. The resulting finite-size corrections may be very hard to distinguish from the systematic errors caused by the imprecise critical point or small realization number. It is generally also possible, that the critical exponents indeed depend on the form of the applied disorder.

In contrast to earlier investigations, where only one type of initial disorder was used, we have decided to carry out all the calculations for two types of disorder, in order to check universality. For both type of chosen disorder the couplings are uniformly distributed:

$$p(J) = \Theta(J)\Theta(1 - J) \, , \tag{3.15}$$

$\Theta(x)$ being the Heaviside step-function. For box-h disorder the distribution of the transverse-

fields is uniform:

$$q(h) = \frac{1}{h_b}\Theta(h)\Theta(h_b - h) \ , \tag{3.16}$$

whereas for fixed-h disorder we have a constant transverse-field:

$$q(h) = \delta(h_f - h) \ . \tag{3.17}$$

In the following we use the logarithmic transverse-field $\theta = \ln h_b$ or $\theta = \ln h_f$ to characterize the system, motivated by the exact one-dimensional result in Eq. (2.3). In 1D this definition yields the critical values of $\theta_c(b) = 0$ for box-h disorder and $\theta_c(f) = -1$ for fixed-h disorder. The quantum control-parameter is defined as $\delta = \theta - \theta_c$, being 0 at the critical point. In higher dimensions $\theta_c(b) > 0$, while $\theta_c(f) < 0$ (see Table 9.1), thus the chosen disorder realizations represent the two opposite possibilities during the SDRG algorithm: for fixed-h disorder the SDRG method starts by only J-decimation steps, while for box-h disorder with only h-decimation steps.

This choice has proven to be rather beneficial during our calculations, due to the fact, that the finite-size corrections of the exponents in these cases have an opposite sign (while being dominantly monotonic). This way the finite-size estimates for the two types of disorder hedge in the asymptotic value, which makes our estimates much more reliable compared to previous ones. An other important topic — not have been tested so far — concerns the scaling predictions in the Griffiths-phase in higher dimensions [14].

Besides these investigations we also wish to study the entanglement entropy in the vicinity of the critical point, to clarify the open questions concerning its higher dimensional behavior in interacting systems.

3.5 Discussion

In this chapter we summarized the scaling properties of IDFPs, as well as the available numerical results in higher dimensions, including our studies for ladders [38]. Finally, a brief summary was given about our aims concerning the next chapters. As the first and most important step, we have to obtain the precise values for the location of the critical points in all cases.

Chapter 4

Determination of the critical point

The precise identification of the θ_c critical point of a disordered system is a very important issue, since the accuracy of the determination of the critical exponents depends sensitively on it. In a random sample of linear size, L, one can generally define finite-size $\theta_c(L,\alpha)$ pseudo-critical points for each α sample [205–211]. These are usually given as the position of the maximum of some physical quantity, which is divergent at the critical point in the thermodynamic limit, e.g. the susceptibility[1]. Having at hand the distribution of $\theta_c(L)$, it provides important information about the scaling behavior at the fixed point of the system [208]. In particular one concerns the shift of the average value, $\overline{\theta_c}(L)$, which according to finite-size scaling theory [206, 208] is expected to scale as:

$$\left|\theta_c - \overline{\theta_c}(L)\right| \sim L^{-1/\nu_s} \ , \tag{4.1}$$

with the shift exponent, ν_s. Similarly, one measures the width of the distribution, $\Delta\theta_c(L)$, which behaves for large-L as:

$$\Delta\theta_c(L) \sim L^{-1/\nu_w} \ , \tag{4.2}$$

where ν_w denotes the width exponent. If quenched disorder is irrelevant, which happens for weak disorder if the clean systems correlation length exponent satisfies $\nu_c > 2/d$ (see Section 1.4.1), then for the disordered system we have $\nu_s = \nu_c$ and $\nu_w = 2/d$, while the thermodynamic quantities at the fixed point are self-averaging. On the contrary for relevant disorder, which happens for $\nu_c < 2/d$, there is a new *conventional random fixed point* with a correlation-length exponent, $\nu \geq 2/d$ [139], and we have $\nu_s = \nu_w = \nu$. In this fixed point there is a lack of self-averaging. These predictions, which have been debated for some time [205], were checked later for various models [206, 208–211]. At (higher dimensional) IDFPs the relation of ν_s to ν_w is still an open question.

4.1 Traditional approaches

Without determining sample dependent pseudo-critical points, it is generally much harder to obtain accurate estimates for the true critical point as we illustrate here on two examples.

[1] In the case of an IDFP, the susceptibility is divergent also in the Griffiths-phase, thus we need to find an other appropriate definition as discussed later in this chapter.

Although their lower precision, these ideas may yield expressive physical insight as the methods, described in the following. The magnetization $m(L,\theta)$ has a finite value in the ferromagnetic phase, while vanishes exponentially in the paramagnetic phase. In between there is a finite-size critical point, where it scales as $m(L) \sim L^{-x}$. By calculating the ratios of magnetizations $r(L,\theta) = m(L,\theta)/m(L/2,\theta)$, the $r(L,\theta)$ functions should cross each other asymptotically at the true critical point. To use this method, a huge number of realizations is needed to reduce the statistical error of the $r(L,\theta)$ values, otherwise we get non-monotonic functions with multiple crossing points. Moreover, we must do this with a high enough resolution in θ around the *a priori* not known critical point. An other way is to search for the point numerically, where the distribution of the log-gaps broadens according to the IDFP scaling (see Chapter 6 for details). This idea was applied in [25] for ladders with width $w = 2$ together with the following approach for 2D systems. The method applied also in [26] relies on the natural expectation that similarly to the 1D case, the critical point occurs, where the J and h decimations become balanced. As a consequence, the distribution of the last decimated J and h values tend to have similar forms, which can be hunted numerically.

In what follows, we come back to methods working through pseudo-critical points, which besides a precise estimate for the critical point also yield the values of ν_s and ν_w.

4.1.1 Results in the chain geometry

In 1D, finite-size critical points are studied in Ref. [212], located by different methods based on the free-fermion mapping of the problem [213]. The finite-size critical points are shown to satisfy the self-duality condition for each random sample:

$$\sum_{i=1}^{L} \ln J_i = \sum_{i=1}^{L} \ln h_i \ , \tag{4.3}$$

from which follows that the distribution of $\theta_c(L)$ is Gaussian with zero mean and with a mean deviation of $\Delta\theta_c(L) \sim L^{-1/2}$. Consequently the width-exponent of the distribution is given by:

$$\nu_w = \nu(1D) = 2 \ , \tag{4.4}$$

which satisfies the rigorous bound of $\nu \geq 2/d$ [139].

This also means that for periodic boundary conditions there is no shift of the mean values, thus ν_s can not be measured in this case. However, with free boundary conditions, where the number of h and J couplings is different by 1, there is a shift characterized by an exponent of

$$\nu_s = 1 \ . \tag{4.5}$$

4.1.2 The doubling method for ladders

In the ladder geometry, i.e. for $w \geq 2$, the free-fermionic mapping is no longer valid, therefore new methods have to be utilized to locate pseudo-critical points. We used the doubling method

[211, 212] combined with the strong disorder renormalization group.

For a given random sample α of length L and width w, we construct a replicated sample 2α of length $2L$ and width w by gluing two copies of α together at the boundaries. Using the SDRG method we calculate some physical quantity (magnetization or energy gap) in the original and in the replicated sample, which is denoted by $f(\alpha, L)$ and $f(2\alpha, 2L)$, respectively. We form their ratio $r(\alpha, L) = f(2\alpha, 2L)/f(\alpha, L)$ and study as a function of θ. At $\theta = \theta_c(\alpha, L)$ this ratio has a sudden jump, which is identified with the pseudo-critical point of the sample. As we have shown for the case of ladders [38], the actual value of $\theta_c(\alpha, L)$ is practically independent of the physical quantity we considered, since this singularity is connected to the topology of clusters. Namely, the pseudo-critical point defined this way corresponds to the θ value, below which the last decimated clusters in the two parts fuse together during the SDRG process. As a consequence, the magnetization ratio is 1 below the pseudo-critical point, where it suddenly jumps to 1/2.

4.2 Applying replicas of the system

Although in a finite sample there is no sharp phase transition, we wish to find a well-defined, sharp pseudo-critical point for a given sample. Let we propose a Gedankenexperiment in order to overcome this problem. In an infinitely large system there would be already a sharp phase transition, so let us assign to each finite system with periodic boundary conditions an infinitely large replicated system. In order to construct this replicated system we open up somewhere[2] our finite system and glue it together in all direction with its copies, using altogether N such replicas. In the limit of $N \to \infty$ we arrive at an infinite system — having already a sharp phase transition —, in one-to-one correspondence with our original finite system. Consequently we may define the pseudo-critical point, as the θ value of the phase transition in the corresponding replicated system.

By applying this approach in quasi-1D, we arrive at the pseudo-critical point definition with the doubling method: if the last decimated clusters of two replicas fuse together, then all the corresponding clusters fuse together, thus the magnetization ratio jumps from 1 to $1/N$, which goes to zero for $N \to \infty$. In higher dimensional systems there can be d such transition points, where the replicas fuse together in one of the d directions. This is not surprising, since in classical percolation, we have also multiple possibilities to define the sample-dependent critical point, corresponding to the directions, in which the spanning cluster is formed. However, in our case with $N \to \infty$ the effective external field of a 'spanning' cluster rapidly goes to zero, thus it will be soon fused together in all the other directions with all the other 'spanning' clusters. This way we have a unique critical point for each infinitely large replicated sample for $N \to \infty$.

The emerging 'spanning' cluster has equivalent sites in the replicas, consequently the sample shows correlations within the range of the size of the sample. The corresponding cluster in the finite PBC system is called as a *correlation cluster*. By applying the maximum rule in the SDRG

[2] We arrive at the same results, independently from the location of the boundary, where we opened up the system.

method, each effective coupling has a contribution coming from a limited amount of original couplings, which form a contiguous cluster. This connected subgraph (also called as *energy cluster*[3]) corresponding to the correlation cluster has a geometrical spanning property right at the pseudo-critical point. This way the quantum phase transition point is precisely mapped to the percolation threshold of the energy clusters. As we have seen in Chapter 2 the SDRG supplemented by the maximum rule is mapped even more generally (also outside the critical point) to a novel type of classical percolation. The correlation cluster and the corresponding energy cluster is illustrated in Fig. 4.1 for 2D and 3D.

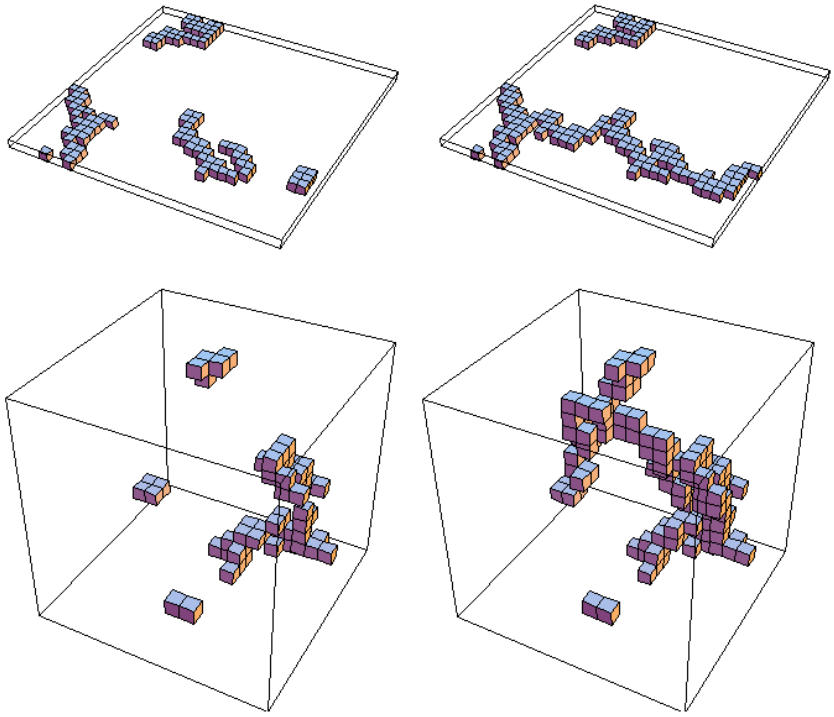

Figure 4.1: The correlation cluster shows fractal behavior at the critical point, as illustrated for fixed-h randomness in 2D ($L = 32$) and 3D ($L = 16$) in the left panels. At the same time, the corresponding connected subgraphs (known as the *energy clusters*), have spanning property, analogously to classical geometrical percolation.

In practice, we can not construct the infinitely large replicated system, but there is no need for this. It is sufficient to study a doubled system, with $N = 2$ to obtain the same results with a minor modification of the SDRG rules.

4.3 The doubling method in higher dimensions

Based on the previous section, we use the doubling method in higher dimensions to obtain the properties of the infinitely large replicated sample. In higher dimensions we glue together two identical samples at the boundaries as indicated in Fig. 4.2 (coming from the restriction of the replicated system for $N = 2$).

[3]The notation comes from the fact that this is the map of the couplings involved in the calculation of the clusters energy scale.

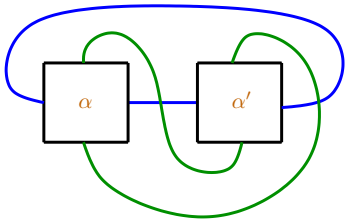

Figure 4.2: 2D illustration of the boundary conditions used in the doubling procedure in higher dimensions. In each direction the opposite sides of the replicas are connected leading to a toroidal configuration.

In this doubled system the correlation cluster is easily observed: during the SDRG method a cluster emerges, which contains identical sites in the sample and its copy. However, in order to accomplish our goal, the h effective external field of a correlation cluster must be set to zero during the SDRG method. This way we recover the behavior of the infinite periodic system, where the 'spanning' cluster has an external field equal to zero. Without applying this modification, the doubled system may have multiple 'correlation clusters', having equivalent sites in both replicas. Now we are ready to apply the doubling method in higher dimensions summarized as follows[4] .

In this procedure we glue together two identical copies (α, α') of the sample by surface couplings and renormalize it up to the last site for different values of the control parameter, θ. The renormalization is found to be qualitatively different for $\theta < \theta_c(L, \alpha)$ and for $\theta > \theta_c(L, \alpha)$. For weak quantum fluctuations, $\theta < \theta_c(L, \alpha)$, the last decimated spin cluster contains equivalent sites of α and α'. On the contrary for $\theta > \theta_c(L, \alpha)$ in the last decimated spin cluster there are no equivalent sites of α and α', thus there is no correlation cluster. For each sample the transition point can be located with high precision requiring a logarithmic number of steps as the function of the allowed error.

4.4 Studying the distribution of pseudo-critical points

Here we present our numerical results regarding the pseudo-critical points of 2, 3 and 4 dimensional lattices. Generally we have considered 4×10^4 realizations (10^5 in 3D) and even for the largest systems, we had at least 10^4 samples. The pseudo-critical point was determined in each sample, at a given length L, with a better accuracy, than 1% of the obtained width of the distributions. The distribution of the pseudo-critical points is shown in Fig. 4.3 for fixed-h disorder. We carried out all the calculations also for box-h disorder and found that both the mean value and the width of the distribution is considerably larger in this case.

Taking into account the result in Eq. (4.1) the appropriate scaling combination is $y = (\theta_c(L) - \theta_c)L^{1/\nu}$ in terms of which the scaled distributions, $\tilde{p}(y)$, are shown in the lower panels of Fig. 4.3. Here using our final estimates collected in Table 9.1 we obtain excellent scaling

[4]Here we note that the introduced doubling method does not rely on the maximum rule, thus can be applied more generally.

collapse of the data for both type of randomness. The calculation of these exponents is presented in the next sections.

The scaling curves for both kind of applied disorder approach the same standardized master curve (for 2D see [39]), which indicates that the fixed point of the SDRG transformation is unique and (at least for strong enough disorder) strongly attractive. The master curve is different from the Gaussian, present in 1D [212]. In higher dimensions the distribution is non-symmetric and the maximum of the curve is shifted to negative values. We have calculated the percolation (or spanning) probability, P_s, at the critical point, which is given by the fraction of samples having finite replica correlation function at θ_c. It can be expressed with the scaled distribution function as $P_s = \int_0^\infty \tilde{p}(y)\mathrm{d}y$. Our estimates are $P_s(2\mathrm{D}) = 0.149(2)$, $P_s(3\mathrm{D}) = 0.088(3)$ and $P_s(4\mathrm{D}) = 0.081(3)$ for both types of disorder. Although with maximum rule we have an underlying geometrical percolation of the energy clusters at the critical point, these values are much smaller, than for standard percolation [214].

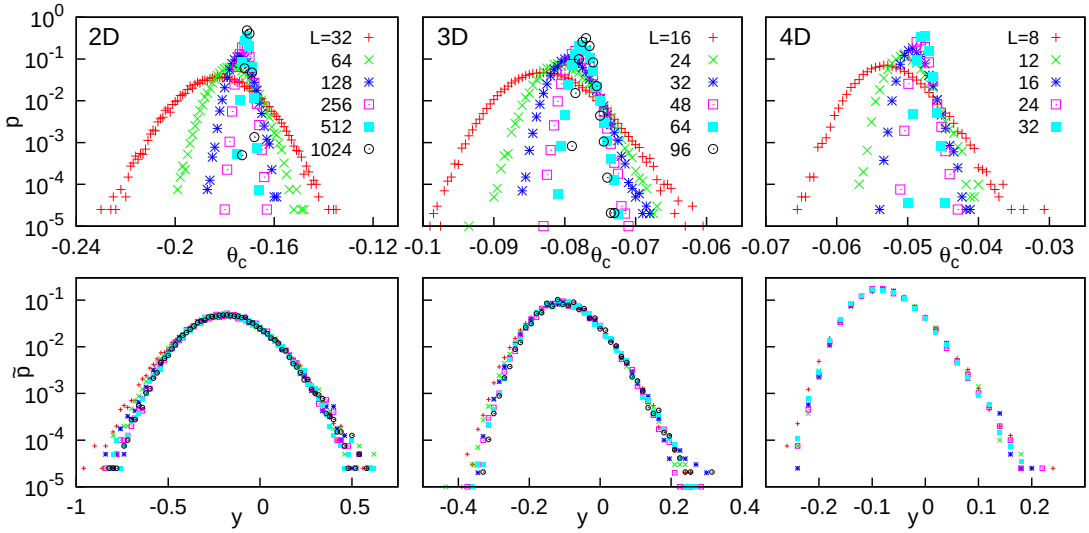

Figure 4.3: Distribution of the pseudo-critical points, $\theta_c(L)$, in 2D, 3D and 4D for fixed-h randomness (upper panels). In the lower panels the scaled distributions are shown as a function of $y = (\theta_c(L) - \theta_c)L^{1/\nu}$, see the text.

4.4.1 Shift of the pseudo-critical points

For a fixed linear size, L, we have calculated the mean value, $\overline{\theta_c}(L)$, which is expected to follow the scaling form in Eq. (4.1). In order to get estimates for ν_s without knowing θ_c, we have calculated effective, size dependent shift exponents which are defined as:

$$\frac{1}{\nu_s(L)} = -\frac{1}{\ln 2}\ln\left[\frac{\overline{\theta_c}(2L) - \overline{\theta_c}(L)}{\overline{\theta_c}(L) - \overline{\theta_c}(L/2)}\right] . \tag{4.6}$$

These are shown in the left panel of Fig. 4.4 as a function of $N = L^d$ in a log-lin scale. In all dimensions, the exponents calculated from the mean values show approximately $1/L$

correction terms for both type of disorder — although with different signs — leading to the same asymptotic estimates. The obtained extrapolated values are $1/\nu_s(2D) = 0.80(2)$, $1/\nu_s(3D) = 1.01(2)$ and $1/\nu_s(4D) = 1.35(8)$. Our estimates for θ_c in Table 9.1 came from a fit corresponding to Eq. (4.1) using these ν_s values supplemented by their leading order $1/L$ correction. An independent estimate for the θ_c critical points is given in the next section, without using the values of the shift exponents.

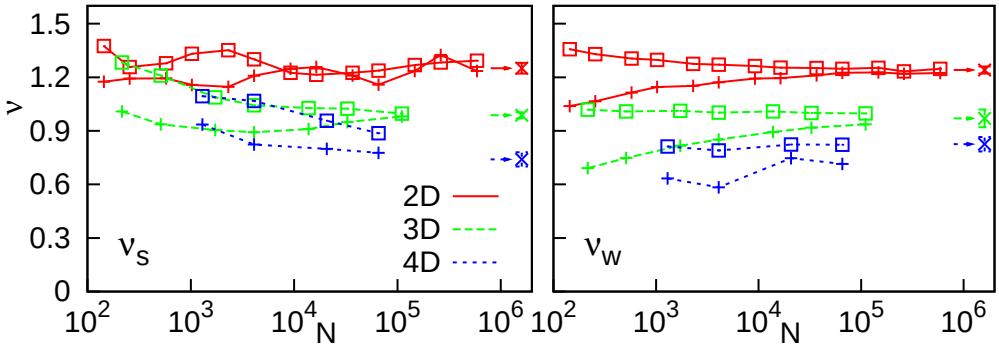

Figure 4.4: Finite-size estimates for the shift, ν_s, (left) and the width, ν_w, (right) critical exponents for 2D, 3D and 4D with both different disorders (fixed-h +, box-h ⊡). The estimated values, as given in Table 9.1 are indicated at the right edge of the figures. Although both the shift and width decreases as a power-law, the limiting value of the shift is the *a priori* unknown true critical point in contrast to the zero limiting value of the width. Therefore, the shift exponents have larger errors as a rule.

4.4.2 Scaling of the width of the pseudo-critical points

We have also measured the standard deviation of the distribution of the pseudo-critical points, $\Delta\theta_c(L)$. In contrast to the mean values, now there is no constant in the scaling from in Eq. (4.2), thus the following, much simpler expression can be used to obtain the size-dependent critical exponents: $1/\nu_w(L) = \log_2\left(\Delta\theta_c(L)/\Delta\theta_c(L/2)\right)$. However, there are finite-size corrections to the $\Delta\theta_c(L) \sim L^{-1/\nu_w}$ form and the obtained effective exponents gain relatively large systematic errors from these. We have found that much weaker finite-size corrections are presented by using the following expression:

$$\frac{1}{\nu_w(L)} = \sinh^{-1}\left[-\frac{\Delta\theta_c(2L) - \Delta\theta_c(L/2)}{2\Delta\theta_c(L)}\right]\frac{1}{\ln 2}\,, \tag{4.7}$$

which is based on the equality: $\Delta\theta_c(2L) - \Delta\theta_c(L/2)/(2\Delta\theta_c(L)) = (2^{-1/\nu_w} - 2^{1/\nu_w})/2 \equiv \sinh\left(-1/\nu_w \ln 2\right)$. Our finite-size exponents are plotted in the right panel of Fig. 4.4. Extrapolating the effective exponents yields the following disorder independent values: $1/\nu_w(2D) = 0.808(10)$, $1/\nu_w(3D) = 1.03(5)$ and $1/\nu_w(4D) = 1.21(6)$.

Our estimates for the shift- and width-exponents agree within the error of the method[5],

[5]In 4D the estimates of the two exponents seem to be at the border or slightly outside the estimated error. To decide about the agreement or disagreement of the two exponents in this case one should study even larger systems, in particular to reduce the error in the position of the critical point.

which corresponds to the renormalization group result for a classical conventional random critical point [208]. In order to make a direct check of the equivalence of the two exponents we have formed the ratio:

$$\alpha(L) = \frac{\theta_c - \overline{\theta_c}(L)}{\Delta\theta_c(L)} \ , \tag{4.8}$$

which should approach an L-independent constant value at the 'true' critical point, θ_c, provided $\nu_s = \nu_w$. In Fig. 4.5 we have plotted the $\alpha(L)$ ratios as a function of $\ln L$ using different input values for the critical point, θ_c in 2, 3 and 4 dimensions.

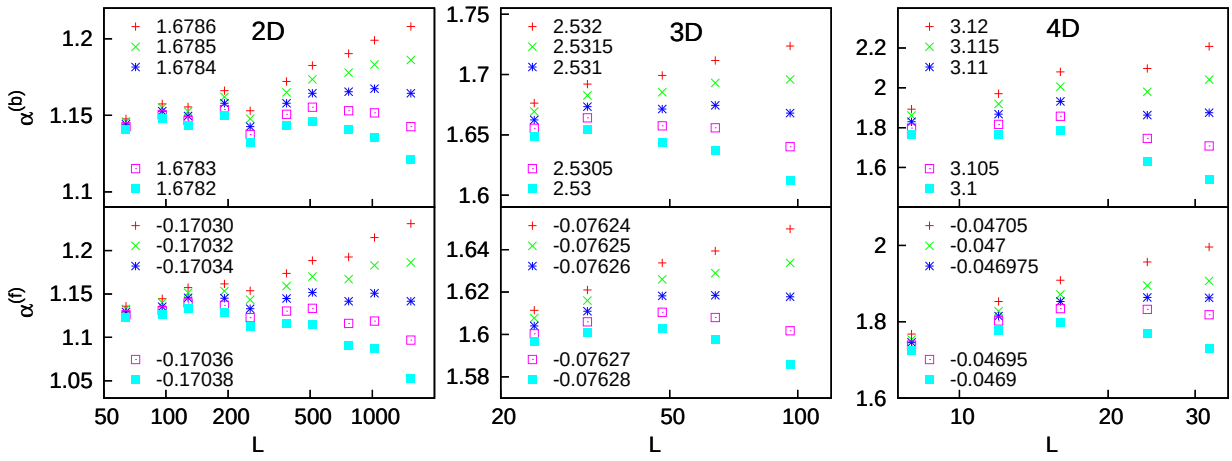

Figure 4.5: The ratio in Eq. (4.8) as a function of $\ln L$ for different input values of the critical point, θ_c, in 2, 3 and 4 dimensions. At the 'true' critical point $\alpha(L)$ should be approximately both disorder and L independent if $\nu_s = \nu_w$. The upper panels show the results for box-h randomness, while the lower panels correspond to fixed-h randomness.

As one can see in this figure the L-dependence of $\alpha(L)$ is very sensitive to the input value of θ_c, for both types of randomness, but at its right value the $\alpha(L)$ ratios are approximately L independent for large sizes. This method works especially well in 2D, where we obtain the same θ_c value as with the direct fit, having an approximately constant $\alpha(L)$ for a broad range of sizes. This means that θ_c can be obtained without the determination of ν_s (and ν_w), from the assumption alone that $\nu_s = \nu_w$. However, in 3 and 4 dimensions $\alpha(L)$ is only constant for the largest system sizes, thus it is possible that we are still not in the asymptotic regime, where $\nu_s(L) = \nu_w(L)$. Even so, $\nu_s = \nu_w$ may be fulfilled for $L \to \infty$. We note that the (somewhat subjective) θ_c values obtained this way in 3D and 4D agree with the previously determined values within the errors in Table 9.1. However, there is still another possibility that ν_s and ν_w are slightly different even for $L \to \infty$ in 3D and 4D. In order to reassuringly decide this question, even larger system sizes will be needed in future investigations. Let we note that the $\alpha(L)$ ratios are close to each other for the two types of disorder (e.g. $\alpha = 1.15(2)$ in 2D), which supports the first scenario, stating that asymptotically $\nu_s = \nu_w$.

In contrast to other cases, in 2D with box-h disorder there are also earlier estimates, $\theta_c^{(b)} = 1.680(5)$, in [27] and $\theta_c^{(b)} = 1.676(5)$, extrapolated from ladders by us in [38], which are consistent with our more accurate result of $\theta_c^{(b)} = 1.6784(2)$.

4.5 Discussion

In the first step, we have determined a pseudo-critical point, $\theta_c(\alpha, L)$, by our variant of the *doubling method* for each random sample, α. The applied doubling method simulates the behavior of an infinitely large replicated system to decrease finite-size corrections. This shall be useful also in the forthcoming chapters. During this method, we renormalize the duplicated sample and calculate the structure of the clusters, among which there might be such, which have sites (in equivalent positions) in both replicas, known as the *correlation cluster*. By increasing the control parameter, θ, the correlation cluster is decreasing and at a well defined $\theta_c(L)$ value it vanishes. We consider $\theta_c(L)$ as the pseudo-critical point of the given sample.

In the second step we have studied the shape and size-dependence of the distributions of the pseudo-critical points. We have checked that finite-size scaling relations in Eqs. (4.1) and (4.2) are satisfied in all dimensions, and used them to obtain finite-size estimates for the exponents. For a given dimension the estimated exponents are found to be independent of the form of disorder, furthermore the shift and the width exponents are identical within the error of the calculation. Consequently, the distributions of the pseudo-critical points can be rescaled to a master curve in terms of the variable, $y = (\theta_c(L) - \theta_c)L^{1/\nu}$, which is shown in Fig. 4.3 with $\nu = \nu_s = \nu_w$. Our estimates about the critical exponents are collected in Table 9.1, together with the estimates of the *true* critical points. Although we have studied systems having approximately the same number of spins in all cases, the error of the estimates is increasing with the dimensionality, due to decreasing linear length, L.

Chapter 5

Magnetization

Having at hand accurate estimates of the critical points for both types of randomness we are ready to study the critical behavior of the RTIM. In this respect we have concentrated our effort at the critical point, where we have studied the distribution function of the magnetization, as well as that of the (log-)gaps (see next chapter) and calculated critical exponents by finite-size scaling. We studied finite systems of hypercubic lattices in dimensions 2, 3 and 4, up to a linear size of $L = 2048$, $L = 128$ and $L = 48$, respectively. For each size we renormalized typically 40000 random samples (for each type of disorder), but even for the largest systems we have treated at least 10000 realizations.

In this chapter we are going to study the magnetization, $m(\delta, L)$, in the vicinity of the critical point on 2D, 3D and 4D lattices, where δ denotes the distance from the critical point and L stands for the system size. In the thermodynamic limit, $L \to \infty$, the magnetization is finite in the ferromagnetic phase ($\delta < 0$) and vanishes at the critical point as: $\lim_{L\to\infty} m(\delta, L) \sim (-\delta)^{\beta}$ where β is the magnetization exponent. At the critical point the spin clusters are fractals, which is illustrated in the left panel of Fig. 4.1 for 2D and 3D. The mass of these critical clusters scales as $\mu \sim L^{d_f}$, where d_f is the fractal dimension, related to the anomalous dimension of the magnetization as $x \equiv \beta/\nu = d - d_f$.

After discussing the possible definitions of magnetization, we are going to study its critical properties and determine the corresponding critical exponents. Based on these results we check the validity of the expected scaling behavior around the critical point.

5.1 Spin clusters related to magnetization

According to the widely accepted definition, the magnetization of a finite system is related to the μ magnetic moment of the last decimated cluster during the SDRG method as $m = \mu/L^d$. This final cluster, which is also known as the *magnetization cluster* has the smallest effective h external field during the method. At the critical point for larger and larger systems the magnetization cluster also tends to be the largest cluster in the system. As we shall see, this definition gives the correct results in the ferromagnetic phase, for $\delta < 0$, and at the critical point, however it fails to grasp the magnetic properties in the paramagnetic phase, for $\delta > 0$,

where the magnetization is relatively small. The smallest possible size of the magnetization cluster is $\mu_{min} = 1$, thus the corresponding minimal magnetization is given by $1/L^d$, i.e. it varies as a power-law of L. This happens in fact in the paramagnetic phase, where the magnetization should vanish exponentially instead. Physically, the last decimated cluster is only related to the spontaneous magnetization, if it has a very small effective external field, which is the case for $\delta \leq 0$ — where the magnetization clusters grow with L —, but not fulfilled in the paramagnetic phase.

However, the application of the doubling method helps to overcome this difficulty. In this case the correlation cluster, which emerges below the pseudo-critical point has a vanishing external field, thus it is a promising candidate to determine the spontaneous magnetization of the system, being never decimated out. We have checked numerically that for not too small system sizes, whenever a correlation cluster exists, it is also the magnetization cluster in the corresponding finite system. An alternative definition of the magnetization is given by the asymptotic value of the correlation function in Eq. (3.2). In a replicated sample the replica correlation function can be used as introduced in Sec. 4.3. By definition, two spins at a distance $r \sim L$ are correlated if both are in the same correlation cluster. Consequently the magnetization is given by $m(\delta, L) = \mu_{\text{corr}}/L^d$, where μ_{corr} is the mass of the correlation cluster.

At the critical point we have checked in all cases that both definitions give the correct critical exponents. Even so, there is a finite ratio of the samples above their pseudo-critical point, in which the magnetization cluster is not a correlation cluster. This significantly reduces the number of samples with non-zero magnetization by working with correlation clusters. Therefore, at the critical point we present our results for the magnetization clusters leading to much less noisy data. In Section 5.2.3 we show that at criticality all the large clusters share the same scaling behavior, thus the technical details of the definition are asymptotically irrelevant. Nevertheless, while studying the off-critical region in Sec. 5.3 the definition based on the correlation clusters is applied, being the only appropriate definition in the paramagnetic phase.

5.2 Critical point

5.2.1 The average magnetization

In order to obtain an accurate estimate for the critical exponents, we have calculated average moments of the magnetization clusters, $\overline{\mu}$, which are plotted in the left panel of Fig. 5.1 as a function of N in a log-log scale. The average moment is found to scale as: $\overline{\mu}(N) \sim N^{d_f/d}$, where d_f is the fractal dimension in agreement with the scaling relation in Eq. (3.6). The points are asymptotically on straight lines, the slope of which being the same for the two different randomnesses for the same d.

Comparing the average mass of the magnetization clusters at two finite sizes, effective, size-dependent fractal dimensions can be derived as $d_f(L) = \log_2\left(\overline{\mu}_L/\overline{\mu}_{L/2}\right)$. However, there are finite-size corrections (such as an additive constant) to the underlying $\overline{\mu}_L = aL^{d_f}$ expression, and the obtained effective exponents gain strong systematic errors from these. As in Section

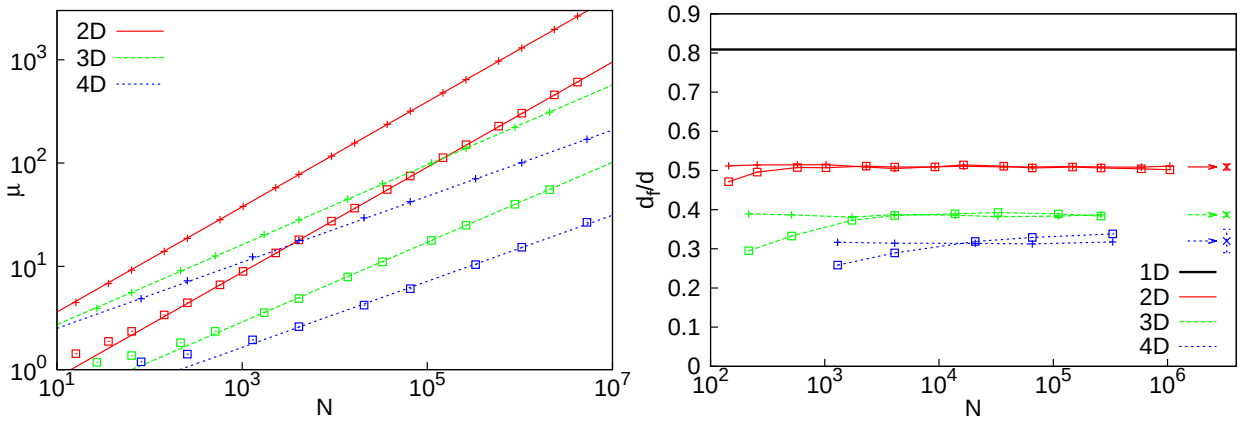

Figure 5.1: The left panel shows the average moment of the magnetization cluster at the critical point vs. the size of the system in a log-log plot for 2D, 3D and 4D for both types of randomness (fixed-h: $+$, box-h: $\boxdot$). The slope of the straight lines is given by: $d_f/d = 0.509$, $d_f/d = 0.387$ and $d_f/d = 0.32$ for 2D, 3D and 4D, as obtained from the finite-size estimates, presented in the right panel.

4.4.2 for the ν_w exponent, we have found that weaker finite-size corrections occur by using the following expression:

$$d_f(L) = \frac{1}{\ln 2} \sinh^{-1}\left[\frac{\overline{\mu}_{2L} - \overline{\mu}_{L/2}}{2\overline{\mu}_L}\right] . \tag{5.1}$$

The obtained $d_f(L)$ values are presented in the right panel of Fig. 5.1 for different dimensions and for both applied disorder distributions. Extrapolating these values for $L \to \infty$, the obtained critical exponents do not depend on the form of disorder for a given dimension. The extrapolated values for d_f/d can be found in the caption of Fig. 5.1, while estimates for the exponents x/d are shown in Table 9.1.

5.2.2 Distribution of the magnetization

In 2D we have also calculated the distribution function of the mass of magnetization clusters over the random samples, $R_L(\tilde{\mu})$, which are shown in Fig. 5.2 for both types of randomness. According to scaling theory, the fractal dimension enters the analysis as $R_L(\tilde{\mu}) = L^{d_f}\tilde{R}(\tilde{\mu}L^{-d_f})$, which is illustrated in the insets of Fig. 5.2 for 2D. Up to a multiplicative constant, the $\tilde{R}(\omega)$ scaling functions are identical for both randomness and can be approximated with an exponential function: $\tilde{R}(\omega) \sim \exp(-\omega/\omega^*)$, ω^* being some randomness dependent value.

5.2.3 Cluster-size distribution

So far we have considered only the magnetization clusters, which show fractal behavior at the critical point. Here we wish to emphasize that even more is true at criticality: the whole ground state structure shows fractal behavior. This may enable the measurement of the fractal dimension even without a proper definition of the special clusters, determining the magnetization. In order to check this, we have analyzed the size-distribution of all clusters, $P_L(\mu)$, which should follow the scaling form: $P_L(\mu) = L^{d_f}\tilde{P}(\mu L^{-d_f})$. According to scaling theory [214] the distribu-

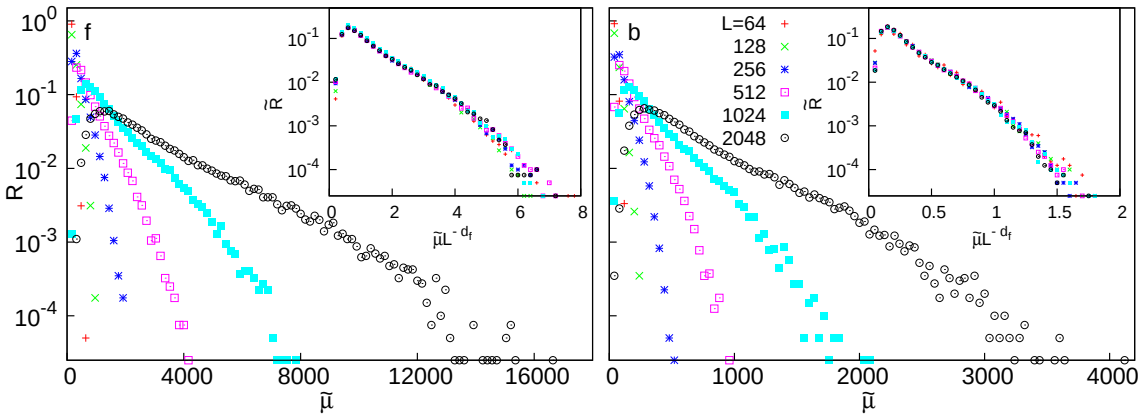

Figure 5.2: Distribution of the μ size of magnetization clusters over the ensemble of random samples in 2D. Left panel: fixed-h randomness, right panel: box-h randomness. The scaled distributions are shown in the insets, where for the fractal dimension the estimate in Table 9.1 is used.

tion has a power-law tail for large arguments, $\tilde{P}(u) \sim u^{-\tau}$, with an exponent $\tau = 1 + \dfrac{d}{d_f}$. The obtained size-distribution of the clusters in 2D, 3D and 4D are plotted in Fig. 5.3 in a log-log scale. The distributions show linear dependence with slopes consistent with our estimates for d_f in Table 9.1: $\tau_{2D} = 3.0(1)$, $\tau_{3D} = 3.56(3)$ and $\tau_{4D} = 4.2(1)$, fitted to the central region of the curves.

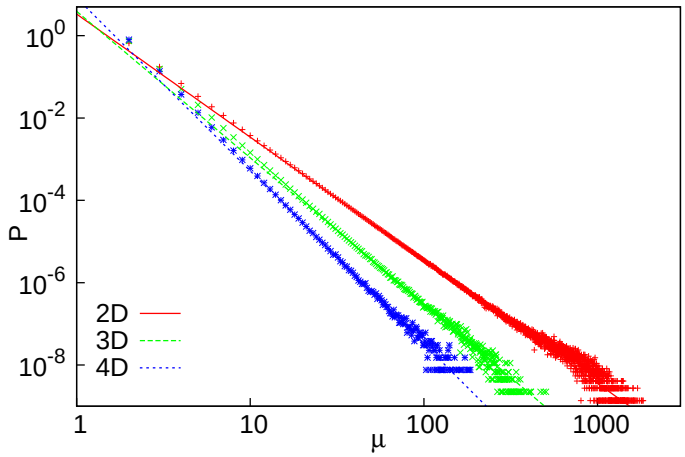

Figure 5.3: Distribution of the mass of the clusters, $P_L(\mu)$, at the critical point for 2D ($L = 1024$), 3D ($L = 128$) and 4D ($L = 48$) with box-h randomness in a log-log scale. The scaling results about the asymptotic slopes of the curves are indicated by straight lines.

5.3 Off-critical region

Close to the critical point the finite-size magnetizations are shown in Fig. 5.4 for 2D, 3D and 4D. For large L in the $\delta < 0$ ferromagnetic phase the magnetization approaches a finite limiting value, whereas for $\delta > 0$ it tends towards zero. According to scaling theory, the magnetization shows the following scaling behavior in the vicinity of the critical point: $m(\delta, L) = L^{-x}\tilde{m}(\delta L^{1/\nu})$.

As a consequence, the finite-size magnetizations can be transformed to a master curve, if one considers the scaled magnetization, $\tilde{m} = mL^x$, as a function of the scaling variable, $\tilde{\delta} = \delta L^{1/\nu}$. This is illustrated in the lower panels of Fig. 5.4, where the exponents x and ν are taken from Table 9.1.

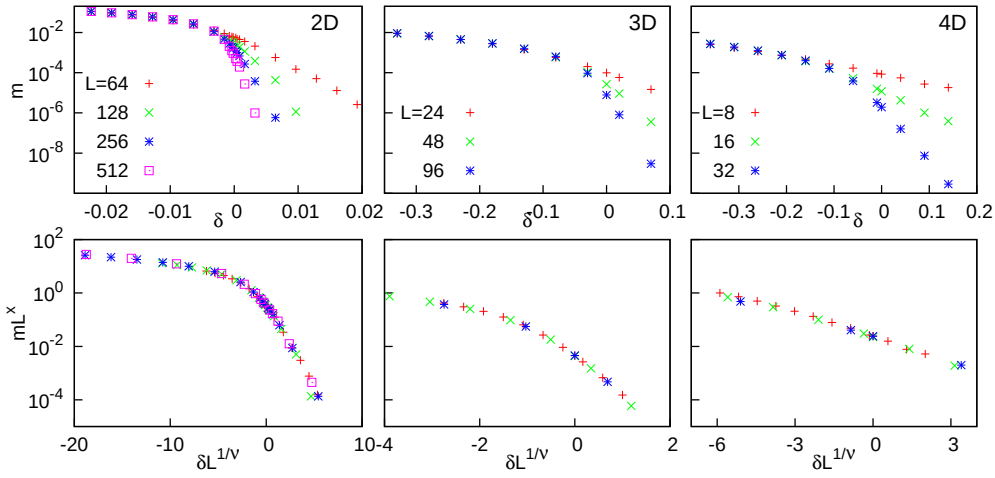

Figure 5.4: Finite-size magnetizations in the vicinity of the critical point (upper panels) for the 2D model (left) with fixed-h disorder and for the 3D (center) and the 4D (right) models with box-h disorder. In the lower panels the scaled magnetization $m(\delta, L)L^x$ is plotted against $\delta L^{1/\nu}$ which yields an excellent data collapse in all cases.

5.4 Discussion

In this chapter we have studied the scaling of the magnetization at the critical point, where the system shows fractal properties. This is not only manifested in the size-distribution and finite-size scaling of the magnetization clusters, but also in the probability distribution of smaller clusters, being characterized by the same d_f fractal dimension at a given d dimension. In order to have quantitative estimates for the asymptotic values of d_f/d, we have measured finite-size effective exponents and made the extrapolation as $1/L \to 0$. Our results are summarized in Table 9.1 together with the other critical exponents. Interestingly, we have found almost no finite-size corrections to the asymptotic values for fixed-h disorder. A good agreement is found in the values for box-h disorder, where there are stronger (even non-monotonic) finite-size corrections[1].

We have also extended the definition of the magnetization for the off-critical region, and studied the scaling regime, where $\delta L^{1/\nu} = \mathcal{O}(1)$. Here we have to note that outside the critical point the correlation length is already finite, thus it is generally not guaranteed that the SDRG method gives exact results. Even so, closely enough to the critical point, our results are expected to be correct, as indicated by the excellent data collapse of the magnetization curves in the vicinity of the critical point in Fig. 5.4.

[1] In 4D even larger system sizes are needed to these corrections to fade out.

Chapter 6

Dynamical scaling

In this chapter we study the properties of low-energy excitations, which are responsible for the dynamical behavior of the system. If a random sample of linear length L has an excitation energy, ϵ_L, then its characteristic time-scale is given by $\tau \sim \epsilon_L^{-1}$. At criticality the dynamics becomes usually very slow, known as the *critical slowing down*. This is generally characterized by a z dynamical exponent, which describes the relation between the length- and time-scale as $\tau \sim L^z$. As a hint, the larger z, the slower the dynamical behavior is. As we already mentioned, at an IDFP, z is formally infinitely large, corresponding to an extremely slow dynamics.

In contrast to static quantities, the SDRG method gives asymptotically exact results for dynamical properties also in the Griffiths-phases, as far as the relaxation time is divergent [181]. According to the scaling relation in Eq. (3.1), it is convenient to use the log-variable $\gamma_L = -\ln(\epsilon_L)$ in the vicinity of the critical point. In the following we study the distribution of γ_L at the critical point — as well as in the disordered and ordered Griffiths-phases — and study its scaling behavior with L.

6.1 Definition of the energy gap

In a finite system, the energy gap is simply given by the value of the 'last decimated', thus smallest effective transverse field. Here we note that an effective J coupling can never be smaller than the smallest effective external field in a finite sample. Even so, at the critical point all the small h and J couplings are expected to scale the same way, thus one can also analyze the scaling of the last decimated effective J couplings, as in [25]. Interestingly, by applying the maximum rule, for each eliminated cluster one can define an 'energy cluster' (see Section 4.2), which contains the given cluster and the renormalization of this connected subgraph gives the same energy value. The form of these energy clusters corresponding to the correlation clusters is illustrated in the right panel of Fig. 4.1.

Outside the critical point we have again some problems with the naive definition given above. In contrast to the case of magnetization, the physical problem now arises in the ordered (ferromagnetic) Griffiths-phase. Namely, in the thermodynamic limit, flipping of the emerging huge magnetization cluster should require vanishing energy and thus ϵ_L must be given by the

second smallest calculated gap. By using replicas of the system, we can easily incorporate this expectation into the usually applied definition: The energy-parameter of a given sample, is given by the smallest effective coupling or transverse field, not considering the transverse field of the correlation cluster (if any). This definition coincides with our aims in the infinite replicated sample, because of the zero external field of the correlation cluster in that case.

6.2 Critical point

The distribution of the log-energy parameter, $\gamma_L = -\log \epsilon_L$, is shown in the upper panel of Fig. 6.1 at the critical point. As a clear indication of infinite disorder scaling the width of the distribution is increasing with L. Referring to Eq. (3.1), the typical value of the log-energy parameter grows with the size as $\gamma_L \sim L^{\psi}$, thus the appropriate scaling combination is given by: $\tilde{\gamma} = (\gamma_L - \gamma_0)L^{-\psi}$. Here γ_0 is a non-universal constant. The scaled distributions are shown in the lower panel of Fig. 3.1. The ψ critical exponent has been estimated from the optimal collapse of the distributions for the largest sizes and coincides with the values given in Table 9.1.

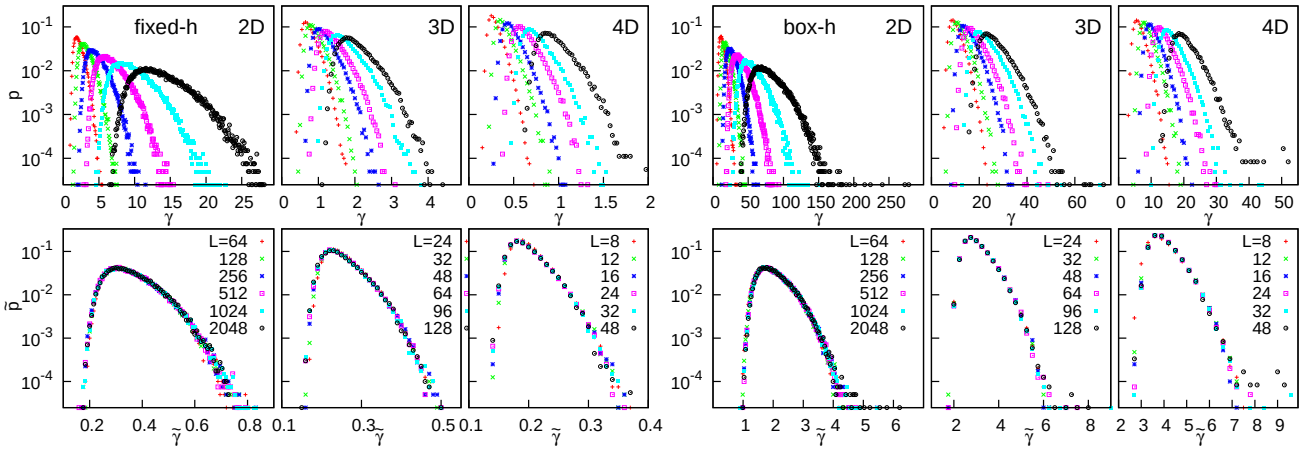

Figure 6.1: Distribution of the log-energy parameters at the critical point in 2D, 3D and 4D for fixed-h randomness (left) and box-h randomness (right). In the lower panel the scaled distributions are shown, as described in the text. The constants in the scaling forms are $\gamma_0 = -1.5(4)$ (2D) $\gamma_0 = -0.33$ (3D) and $\gamma_0 = -0.23$ (4D) for fixed-h randomness and $\gamma_0 = -0.4(1)$ (2D), $\gamma_0 = 3.1$ (3D) and $\gamma_0 = 4.06$ (4D) for box-h randomness.

In order to obtain more accurate estimate for the ψ exponent, we should define finite-size, effective exponents and extrapolate the obtained values as $L \to \infty$. In principle we can use the $\Gamma(L)$ average value of the distributions as well as the $\sigma\gamma(L)$ width of the distributions. At the critical point both quantities diverge as $\sim L^{\psi}$, as illustrated in Fig. 6.2 for 2D with fixed-h disorder.

However, the $\sigma\gamma(L)$ width has the advantage that the γ_0 non-universal constant does not enter the values, thus we use the width in the following. Regarding the $\Gamma(L)$ average value, we mention that there are strong finite-size corrections to the scaling form, thus it is hard to obtain a precise estimate for γ_0. Presumably the best approach in this case is to first

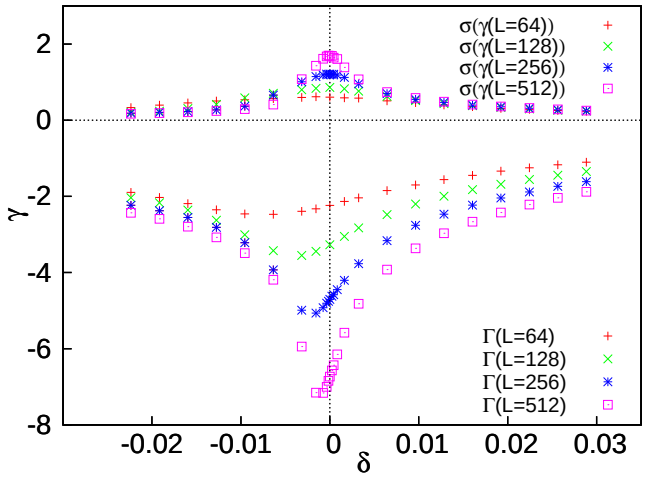

Figure 6.2: The mean and width of the log-gap distributions as the function of the δ control parameter in 2D with fixed-h disorder. At the critical point, both quantities show the same divergence with the system size. However, in the case of the average values (lower curves) also a strong shift can be observed, which hinders the precise determination of ψ in this case.

differentiate $\Gamma(L)$ as the function of L, and calculating the effective exponents thereafter. This way, we have checked in all cases that the obtained exponents are the same based on the average values as calculated from the widths. However, the extra differentiation strongly amplifies the errors of the estimates.

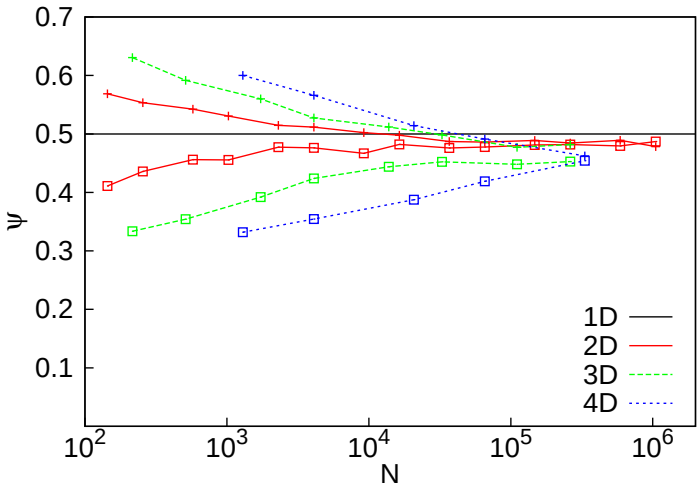

Figure 6.3: Finite-size estimates for the ψ critical exponent in 2D, 3D and 4D obtained from the width of the log-energy distributions for the two different disorders (fixed-h +, box-h ⊡). The solid black line indicates the exact, $\psi = 1/2$ result in 1D. The extrapolated values for $L \to \infty$ are $\psi(2D) = 0.48(2)$, $\psi(3D) = 0.46(2)$ and $\psi(4D) = 0.46(2)$.

The effective exponents, calculated from the widths at two sizes (L and $L/2$) are given in Fig. 6.1 for all dimensions and for both types of disorder. As for other exponents studied before, the estimates for ψ for a given dimension do not depend on the actual form of disorder. The scaling functions in the lower panel of Fig. 6.1 have the same form for both types of disorder and have a heavier tail than in 1D. The corresponding skewness values are: $s_{1D} = 0.64(1)$,

$s_{2D} = 0.80(2)$, $s_{3D} = 0.96(4)$ and $s_{4D} = 1.05(5)$.

6.3 Disordered Griffiths-phase

We have also studied the distribution of the low-energy excitations outside the critical point. In the $\delta > 0$ paramagnetic phase the distribution of γ_L for different sizes are shown in Fig. 6.4 for 2D, 3D and 4D. As seen in this figure the shape of the distribution functions is very similar for different L-s and the curves are merely shifted with $\ln(L)$. This behavior is in agreement with scaling theory in the disordered Griffiths-phase (see Section 1.4.1), where the dynamical exponent is finite, thus $\epsilon_L \sim L^{-z}$. Here $z = z(\delta)$ is a continuous function of the control parameter, $\delta > 0$. Consequently, the appropriate scaling combination is:

$$\tilde{\gamma} = \gamma_L - z \ln L - \gamma_0 \ , \tag{6.1}$$

in terms of which a scaling collapse of the distributions is found, shown in the lower panels of Fig. 6.4. One way to estimate $z(\delta)$ is to analyze the scaling collapse of the distributions, or equivalently to compare the shift of the distributions with L. The obtained results for d/z can be found in the caption of Fig. 6.4.

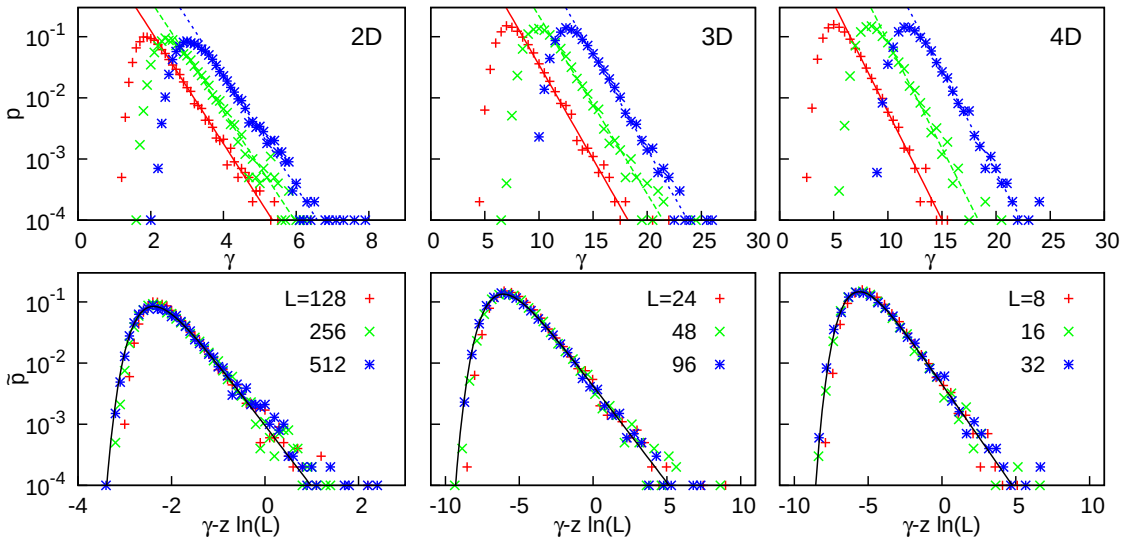

Figure 6.4: Distribution of the log-excitation energies in the disordered Griffiths-phase for 2D with fixed-h randomness and 3D and 4D with box-h randomness in a log-lin scale. The distance from the critical point as well as the slopes of the straight lines indicating the tail of the curves are the following: $\delta = 9.64 \times 10^{-3}$, $d/z = 2.1(2)$ in 2D, $\delta = 0.37$, $d/z = 0.70(3)$ in 3D and $\delta = 0.34$, $d/z = 0.80(5)$ in 4D. In the lower panels the scaled distributions (see text) are shown with the best parameters as follows, $d/z = 2.3$ in 2D, $d/z = 0.73$ in 3D and $d/z = 0.8$ in 4D. The scaled distributions are in all cases well described by the Fréchet distribution (full line) in Eq. (6.2).

There is, however, another way to calculate d/z from the distributions. If the low-energy excitations are localized — which is satisfied for the RTIM in the paramagnetic phase — the

distribution function of the scaled variable, $\tilde{\gamma}$, is expected to follow extreme value statistics [215] and given by the Fréchet distribution [216]:

$$\ln p(\tilde{\gamma} - \gamma_0) = -\frac{d}{z}\tilde{\gamma} - \exp\left(-\tilde{\gamma}\frac{d}{z}\right) + \ln\left(\frac{d}{z}\right) \ . \tag{6.2}$$

Indeed the scaled distributions in the lower panels of Fig.6.4 are well described by this form, having just one free parameter, γ_0. From Eq. (6.2) follows that the asymptotic slope of $\ln p(\gamma)$ vs. γ is just d/z. The independent estimates for d/z, obtained this way, are in good agreement with our previous estimates from the shift of the curves, see Fig. 6.4.

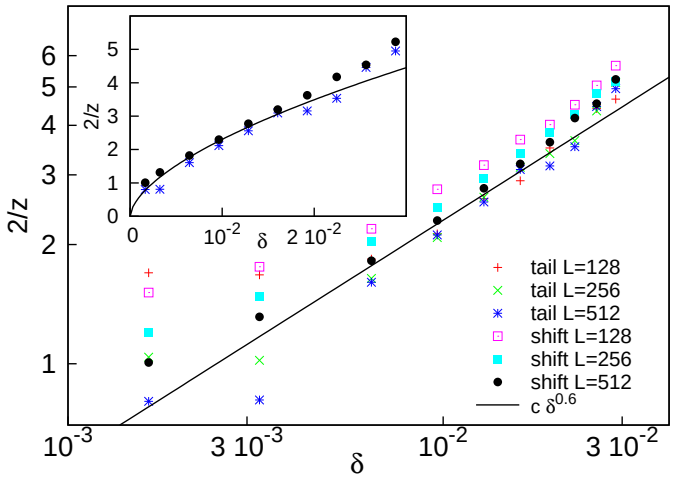

Figure 6.5: Estimates for d/z in 2D with fixed-h randomness, at different points of the disordered Griffiths-phase in a log-log plot. The estimates are calculated either from the shift of the distributions or from their tail at various finite sizes. The straight line with a slope of 0.6 indicates the asymptotic behavior in Eq. (6.3). In the inset we compare our results for the largest size, $L = 512$, with the scaling curve in Eq. (6.3) with $c = 36.5$, in a linear plot.

In 2D we have repeated the previous calculation for several values of δ in the disordered Griffiths-phase and calculated estimates for the dynamical exponent both from the shift of the distributions and from the slope of the tail. These estimates obtained at different L-s are shown in a log-log plot in Fig. 6.5. One can notice that the finite-size corrections are stronger for small δ values, where the correlation length is comparatively larger. According to scaling theory [14, 22], the dynamical exponent for small δ behaves as

$$\frac{d}{z} \propto \delta^{\nu\psi} \ . \tag{6.3}$$

We have checked this relation in Fig. 6.5, where one can identify an approximately linear part for $\delta \leq 0.02$ having a slope ≈ 0.6. This value is compatible with our previous estimates $\nu\psi = 0.60(6)$ using our results from Table 9.1. Unfortunately, we could not check this scaling result in higher dimensions due to strong finite-size effects in the vicinity of the critical point.

6.4 Ordered Griffiths-phase

We have also calculated the distribution of the log-energy parameters in the $\delta < 0$ ordered Griffiths-phase, illustrated in Fig. 6.6 for the 2D and 3D model. Compared to the distributions in the disordered Griffiths-phase in Fig. 6.4, one can notice that in both cases the distributions do not broaden but shift with an L-dependent amount. There are, however, several differences in the two cases. Most importantly, the shift of the distributions in the ordered Griffiths-phase is slower than linear with $\ln(L)$. This is connected to the scaling result that the typical value of the excitation energy, ϵ_L, scales with the size as: $\ln \epsilon_L \sim -\ln^{1/d}(L)$ (see Section 1.4.1). Consequently, the appropriate scaling combination is

$$\tilde{\gamma} = \gamma_L - A \ln^{1/d}(L) - \gamma_0 \, , \tag{6.4}$$

with A and γ_0 being nonuniversal constants. This is to be compared with Eq. (6.1) in the disordered Griffiths-phase. Using the variable in Eq. (6.4), the distributions show a scaling collapse indeed, as illustrated in the lower panels of Fig. 6.6. We should mention, however, that due to finite-size effects we can not obtain an independent estimate of the exponent of the logarithm, being theoretically $1/d$.

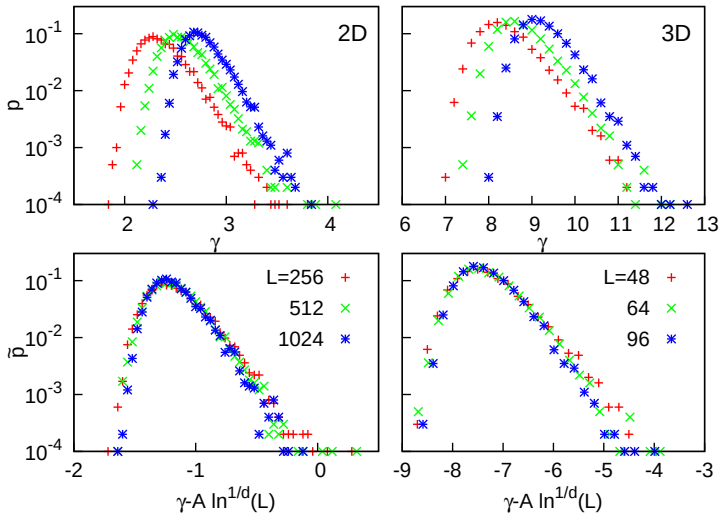

Figure 6.6: Upper panels: Distribution of the log-excitation energies in the ordered Griffiths-phase for 2D systems with fixed-h randomness (left panel at $\delta = -0.01916$) and 3D systems with box-h randomness (right panel at $\delta = -0.33$). In the lower panels the scaled distributions are shown in terms of the variable in Eq. (6.4), with $A = 1.5$ in 2D and $A = 10.0$ in 3D.

Also the shape of the scaled distributions are different in the two Griffiths-phases. In the disordered Griffiths-phase the distributions in Fig. 6.4 approach a linear asymptotics from above, on the contrary in the ordered Griffiths-phase in Fig. 6.6 the points bend below a straight line. This is compatible with the scaling result that asymptotically $\ln p(\tilde{\gamma}) \sim -\tilde{\gamma}^d$. In fact, our data in Fig. 6.6 are still not in the asymptotic regime, but the tail of the distribution clearly decreases faster than linear for large sizes.

6.5 Discussion

In this chapter we analyzed the dynamical scaling at the critical point, where it shows ultraslow, IDFP behavior in all dimensions, characterized by a universal ψ critical exponent, instead of the conventional z dynamical exponent. Interestingly the obtained ψ exponents for all studied dimensions are close to $1/2$, which is the exact value in 1D. This observation can be explained by the fact that the *energy clusters*, which are connected subgraphs related to the energy-parameter of a spin cluster (introduced in Section 4.2), are almost one dimensional objects in all studied cases, see in the right panel of Fig. 4.1. The measured fractal dimensions are approximately 1.28 in 2D, 1.4 in 3D and 1.6 in 4D. Additionally, in higher dimensional systems, the original h and J values inside the energy cluster are strongly correlated, due to the fact that these lead to an extremely small energy gap compared to the rest of the system. This emerging correlation further decreases the effective dimensionality of the relevant clusters in all dimensions, leading to the observed ψ exponents.

To obtain information about the off-critical dynamics of the system we have also studied the scaling behavior of the excitation energies in both the ordered and disordered Griffiths-phases. Being the first systematic investigations in higher dimensions, our results show a good accordance with the expected scaling results in the Griffiths-phases. Remarkably, the ordered and disordered Griffiths-phases show generally different behavior in higher dimensional systems.

Closing this section we note that the dynamical exponent enters into the singularities of different physical quantities also in the Griffiths-phases. For example at low-temperature the susceptibility behaves in the disordered Griffiths-phase as: $\chi(T) \sim T^{d/z-1}$, while the specific heat has the form of $C_v \sim T^{d/z}$. The same expressions in the ordered Griffiths-phase are: $\chi(T) \sim \exp\left(-C|\log T|^d\right)/T$ and $C_v \sim \exp\left(-C'|\log T|^d\right)$. More details about the scaling relations in the Griffiths-phases can be found in [14] and [116].

Chapter 7

Erdős-Rényi random graphs

Here we come back to the question posed in the Introduction about the possible value of the upper critical dimension, d_u of the problem, above which there is no infinite disorder fixed point. Due to our fast SDRG algorithm, we can study the same number of spins in any dimensions. Thus technically, there is nothing to stop us from studying the 5 and higher dimensional lattices. However, due to finite-size corrections we have to achieve a large enough linear size as well, in order to obtain reliable results about the asymptotic behavior. The first and most important problem is to precisely locate the critical point, without this, we can not go further with our analysis. As we saw so far, already in 4D the most significant error stemmed from this step. As a rule of thumb, we would need roughly at least $L \approx 100$ in any dimensions. In 5D this would require about 3000 times larger computational power, than available for us. Instead of waiting for this to realize, we tried to address directly the infinite dimensional problem, to check the presence of an IDFP. Naturally, we did not intend to get precise estimates for the critical exponents in this case.

In the following we consider Erdős-Rényi random graphs [204] with a finite coordination number, which are representing the large-dimensional limit of our lattices. Generally an Erdős-Rényi random graph consists of N sites and $kN/2$ edges, which are put in random positions. In order to have a percolating random graph we should have $k > 1$. Here we have used $k = 3$, but some control calculations had also been done with $k = 4$ leading to the same results. The linear size of such a random graphs grows as $L \sim \log N$ in contrast to the finite dimensional case, where $L \sim N^{1/d}$. Due to the random structure and infinite dimensionality of Erdős-Rényi graphs we had to modify some parts of the analysis used in Chapter 4.

7.1 Determination of the critical point

As for $d \leq 4$ we have calculated sample dependent pseudo-critical points, but now in the doubling method the two identical copies of the sample have been connected by $N/2$ random links. To be more precise, we replaced an (i, j) link in the original sample and (i', j') in the replicated sample with the new links (i, j') and (i', j). This choice is the direct extension of the rules used in finite dimensional systems with periodic boundary conditions. Generally, the

number of interconnecting links was half of the number of surface spins in any case. The relative amount of surface spins increases with the dimensionality, until in the Erdős-Rényi graphs all the (statistically equivalent) spins are assumed to be surface spins.

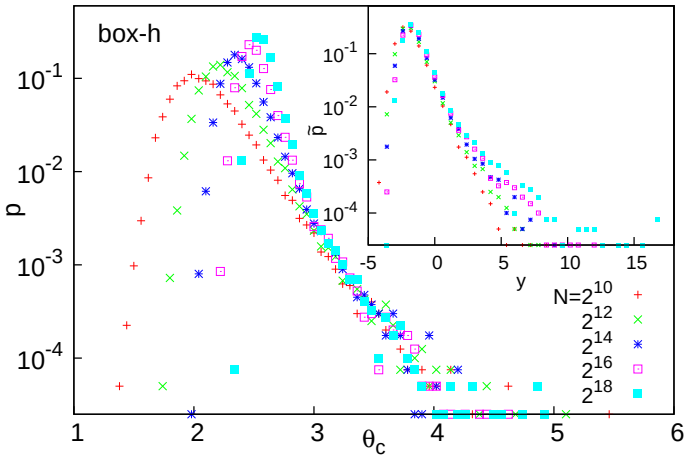

Figure 7.1: Distribution of the pseudo-critical points, $\theta_c(N)$, for the Erdős-Rényi random graphs with box-h randomness. In the inset the scaled distributions are shown as a function of $y = (\theta_c(N) - \theta_c)N^{1/\omega}$ with $\omega = 6$.

The distribution of the calculated pseudo-critical points for different values of N are shown in Fig. 7.1. The general behavior of the distributions is similar to that found for lattices, see Fig. 4.3, but in the present case for large θ_c values there is an N-independent background of the distributions. This background is probably due to the random nature of links between the replicas[1]. This background, however, has a very small weight to the distributions and does not influence the analysis of the properties of the pseudo-critical points. Concerning Fig. 7.1 we have measured the shift, $\left|\theta_c - \overline{\theta_c}(N)\right| \sim N^{-1/\omega_s}$ and the width $\Delta\theta_c(N) \sim N^{-1/\omega_w}$ of the distributions, in analogy with the finite dimensional problem with $\omega_s = d\nu_s$ and $\omega_w = d\nu_w$. From two-point fits we have calculated effective exponents (see Fig. 7.2) from which we have obtained the estimates, $\omega_s = 4.5(15)$ and $\omega_w = 7.8(20)$, which are valid for both type of randomnesses. We note that the relative error of the estimates is somewhat larger than for lattices, but still the two exponents of the distribution may agree within the estimated errors, yielding $\omega = 6(3)$. Using this value, the distribution of the scaled variable $y = (\theta_c(N) - \theta_c)N^{1/\omega}$ shows a good scaling collapse as illustrated in the inset of Fig. 7.1. The estimated locations of the critical point for the two applied disorder are given in Table 9.1.

7.2 Magnetization

We have studied the fractal properties of the correlation cluster, the average mass of which is found to scale at the critical point as: $\overline{\mu}(N) \sim N^{\vartheta}$. This is in analogy with the finite dimensional problem with $\vartheta = d_f/d$. From two-point fits we have obtained effective values for ϑ, which

[1]Typically in each doubled system there are special subgraphs generated, such as 4-point loops, which may form strong correlation clusters.

are shown in Fig. 7.2 and which are extrapolated to $\vartheta = 0.17(5)$. We note that according to scaling theory the magnetization exponent of the RTIM on the Erdős-Rényi graph is given by: $\beta = \omega(1-\vartheta) = 5(2)$.

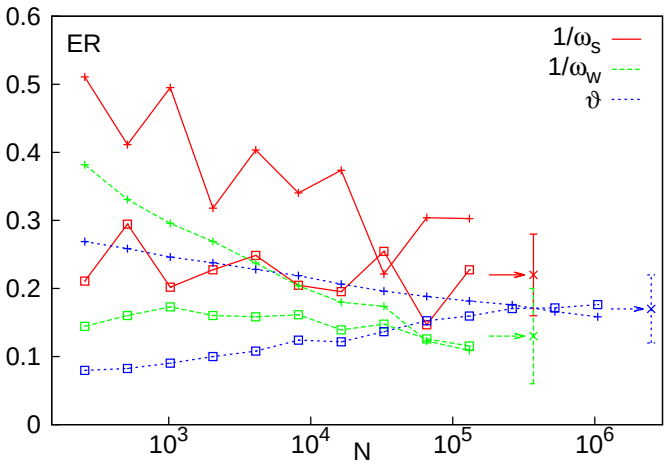

Figure 7.2: Finite-size estimates for the critical exponents in Erdős-Rényi random graphs for both disorders (fixed-h +, box-h ⊡).

7.3 Dynamical scaling

We have also investigated the distribution of the log-energy parameters at the critical point, which is shown in Fig. 7.3 for both applied disorder. In order to see the possible existence of infinite disorder scaling we have measured the width of the distributions, which are shown in the lower left panel of Fig. 7.3 as a function of $\log N$. As seen in the figure the width of the distribution can be parametrized as $W_0 + W_1 \ln^{\omega} N$, where the constant is $W_0 \approx 0$ for fixed-h randomness and it is $W_0 \approx 1.2$ for box-h randomness. In both cases the exponent in the logarithm can be estimated as: $\omega = 1.3(2)$, thus the increase of the width of the distribution is somewhat larger than linear in $\ln N$. As a good scaling combination we have here $\tilde{\gamma} = (\gamma(N) - \gamma_0)(\ln N/N_0)^{-\omega}$ (γ_0 and N_0 are constants), which is illustrated by the excellent data collapse in the lower right panel of Fig. 9.1 for fixed-h randomness[2]. This evidence for broadening distributions justifies that even for the infinite dimensional Erdős-Rényi graphs the critical behavior of the RTIM is controlled by a (logarithmically) infinite disorder fixed point. Therefore, we conclude that the upper critical dimension of infinite disorder scaling of the RTIM is most probably $d_u = \infty$.

We note that although the graph theoretic diameter of an Erdős-Rényi graph grows typically as $\ln N$, there is not a direct correspondence between the L linear size of the lattices studied earlier and $\ln N$ for each sample. Consequently, the obtained ω exponent is not in direct analogy with ψ.

[2]With box-h randomness the illustration of the data collapse is hindered by the relatively large value of W_0.

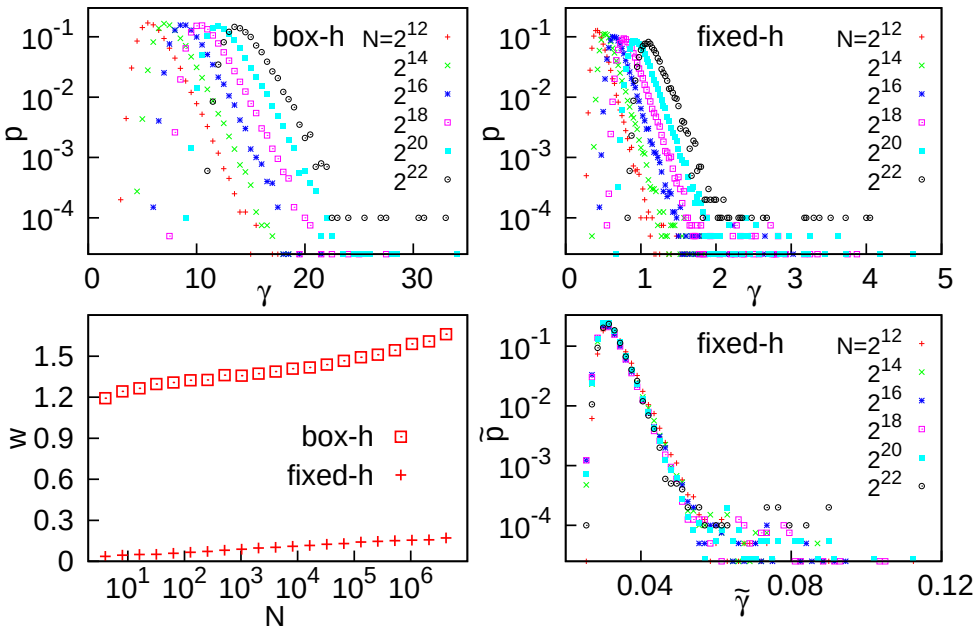

Figure 7.3: Distribution of the log-energy parameters at the critical point as a function of the size of the Erdős-Rényi graphs for box-h randomness (upper left panel) and fixed-h randomness (upper right panel). In the lower left panel the width of the distributions is shown as a function of $\ln N$ for both disorders. In the lower right panel the scaled distributions are shown for fixed-h randomness, with $\gamma_0 = -0.5$ and $\ln N_0 = -5$, see text.

7.4 Discussion

Our numerical RG results indicate that the critical behavior of the random transverse-field Ising model in 1, 2, 3 and 4 dimensions as well as in the Erdős-Rényi random graph is controlled by infinite disorder fixed points. We note that the large-d limit of the problem is qualitatively relevant for models with long-range interactions. In this respect the critical behavior of the (non-random) $LiHoF_4$ system has been the subject of intensive Monte Carlo simulations [217]. The obtained critical exponents also influence the low temperature behavior as seen in Section 3.1. For instance, the $\chi(T)$ susceptibility and the $C_V(T)$ specific heat are expected to scale as $\chi(T) \sim \exp\left(C|\log T|^{1/\omega}\right)/T$ and $C_V(T) \sim \exp\left(C'|\log T|^{1/\omega}\right)$ at $\delta = 0$.

Remarkably, our analysis for Erdős-Rényi random graphs may also be interesting from an other point of view. The random contact process, which is expected to belong to the same universality class as the RTIM for strong enough disorder [11, 12] has been simulated recently in Erdős-Rényi graphs. For bimodal disorder the critical behavior of the system is found to be the same as the non-random model [218]. This result, which differs from our SDRG results for the RTIM, is probably due to the fact that the applied disorder in the simulations was not in the strong disorder regime. Nevertheless, our study is one of the first steps towards the understanding of properties of real epidemics over complex (e.g. social or computer) networks with quenched disorder. Note that quenched disorder is an inevitable feature of real networks, having different sites with different healing rates as well as highly inhomogeneous infection rates[3], both varying only slowly (if at all) during an experiment.

[3]Determined by e.g. the strength of the physical or social connections.

Chapter 8

Entanglement entropy

'I would not call [entanglement] *one*, but rather *the* characteristic trait of quantum mechanics, the one that enforces its entire departure from classical lines of thought.'
Erwin Schrödinger

To study the entanglement properties of quantum many body systems is a promising concept to understand their topological and universal properties, in particular in the vicinity of a quantum phase-transition point [30, 219, 220]. Generally the entanglement between the subsystem, $\mathcal{A}$ and the rest of the system, $\mathcal{B}$, in the ground state, $|\Psi\rangle$ is quantified by the von Neumann entropy of the reduced density matrix, $\rho_{\mathcal{A}} = \mathrm{Tr}_{\mathcal{B}}|\Psi\rangle\langle\Psi|$ as [30]:

$$\mathcal{S} = -\mathrm{Tr}_{\mathcal{A}}\left(\rho_{\mathcal{A}} \log_2 \rho_{\mathcal{A}}\right) \ , \tag{8.1}$$

called as the *entanglement entropy* of the subsystem. The $\mathcal{A}$ subsystem is usually a connected region having a cubic shape (interval in 1D, square in 2D), with linear size ℓ. We note here that the interval used in 1D may be generalized for higher dimensional systems in other ways as well, as illustrated in Fig. 8.1. We show later that in order to understand the entanglement entropy of a cubic subsystem, it is highly beneficial to study also subsystems having different shapes, as indicated in this figure.

Generally $\mathcal{S}$ scales with the area of the interface separating $\mathcal{A}$ and $\mathcal{B}$, $\sim \ell^{d-1}$ for cubic subsystem, known as the *area law*. In some cases, however, there are singular corrections to the area law. In 1D systems, where the area law predicts a constant value, $\mathcal{S}$ is logarithmically divergent at a quantum critical point [31–33]: $\mathcal{S}(\ell) = \frac{c}{3}\log_2 \ell + cst.$ Here the c prefactor is universal, being the central charge of the conformal field theory. Recently one considers also generalizations to Rényi entropy and the properties of the entanglement spectrum [221].

In higher dimensions our understanding about bipartite entanglement is far less complete, the known results are almost exclusively about 2D models. Considering non-interacting systems, for free bosons the area law [222] is found to be satisfied even in gapless phases [223, 224]. On the contrary, for gapless free-fermionic systems with short-range hoppings and a finite Fermi surface there is a logarithmic factor to the area law [225, 226]. In interacting 2D systems the area law is generally found to be satisfied, but in gapless phases and in quantum critical points there are additional logarithmic terms, which are expected to be universal. This has

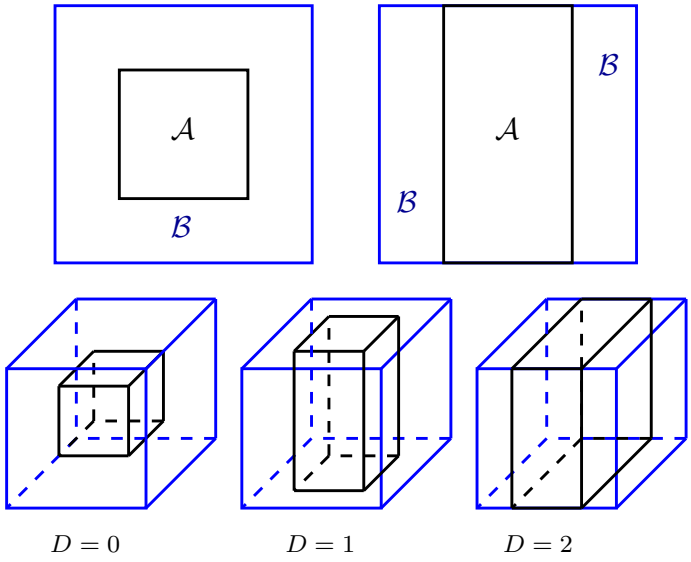

Figure 8.1: Illustration of the two studied shape of the $\mathcal{A}$ subsystems in 2D (upper panels): $\ell \times \ell$ square subsystem (left) and $\ell \times L$ stripe (right). The lower panels show the three studied subsystem geometries in 3D: cube ($D = 0$), column ($D = 1$) and slab ($D = 2$). Note that periodic boundary conditions were applied in all directions.

been demonstrated for the 2D transverse-field Ising model [227] and for the antiferromagnetic Heisenberg model [228,229]. For the latter the logarithmic terms are associated to two sources: i) corners on the boundary of the subsystem and ii) non-trivial topology in the bulk. There is another class of 2D critical systems described by 2D conformal field theory, the prototype being the square lattice quantum dimer model [230]. For these models non-perturbative analytical and numerical results are available and the log-correction to the area law is shown to be universal and related to corners [231–233].

Besides pure systems there are also investigations about the entanglement properties of quantum models in the presence of quenched disorder [234]. For random systems in 1D (RTIM, random antiferromagnetic Heisenberg and XX models, etc.) the critical point is controlled by an IDFP [20–22], which can be conveniently studied by the SDRG method [14,176,177]. Using this approach logarithmic entanglement entropy is found with a universal prefactor [34], which has been numerically checked by density-matrix renormalization [235] and by free-fermionic methods [236]:

$$\mathcal{S}(\ell) = \frac{c}{3} \log_2 \ell + k \,, \tag{8.2}$$

where k is a non-universal constant, depending also on the form of disorder, whereas the prefactor of the logarithm, c, which is also called as the effective central charge, is universal and given by: $c = \ln 2/2$ for the RTIM.

After decimating all degrees of freedom in the numerical application of the SDRG method, the ground state of the RTIM is found as a collection of independent ferromagnetic clusters of various sizes. As mentioned in Section 3.2, each such cluster is in a Greenberger-Horne-Zeilinger state: $\frac{1}{\sqrt{2}}(|\uparrow\uparrow\ldots\uparrow\rangle + |\downarrow\downarrow\ldots\downarrow\rangle)$, due to the very broad distribution of the effective couplings and transverse fields at the IDFP. Consequently, the entanglement entropy between $\mathcal{A}$ and $\mathcal{B}$

is given by such renormalized spin clusters, which contain sites both in $\mathcal{A}$ and in $\mathcal{B}$, and the cluster is eliminated at some point of the renormalization [24, 27, 34]. Here we recall that the spatial structure of the spin clusters is different in the $\delta < 0$ ferromagnetic phase, when there is a giant cluster and in the $\delta > 0$ paramagnetic phase, when all clusters have a finite extent.

Let we first consider the simplest case of two-point clusters of form $|\Psi\rangle = 1/\sqrt{2}(|\uparrow\uparrow\rangle + |\downarrow\downarrow\rangle)$, which may give contribution to the entanglement entropy, if the two points fall into different subsystems. The $\rho = |\Psi\rangle\langle\Psi|$ density matrix can be written in the form of

$$\rho = \frac{1}{\sqrt{2}} \begin{pmatrix} 0 & 0 & 0 & 0 \\ 0 & 1 & 1 & 0 \\ 0 & 1 & 1 & 0 \\ 0 & 0 & 0 & 0 \end{pmatrix}, \tag{8.3}$$

from which the reduced density matrix of the first spin is given by $\rho_{\mathcal{A}} = \begin{pmatrix} 0.5 & 0.5 \\ 0.5 & 0.5 \end{pmatrix}$, leading to $\mathcal{S} = \log_2 2 = 1$. This result is even generally true for the RTIM: each cluster contributes by an amount of $\log_2 2 = 1$ to the entanglement entropy if it is shared by the subsystems, and 0 otherwise. Thus calculation of the entanglement entropy for the RTIM is equivalent to a cluster counting problem. This is illustrated in Fig. 8.2 for ladders and Fig. 8.6 in 2D (lower left and middle panels).

In 2D the entanglement entropy of the RTIM has been studied by the SDRG method in two papers with conflicting results at the critical point. Lin *et al* [24] has used periodic systems up to linear size $L = 64$ and the numerical results are interpreted in terms of a double-logarithmic factor to the area law: $\mathcal{S} \sim \ell \ln \ln \ell$. In a subsequent study Yu *et al* [27] has used open systems up to $L = 160$ and the numerical data are fitted with a logarithmic correction to the area law: $\mathcal{S} = a\ell + b \ln \ell$. This type of choice of the singularity is motivated by the similar form of the entropy in 2D conformally invariant models [231–233], although the logarithmic correction is not attributed to corner effects but to percolation of correlated clusters.

Being aware of these subtleties in 2D, we approach it more carefully, starting with the analysis of the ladders with a w width [38]. After this, we revisit the problem in the 2D RTIM using our improved SDRG method presented in Section 2.3 [40, 41]. It turns out that the simple cluster counting problem is in fact more time consuming, than our improved SDRG method to determine the underlying cluster structure. In order to achieve the same system sizes, as in our previous studies concerning the critical exponents, we had to work out a sophisticated analytical-numerical hybrid algorithm, presented in the Appendix. Having at hand these tools, we addressed the following basic questions in 2, 3 and 4D.

- How the criticality of the RTIM is manifested in the singular behavior of the entanglement entropy?
- What is the physical origin of this singularity, corner and/or bulk effects?
- Is this singularity universal and independent of the form of disorder?

- Is it related to the diverging correlation length?

8.1 Entanglement entropy of ladders

Here we study numerically the critical ladder systems with various number of legs and try to identify the cross-over between one- and two dimensions. We consider a block, $\mathcal{A}$, which contains all the w legs and has a length, $\ell \ll L$. Consequently the $\mathcal{A}$ subsystem has two parallel lines of width, w, at which it has contact with the rest of the system, $\mathcal{B}$.

To illustrate the ℓ dependence of the entanglement entropy, we show $\mathcal{S}$ as a function of $\ln \ell$ for different number of legs for $L = 4096$ in Fig. 8.3. The central parts of the curves are very well linear having approximately the same slope, which is consistent with the exact result for the $w = 1$ chain geometry. Thus we conclude that the effective central charge, $c(w)$, does not depend on the number of legs.

In the next step we fix $c(w) = \ln 2/2$, calculate the non-universal term in Eq. (8.2): $k(w, \ell) = \mathcal{S}(w, \ell) - \frac{\ln 2}{6} \log \ell$ and take its limit, $k(w)$, for large ℓ (but still with $\ell \ll L$). As illustrated in the upper inset of Fig. 8.3, the ℓ-dependent correction term is approximated as $\log \ell/\ell$. The $k(w)$ asymptotic terms are shown for different number of legs in the lower inset of Fig. 8.3. One can see that starting with the chain, $w = 1$, first $k(w)$ is decreasing, has a minimum around $w = 3$ and then starts to increase linearly as $k(w) = 0.0256(5)w + 0.148(5)$. This linear increasement is compatible with the area law in 2D, where $w \sim L$, leading to slab subsystems seen in Fig. 8.1. Formally one could also expect an additive logarithmic correction to the area law, even so, our data can not be used to make these or further predictions.

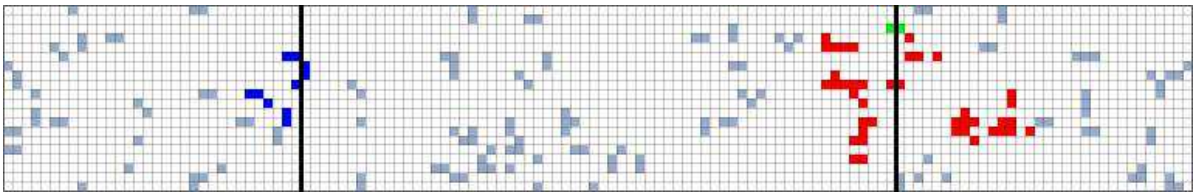

Figure 8.2: As an explicit example, we show here the structure of the decimated spin clusters at the critical point of a ladder of $w = 20$ and $L = 128$, which is divided into two equal blocks with $\ell = 64$, the boundary of which is indicated by thick vertical lines. In this sample there are three clusters, denoted by blue, red and green colors, which contain sites at both blocks and thus result in an entropy $\mathcal{S} = 3$.

8.2 Entanglement entropy in higher dimensions

We have calculated the entanglement entropy of the RTIM at the critical point in finite hypercubic samples of linear size, L with full periodic boundary conditions, the largest sizes for box-h (fixed-h) disorder being 2048 (1024), 128 (64) and 48 (24) for 2D, 3D and 4D. In the case of fixed-h disorder the clusters are more compact, containing more sites, thus the analysis of the entropy is more involved. We have considered d different geometries, in which in $0 \leq D \leq d-1$

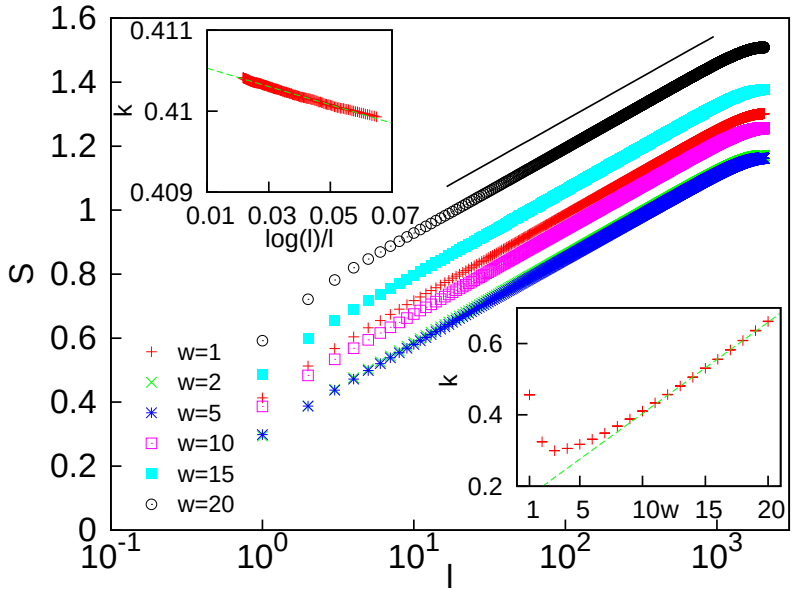

Figure 8.3: The log-ℓ-dependence of the entanglement entropy at the critical point of ladders for different number of legs, w, at $L = 4096$. The linear part of the curves has approximately the same slope, which is consistent with the 1D results, $\ln 2/6$, as indicated by a full straight line. Upper inset: the non-universal part of the critical entropy, $k(w, \ell)$, for the $w = 10$-leg ladder and its extrapolation for $\ell \gg w$ (but $\ell \ll L = 4096$) with a correction term of $\sim \log \ell/\ell$. Lower inset: the asymptotic value of the non-universal part of the critical entropy, $k(w)$, as a function of w. Asymptotically there is a linear w-dependence, which is shown by a broken (green) straight line.

directions $\mathcal{A}$ extends to the full length of the system, L and has PBCs, whereas in the other directions its length is $\ell < L$. The three possible geometries for 3D are illustrated in the inset of Fig. 8.1. Only in the cube geometry with $D = 0$ there are corners, whereas for $D = d-1$ in the slab geometry the interface contains no edges. For a given random sample and for each geometry we have averaged the entanglement entropy for every possible position (and orientation) of $\mathcal{A}$ and subsequently we have averaged over several samples. The typical value of realizations was 40000 but even for the largest sizes we had at least 10000 samples. For a given realization the extra computational time needed to perform the cluster counting problem for the entropy is generally $\mathcal{O}(L^{2(d-D)})$, but we could considerably speed up this method as described in the Appendix. Note that without these improvements, the running time for cubic subsystems with $D = 0$ scales as $\mathcal{O}(N^2)$, being $\sim 10^6$ times slower than the $\mathcal{O}(N \log N)$ performance of the underlying improved SDRG algorithm.

8.2.1 Slab geometry

We start our investigations in the slab geometry, where the entanglement entropy of a sample averaged over all positions can be written in a simple closed form in terms of cluster statistics. Here we announce the result, for details see the Appendix. In this algorithm we consider that axis, say the z-axis, which is perpendicular to the surface of the slab and we measure

the z-coordinate of the points of the clusters. For each cluster we arrange the different z values as $z_1 < z_2 < \cdots < z_k$ and define the difference between consecutive z-values, $h_i = \min[z_{i+1} - z_i, L - (z_{i+1} - z_i)]$, $i = 1, 2, \ldots k-1$; $h_k = \min[z_k - z_1, L - (z_k - z_1)]$. Repeating this measurement for all clusters we calculate the statistics of the h_i differences: $n(j)$ being the number of distances with $j = h$. The position averaged entanglement entropy of the sample is then given for $\ell \leq L/2$, as:

$$\mathcal{S}^{(d)}_{\rm slab}(L, \ell) = \frac{1}{L} \sum_{i=1}^{\ell} \sum_{j=i}^{L/2} n(j) \; . \tag{8.4}$$

This type of algorithm works in $\mathcal{O}(L)$ times, which is to be compared with the performance of the direct cluster counting approach: $\mathcal{O}(L^2)$. This algorithm can also be applied for ladders and chains, being technically at the same complexity level as a slab subsystem in any finite dimension, d. Generally, the area is independent of ℓ in the slab geometry, similarly to the case of ladders, thus any singular contribution to the area law can only be of bulk origin.

In our study we have fixed L to its largest value and calculated the entropy per area, $a_{d-1}(L, \ell)$ for varying ℓ. For $1 \ll \ell \ll L$ we have found that $a_{d-1}(L, \ell)$ approaches a constant with a correction term: $\sim \ell^{-d+1}$. To illustrate this relation we have calculated the finite difference: $\delta\mathcal{S}^{(d)}_{\rm slab}(L, \ell) = \mathcal{S}^{(d)}_{\rm slab}(L, \ell+1) - \mathcal{S}^{(d)}_{\rm slab}(L, \ell)$ as a function of ℓ, which has the behavior: $\delta\mathcal{S}^{(d)}_{\rm slab}(L, \ell) \sim \ell^{-d}$ as shown in Fig.8.4 for 2D, 3D and 4D. This type of *non-singular* contribution to the entropy in the slab geometry can be interpreted in the following way. Due to the finite width of the slab only those correlated domains can effectively contribute to the entropy, which have a finite extent $\xi \lesssim \ell$. Much larger clusters have typically no sites inside the slab, being fractals with a d_f fractal dimension listed in Table 9.1. Finite-size corrections are due to clusters with $\xi \approx \ell$, the number of these blobs scales as $n_{bl} \sim (L/\ell)^{d-1}$ and each has the same correction to the entropy, which then scales as $\sim n_{bl}$ in agreement with the scaling Ansatz and with the numerical data in Fig. 8.4.

Here we note that in the SDRG reasoning used in [24], which led to a $\ln\ln\ell$ multiplicative correction in 2D, one assumed the existence of several (ℓ-dependent number of) independent large clusters in a $\xi \approx \ell$ blob, which is in contradiction with the results of the present large-scale calculation. We have also directly checked the possibility for a log-log correction in 2D for square subsystems, indicated in Fig. 8.5. Although for small system sizes ($L \leq 50$) this yields a reasonable fit, a clear deviation is seen later.

8.2.2 Columnar geometries

In higher dimensions there are multiple subsystem geometries, in which the subsystem spans the system in at least one, but at maximally $d-2$ directions. In such a columnar geometry, see the lower middle panel in Fig. 8.1 for 3D, there are corrections to the area law due to edges. Let us consider an E-dimensional edge ($1 \leq E < d-1$) with a total surface, $f_E \sim L^E$, so that its contribution to the entropy is given by: $a_E f_E$. We have found, that the a_E prefactors have alternating signs: $a_E/a_{E-1} < 0$ and $a_{d-2} < 0$. Here using the same reasoning as in the slab geometry the correction to the edge contribution per surface is given by: $a_E - a_E(\ell) \sim \ell^{-E}$,

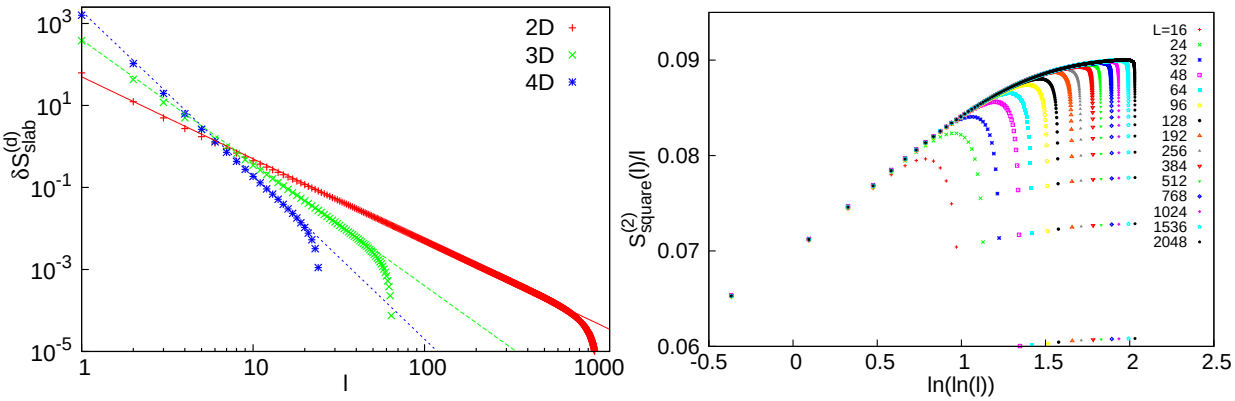

Figure 8.4: Left figure: finite difference of the entropy in the slab geometry, $\delta\mathcal{S}^{(d)}_{\rm slab}(L,\ell)$, as a function of the width ℓ for $d = 2, 3$ and 4 for the largest sizes, L, for box-h disorder. (The error is smaller than the size of the symbols.) The asymptotic forms, $\sim \ell^{-d}$, are indicated by straight lines. Right figure: $\mathcal{S}^{(2)}_{\rm square}(\ell)/\ell$ as the function of $\ln\ln\ell$ in 2D for box-h disorder shows a clear deviation from the log-log form in [24].

which result has been checked numerically. Thus we can conclude that the contributions to the entropy due to edges are also *non-singular* and singular contributions can only be obtained at corners.

8.2.3 Cubic geometry

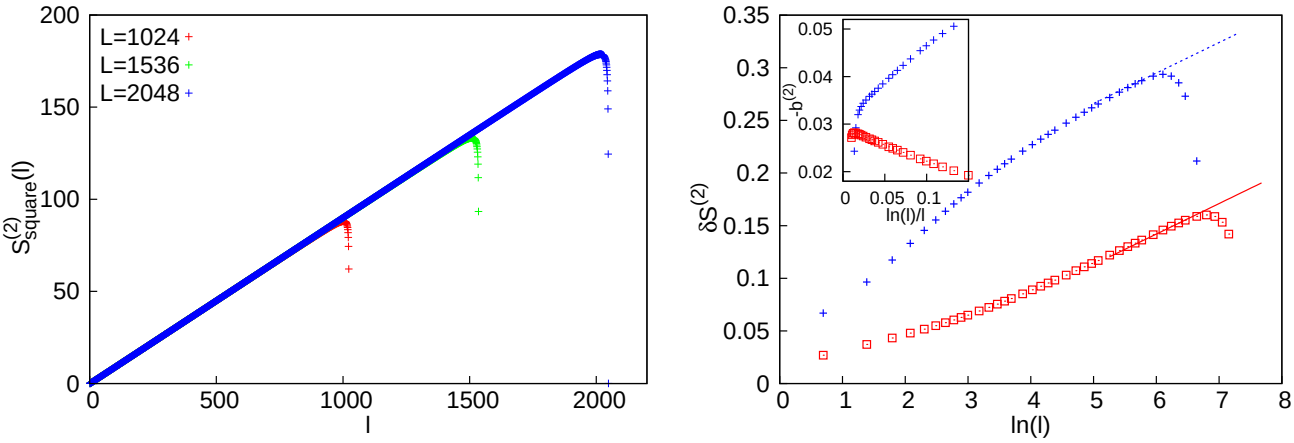

Figure 8.5: $\mathcal{S}^{(2)}_{\rm square}(\ell)/\ell$ as the function of ℓ in 2D for box-h disorder shows has a very well linear behavior as a clear indication of the area law (left figure). There are however weak additive corrections as seen in the right figure for fixed-h (+, $L = 1024$) and box-h ($\boxdot$, $L = 2048$) disorders as the function of $\ln\ell$. The asymptotic behaviors for large ℓ are indicated by straight lines having the same slopes: $b^{(2)} = -0.029$. Inset: effective, ℓ-dependent $-b^{(2)}$ parameters obtained from two-point fits.

In order to check the corner contributions to the entropy, $\mathcal{S}^{(d)}_{\rm cr}(\ell)$, we study here cube subsystems, as shown in the right panels of Fig. 8.1. In this case we write $\mathcal{S}^{(d)}_{\rm cube}(\ell)$ in the general

case as:

$$\mathcal{S}^{(d)}_{\rm cube}(\ell) = a_{d-1} f_{d-1} + \sum_{E=1}^{d-2} a_E f_E + \mathcal{S}^{(d)}_{\rm cr}(\ell) \; . \tag{8.5}$$

where the corner contribution has the sign: $(-1)^{d+1}$, which is opposite to the sign of a_1. In 2D, when the subsystem is a square, the second term in Eq. (8.5) is missing and we obtain accurate estimates for the corner contribution by evaluating the difference: $\delta\mathcal{S}^{(2)}(\ell) \equiv \mathcal{S}^{(2)}(\ell) - 2\mathcal{S}^{(2)}(\ell/2) \approx \mathcal{S}^{(2)}_{\rm cr}(\ell) - 2\mathcal{S}^{(2)}_{\rm cr}(\ell/2)$. This is presented in Fig. 8.5 as a function of $\ln \ell$ for both disorder using the largest system sizes.

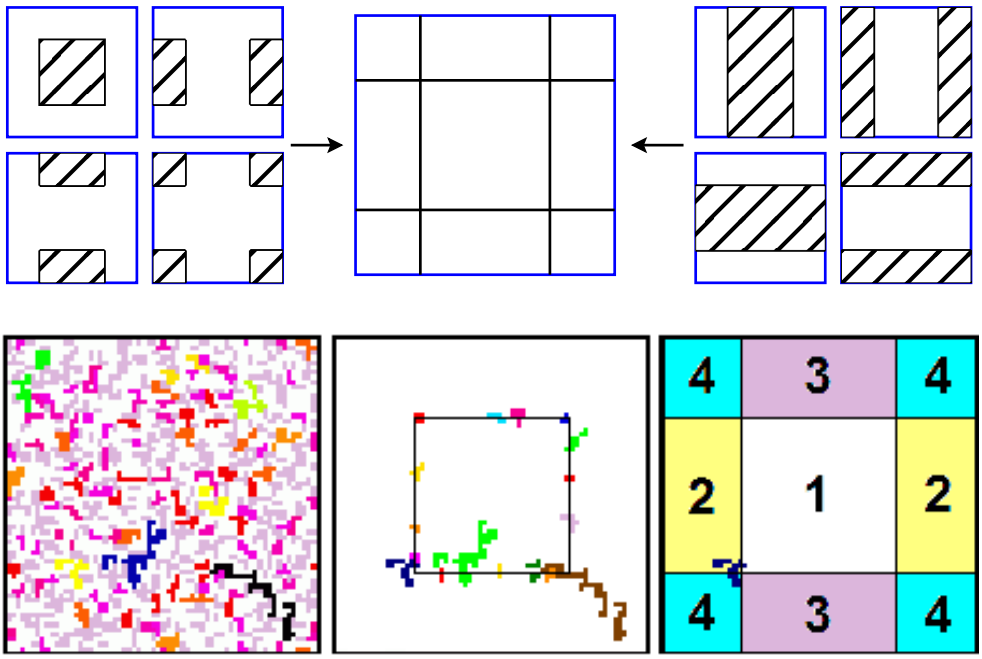

Figure 8.6: Upper panels: 4 neighboring squares with $\ell = L/2$ or two orthogonal stripes with $\ell = L/2$ measure the same boundaries and the same times inside the 2D system. However, there can be a difference coming from the corners. Lower panels: illustration in a critical 64×64 random sample with fixed-h disorder. Renormalized spin clusters (left panel) and those connected clusters, which have a contribution to the entanglement entropy (middle panel). (In the left panel clusters with the same mass are represented by the same color (greyscale), in the middle panel spins in the same cluster are denoted in this way.) Right panel: partition of the sample into four squares, denoted by $1, 2, 3$ and 4 and for four slabs, each being composed of two squares as: $(1, 3); (2, 4); (1, 2)$ and $(3, 4)$. In this sample and with this subdivision there is one 'corner'-cluster, (see at the left-low corner of 1) which contributes to all the four slab subsystems, but does not contribute to all the four square subsystems, see text. Note that periodic boundary conditions are used and the average value of connected and corner clusters in this geometry are measured 18.7 and 0.22, respectively.

For large ℓ the data approach a linear logarithmic dependence, $\delta\mathcal{S}^{(2)}(\ell) \simeq \mathcal{S}^{(2)}_{\rm cr}(\ell) + cst \simeq -b^{(2)} \ln \ell + cst$. We have calculated effective, ℓ-dependent $b^{(2)}$ values from two point fits, which are presented in the inset of Fig.8.5. From their extrapolation we obtain the estimate, $b^{(2)} = -0.029(1)$, for both types of disorder, which is to be compared with $b^{(2)} = -0.019(5)$ by Yu *et al* [27] calculated in a much smaller system with box-h disorder.

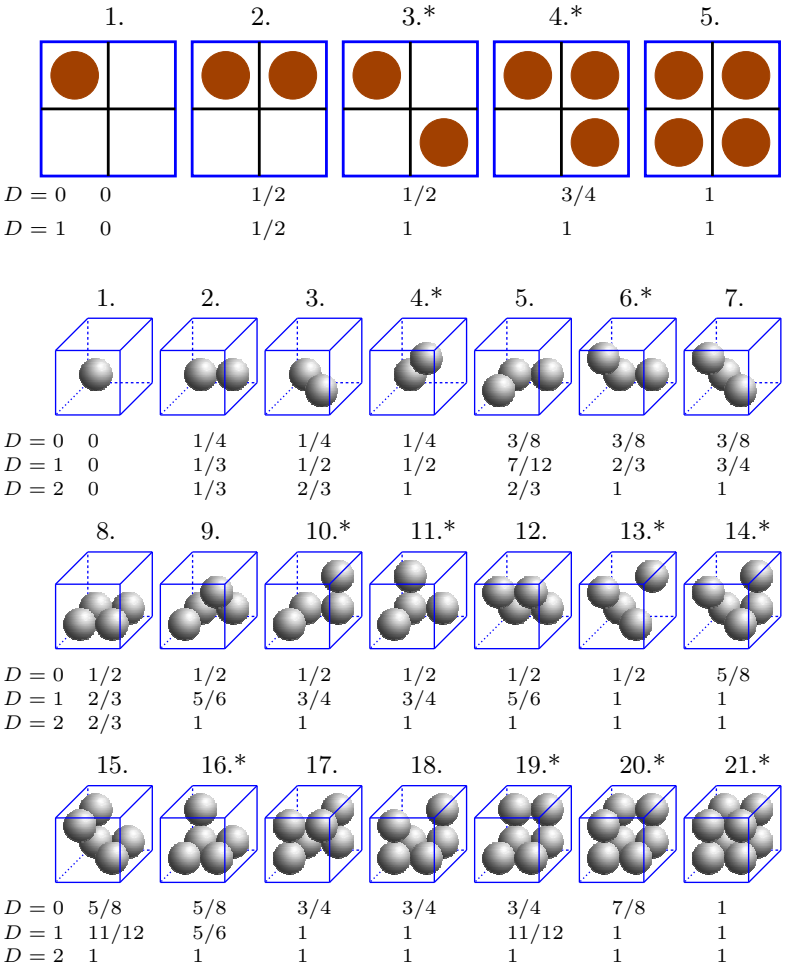

Figure 8.7: Upper panels: Five possible configurations of a cluster over the 4 parts of the system in 2D. The entanglement entropy of the $(D = 0)$ squares or $(D = 1)$ stripes is the sum of the occurrence probability of the different configurations times the corresponding relative weight of the configuration indicated below. As an illustration we list the occurrence probabilities for box-h randomness at $L = 96$ summarized for all clusters: $p_1 = 38.2384$, $p_2 = 1.9162$, $p_3 = 0.0069$, $p_4 = 0.0764$, $p_5 = 0.0292$. There are two configurations marked by asterisks, which give different contributions to the square and stripe subsystems, thus contribute to the entropy of the corners. The central configuration is possible, because the spins of a cluster are generally not connected to each other in the RTIM. Lower panels: The possible cluster configurations and their entropy contributions in 3D. The configurations marked by asterisks, contribute to the corner entropy.

In higher dimensions, $d \geq 3$, the corner contribution represents only a very small fraction of the entanglement entropy and thus its estimate through a direct analysis of Eq. (8.5) contains rather large errors. We can, however, circumvent this problem by considering samples with $\ell = L/2$, when $\mathcal{S}_{\rm cr}^{(d)}(\ell)$ is expressed as appropriate combination of the entropies of subsystems with different shapes for $D = 0, 1, \ldots, d-1$. This calculation is presented in the next section and illustrated in Fig. 8.6 for 2D. Here a given $L \times L$ sample contains four square subsystems and also four slab subsystems. In the two geometries the accumulated boundary between the subsystems and the environment is the same, thus the difference between the accumulated entropies gives the corner contribution: $\mathcal{S}_{\rm cr}^{(2)} = \mathcal{S}_{\rm square}^{(2)} - \mathcal{S}_{\rm slab}^{(2)}$. This contribution is not zero, since

the so called 'corner' clusters at a given partition of the system (see Fig. 8.6) provide different contributions to $\mathcal{S}^{(2)}_{\rm square}$, than to $\mathcal{S}^{(2)}_{\rm slab}$. Furthermore, we show in Fig. 8.7 the contribution of a cluster to the entropy for different shapes (D values) as the function of the configuration of the cluster in both 2D and 3D. The configurations, which give a corner contribution are marked by an asterisk.

The obtained corner contribution to the entanglement entropy at the critical point with $\ell = L/2$ for different values of L are presented in Fig. 8.8 in 2D, 3D and 4D for both disorder distributions. In 2D the variation with $\ln L$ is similar to that obtained by the direct analysis in Fig. 8.5. Also for $d > 2$ asymptotically a logarithmic increase is found

$$\mathcal{S}^{(d)}_{\rm cr}(\ell = L/2) \simeq b^{(d)} \ln \ell + cst \ , \tag{8.6}$$

where the prefactors $b^{(d)}$ are estimated by two-point fits. These are shown in the right panel of Fig.8.8. Their extrapolated values are disorder independent, thus universal, listed in the caption of Fig. 8.8 and in Table 9.1. In 2D this coincides with the value calculated previously in Fig. 8.5.

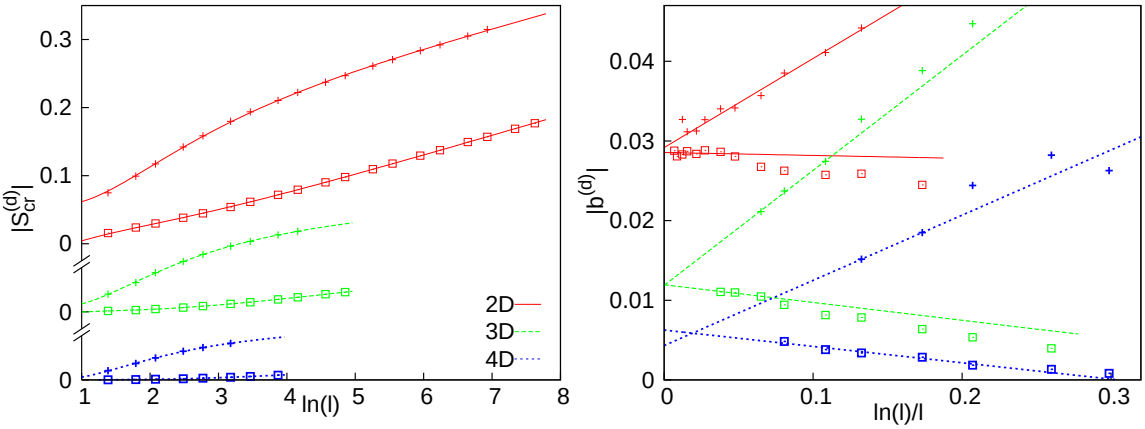

Figure 8.8: Left panel: corner contribution to the entanglement entropy as a function of $\ln \ell$, for $d = 2$, 3 and 4 from up to down for both fixed-h (+) and box-h (⊡) disorders. Note that the position of 0 of the vertical axis is shifted by 0.1 with d. In the right panel the effective prefactors of the logarithm are shown as calculated by two-point fit. The extrapolated values are disorder independent: $b^{(2)} = -0.029(1)$, $b^{(3)} = 0.012(2)$ and $b^{(4)} = -0.006(2)$. The error of data is smaller than the size of the symbols in the left panel and twice of the size of the symbols in the right panel. The lines trough the points are guides to the eye.

The $\ln \ell$ dependence of the corner contribution to the entropy can be understood on the example of two-point clusters. Here we remark that during renormalization spins are glued together to form new effective spin variables and a final spin cluster, which appears in the lower right panel of Fig.8.6 is also the result of the aggregation of two effective spins. As shown in the Appendix, a two-point cluster is a 'corner' cluster in d dimension if the two points are located in two such hypercubes, which are connected by the main diagonal. If the relative coordinates of the two-point cluster are $0 \le x_j \le L/2,\ j = 1, 2, \ldots, d$ (due to periodic boundary conditions) then its accumulated contribution to the corner-entropy — obtained by averaging over all possible positions — is $-2\prod_{j=1}^{d}(-x_j/L)$. The probability of having a

two-site cluster of a length, r, is given by the average pair correlation function, $C_{\rm av}(r) \approx n_r^2$, where $n_r \sim r^{-d}$ is the density of non-decimated sites (when the typical length between existing effective spins is r). The average contribution to the corner-entropy can be estimated as: $\mathcal{S}_{\rm cr}^{(d)}(\ell) \sim -\int_1^\ell {\rm d}x_1 \ldots \int_1^\ell {\rm d}x_d \prod_{j=1}^d (-x_j/r^2) \sim (-1)^{d+1} \int_1^\ell (r^{d-1} r^d)/r^{2d} {\rm d}r \sim (-1)^{d+1} \ln \ell$, which is logarithmically divergent in any dimension, in agreement with the numerical results in Fig. 8.8.

8.3 Results outside the critical point

We have also studied the behavior of the corner-entropy outside the critical point and measured $\mathcal{S}_{\rm cr}^{(d)}(L,\delta)$ as a function of $\delta = \theta - \theta_c$. In the ordered phase, $\delta < 0$, and for $\xi < \ell$ the giant cluster behaves as a so called global cluster, which has 1 contribution to the entropy for all position, orientation and shape of the subsystem. As shown in the Appendix in odd (even) dimensions, after averaging for all positions a global cluster has a contribution 2^{1-d} (0) to the corner entropy. Approaching the critical point for $\xi \gtrsim \ell$ these giant clusters have a finite, but δ-dependent contribution that we omit in the following analysis[1].

In the upper panels of Fig. 8.9 $\mathcal{S}_{\rm cr}^{(d)}(L,\delta)$ is presented as a function of δ for different finite systems for box-h disorder. For any d the corner-entropy is extremal around the critical point and its value outside the critical point is well described with the substitution: $\ell \to \xi$, with $\xi \sim |\delta|^{-\nu}$ being the correlation length. Close to the critical point it satisfies the scaling relation: $-\mathcal{S}_{\rm cr}^{(d)}(L,\delta) + b^{(d)} \ln L = f(\delta L^{1/\nu})$, as illustrated in the lower panels of Fig. 8.9. Here we have used our previous estimates for the correlation length critical exponents $\nu = 1.24,\ 0.98$ and 0.78 in 2D, 3D and 4D from Table 9.1.

8.4 Corner-contribution to the entropy for $\ell = L/2$

Here we show how we determined the corner-contribution to the entropy for a given sample from the entropies measured in different shapes of the subsystems in d dimensions. Inside the hypercubic system we select subsystems of different shapes, which span the system in $D = 0, 1 \ldots, d-1$ directions, but restricted to length $L/2$ in the others as shown in Fig.8.1. The so defined subsystems have hyperfaces of dimension $\Delta = D, D+1, \ldots, d-1$, and the surface of a Δ-dimensional unit is $\varrho_D(\Delta) = L^D 2^{D-\Delta}$, while the number of equivalent hyperface units is given by

$$n_D^{(d)}(\Delta) = 2^{d-\Delta} \binom{d-D}{\Delta - D} . \tag{8.7}$$

[1] We can reformulate this step also in the spirit of the doubling procedure. Analogously to the case of the magnetization and the energy gap, the definition of the entanglement entropy must be adjusted outside the critical point according to our replica approach, in order to decrease the possibly strong finite-size corrections emerging in the SDRG method. In a replicated system, having N replicas, the correlation cluster gives only $1/N$ contribution to the averaged entanglement entropy, thus in the limit of $N \to \infty$ — which we wish to simulate in our calculations — it should be neglected.

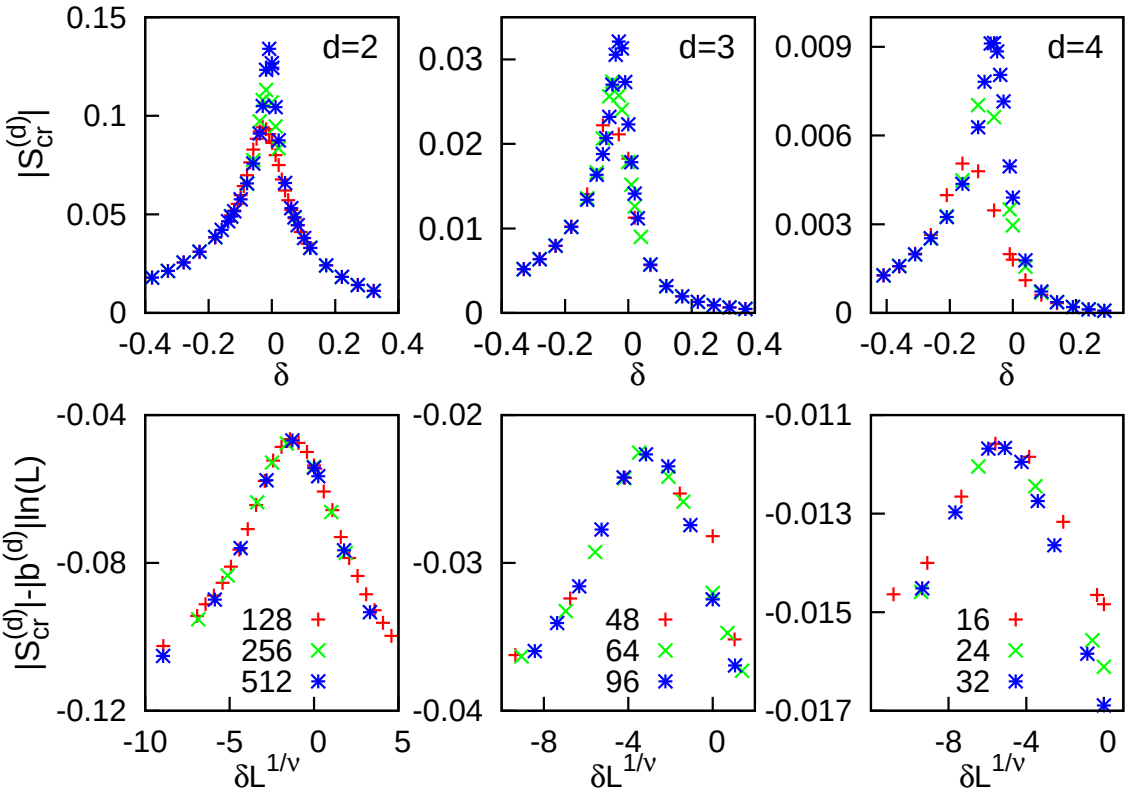

Figure 8.9: Upper panels: entropy contribution of the corners $\mathcal{S}_{\rm cr}^{(d)}(L,\delta)$ in $d=2,3$ and 4 for different system sizes as the function of the control parameter for box-h disorder. In the lower panels scaling collapse of the central part of $\mathcal{S}_{\rm cr}^{(d)}(L,\delta)$ is shown, see text.

We measure the entanglement entropy in this system, $\mathcal{S}_D^{(d)}$, for all different D, averaged over the L^{d-D} possible positions and over the $\binom{d}{D}$ orientations of the subsystem. The entanglement entropy is written as the sum of the contributions of the different dimensional hyperfaces:

$$\mathcal{S}_D^{(d)} = \sum_{\Delta=D}^{d-1} \mathcal{S}_D^{(d)}(\Delta)\ , \tag{8.8}$$

which is to be compared with $\mathcal{S}_0^{(d)} \equiv \mathcal{S}_{\rm cube}^{(d)}$ in Eq. (8.5). First we note that

$$\frac{\mathcal{S}_D^{(d)}(\Delta)}{\mathcal{S}_0^{(d)}(\Delta)} = \frac{\varrho_D(\Delta) n_D^{(d)}(\Delta)}{\varrho_0(\Delta) n_0^{(d)}(\Delta)} = 2^D \frac{\binom{d-D}{\Delta-D}}{\binom{d}{\Delta}}\ , \tag{8.9}$$

where $\varrho_D(\Delta) n_D^{(d)}(\Delta)$ and $\varrho_0(\Delta) n_0^{(d)}(\Delta)$ are the total areas of the given hyperface measured in the two shapes. In this way we obtain:

$$\mathcal{S}_D^{(d)} = \sum_{\Delta=D}^{d-1} 2^D \frac{\binom{d-D}{\Delta-D}}{\binom{d}{\Delta}} \mathcal{S}_0^{(d)}(\Delta)\ . \tag{8.10}$$

It is straightforward to check that this expression can be inverted to obtain the entropy contribution in the cube geometry:

$$\mathcal{S}_0^{(d)}(\Delta) = \sum_{D=\Delta}^{d-1} \frac{(-1)^{D-\Delta}}{2^D} \binom{d}{D} \binom{D}{\Delta} \mathcal{S}_D^{(d)} \ . \tag{8.11}$$

As a special case for $\mathcal{S}_0^{(d)}(0) \equiv \mathcal{S}_{\rm cr}^{(d)}$ we obtain for the corner contribution:

$$\mathcal{S}_0^{(d)}(0) = \sum_{D=0}^{d-1} \left(-\frac{1}{2}\right)^D \binom{d}{D} \mathcal{S}_D^{(d)} \ . \tag{8.12}$$

As an application, we calculate the contribution of a global cluster to $\mathcal{S}_0^{(d)}(0)$. A cluster is global by our definition, if its entropy contribution is 1 for all positions, orientations and shapes (D) of the subsystems, thus

$$\begin{gathered} \mathcal{S}_0^{(d)}(0)_{(\rm global)} = \textstyle\sum_{D=0}^{d-1}(-2)^{-D}\binom{d}{D} = \\ \frac{1-(-1)^d}{2^d} = \begin{cases} 0, & \text{even } d \\ 2^{1-d}, & \text{odd } d \end{cases} \end{gathered} \tag{8.13}$$

8.5 Discussion

First, we studied the scaling behavior of the entanglement entropy in the ladder geometry. For a fixed width, w, the entropy is found to grow logarithmically with the length of the block, ℓ, and the prefactor is found independent of w. On the other hand the ℓ independent term of the entropy is found to have a linear w dependence, at least for large enough w, which forecasts are law behavior in 2D.

We have also studied the entanglement entropy of the RTIM in 2D, 3D and 4D with our improved SDRG algorithm. Since the critical properties of the RTIM are governed by IDFP-s, at which the SDRG becomes asymptotically exact, also our results about the singularities of the entropy tend to be exact for large scales. We expect that our finite-size results are already in the asymptotic regime, which is supported by the fact that the singularity parameters obtained are disorder independent. We have demonstrated that the area law is satisfied for $d \geq 2$ and there is a singular correction to it in the form of $b^{(d)} \ln \ell$. This correction is shown to be attributed to corners, related to the diverging correlation length and universal, i.e. disorder independent.

Chapter 9

Conclusions

In this thesis we studied the critical behavior of the random transverse-field Ising model in higher dimensional systems. Detailed theoretical results about the RTIM are known in one dimension due to a complete analytical solution of the strong disorder renormalization group treatment [20, 21]. The SDRG results are asymptotically exact in the vicinity of the critical point and also in the Griffiths-phases, as long as dynamical singularities are concerned [181]. One important observation that the critical properties of the 1D model are governed by an infinite disorder fixed point, in which the strength of disorder grows without limit during renormalization [20–22] and thus becomes dominant over quantum fluctuations. At an IDFP the system shows extremely heterogeneous behavior, which manifests itself in all aspects of the observed physics. As a consequence, the physical quantities have a broad distribution, where the typical and average values are very different and generally show different type of singularities while increasing the system size. Moreover, the dynamics becomes extremely slow, characterized by a formally infinitely large z dynamical exponent. Contrary to the $t \sim L^z$ usual scaling of the characteristic t time scale with the L system size, at an IDFP the system obeys the following scaling form $\ln t \sim L^\psi$, with $\psi = 0.5$ in 1D.

In higher dimensions, in particular in two dimensions the calculations are numerical and have only limited accuracy [23–28], having a running time $\sim N^3$ for a system containing N sites. In order to address this problem, we developed a very efficient numerical algorithm of the strong disorder renormalization group method. Having at hand this improved algorithm we can renormalize an N-site system within a time $N \log N$, independently of the topology of the system and we went up to $N \sim 4 \times 10^6$ with a typical number of 4×10^4 realizations. The improved algorithm is based on our observation that the routinely applied maximum rule enables the significant simplification of the SDRG algorithm, while yielding exactly the same results as before. We also extended our improved SDRG algorithm for disordered quantum Potts models and for the disordered quantum rotor model. Remarkably, we have also found a very efficient, novel algorithm for the one-dimensional problem, where the maximum rule does not play any role.

Besides the fact that the RTIM has experimental realizations it also controls the critical behavior of the quantum spin-glass transition, as well as that of a class of random quantum systems having an order parameter with discrete symmetry, such as random quantum Potts

[237] and clock models [238]. Nonequilibrium phase transitions, such as the contact process with (strong) disorder also belong to this universality class.

Comparing with earlier SDRG investigations in 2D, our study had several different features.

- We defined and calculated finite-size pseudo-critical points with the extension of the doubling method for the higher dimensional case.
- By studying the distribution of the pseudo-critical points, we obtained accurate estimates for the true critical point of the model.
- We calculated effective, size-dependent critical exponents and studied their extrapolation for $L \to \infty$.
- We considered different forms of disorder and studied the universality of the critical exponents as well as the scaling functions.
- As the first systematic study, we analyzed the magnetic scaling behavior outside the critical point, as well as dynamical scaling in the disordered and ordered Griffiths-phases.

We have studied regular lattices with dimension $d \leq 4$ as well as Erdős-Rényi random graphs, which are infinite dimensional objects. For different types of (ferromagnetic) disorder the infinite disorder fixed point is shown to be characterized by the same set of critical exponents, for which we have obtained improved estimates in 2D and the first quantitative estimates in even higher dimensions.

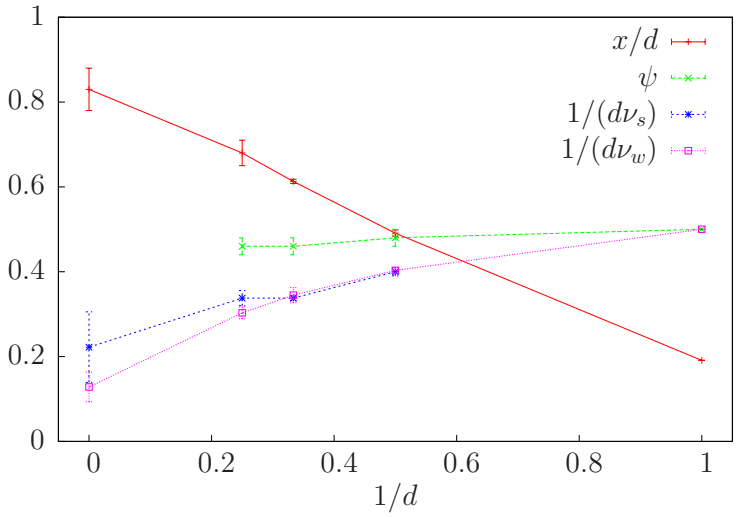

Figure 9.1: Critical exponents of the random transverse-field Ising model as a function of $1/d$. At $1/d = 0$ there are results of the Erdős-Rényi random graph.

Our numerical SDRG results indicate that the critical behavior of the random transverse-field Ising model in 1, 2, 3 and 4 dimensions as well as in the Erdős-Rényi random graph is controlled by infinite disorder fixed points. This fact justifies the use of the SDRG method and ensures that the calculated numerical results about the critical exponents tend to be asymptotically correct for large sizes. The critical exponents, obtained so far, are summarized in Table 9.1 for

Table 9.1: Critical properties of the RTIM for finite dimensional lattices and for Erdős-Rényi random graphs. N_{max} denotes the number of spins in the largest finite systems used in the RG calculation. In the last four lines by estimating the different critical exponents results obtained by both forms of applied disorder are taken into account. For Erdős-Rényi graphs the following analogies are used: $d\nu = \omega$, while $x/d \equiv 1 - d_f/d = 1 - \vartheta$ and $\beta \equiv \nu x = \omega(1-\vartheta)$. Note that the $\omega = 1.3(2)$ exponent characterizing the dynamics for Erdős-Rényi graphs is not in direct analogy with ψ. The notation b indicates the prefactor of the $\ln \ell$ universal logarithmic corner contribution to the entanglement entropy for hypercubic subsystems, as obtained in Chapter 8.

	1D	2D	3D	4D	E.-R. graphs
N_{max}	(exact)	$2048^2 \approx 4.2 \times 10^6$	$128^3 \approx 2.1 \times 10^6$	$48^4 \approx 5.3 \times 10^6$	$2^{22} \approx 4.2 \times 10^6$
$\theta_c^{(b)}$	0	1.6784(1)	2.5305(10)	3.110(5)	2.775(2)
$\theta_c^{(f)}$	-1	$-0.17034(2)$	$-0.07627(2)$	$-0.04698(10)$	$-0.093(1)$
$d\nu_w$	2	2.48(4)	2.90(15)	3.30(15)	7.8(20)
$d\nu_s$	(no shift)	2.50(6)	2.96(5)	2.96(15)	4.5(15)
x/d	$\frac{3-\sqrt{5}}{4} \approx 0.191$	0.491(8)	0.613(5)	0.68(3)	0.83(5)
ψ	0.5	0.48(2)	0.46(2)	0.46(2)	–
b	$1/6 \approx 0.1667$	$-0.029(1)$	0.012(2)	$-0.006(2)$	–

lattices and Erdős-Rényi graphs. The exponents show a smooth variation with the dimension, which is illustrated in Fig. 9.1, which indicates that the large-d limit of the problem is not singular. Consequently, infinite disorder scaling is expected to be valid at any dimension.

We have also studied the entanglement entropy of the RTIM for ladders, as well as for 2D, 3D and 4D lattices. We have demonstrated that the area law is satisfied for $d \geq 2$ and there is a singular correction to it in the form of $b^{(d)} \ln \ell$. This correction is shown to be attributed to corners, related to the diverging correlation length and universal, i.e. independent from the type of the disorder. On the example of two-point clusters we have also derived the logarithmic form of this correction, as well, as its alternating sign with d. Since in the SDRG method all clusters are formed as effective two-point clusters, our results are expected to hold generally. Here we note that very recently, also a possible method for the experimental measurement of the entanglement entropy was proposed [239], applicable for a generic quantum many-body system by using a quantum switch.

Our investigations can be extended and generalized to several directions. First we mention that the extremal behavior of the corner entropy at the critical point makes a possibility to detect and define sample dependent critical points via the entanglement entropy, a concept which has already been applied in 1D [212]. It is of interest to study the possible singularities of the entropy per area and the edge contributions per surface as a function of δ around the critical point for $d \geq 2$. One can also study the entanglement properties of diluted transverse-field Ising models for $d \geq 2$ having critical properties related to classical percolation [240]. An other interesting problem is to study the dependence of the corner contribution on the number of corners, the subsystem has, e.g. on triangular lattices. We expect that the b prefactor of the logarithm vanishes for an asymptotically spherical subsystem for the RTIM.

An other interesting question concerns dynamical aspects of the entanglement entropy after

a sudden change of the parameters in the Hamiltonian at time $t = 0$. This question has been recently studied in 1D [241] and an ultraslow increase of the entropy is found: $\mathcal{S}(t) \sim \ln \ln t$, if the quench is performed to the critical point of the system. For $d \geq 2$ one expects a similar time-dependence of the corner-contribution: $\mathcal{S}_{\rm cr}^{(d)}(t) \sim \ln \ln t$.

A natural way to extend our work regarding the critical exponents concerns surface critical behavior, especially the surface magnetization studied recently in [242] with a non-linear transfer approach even in higher dimensions. In 1D the surface critical exponent is exactly known (for a review see [14]). A related question is the form of the magnetization profile with different boundary conditions in higher dimensions, as studied numerically in 1D recently [99, 243].

Very recently, also a completely independent approximate approach led to the prediction that the critical point of the RTIM is governed by an IDFP also in higher dimensions [244]. Another recent study concerns the SDRG method over various fractals showing clear evidences of IDFP behavior [245]. Probably the most recent study in [246] concerns also the 2D RTIM in a planar approximation for up to $L = 500$ and 400 realizations, leading to estimates which are consistent with our findings for $L = 2048$ and 40000 realizations in 2010 [39].

In our studies, we applied the Erdős-Rényi random graphs as the realization of the infinite dimensional lattice. We note, however, that there are many other interesting networks, among those there are several characterized by a formally infinitely large dimension. An interesting example is the case of generalized small-world networks with tunable dimension [247], where we carried out a similar analysis and have not found IDFP behavior above dimension ≈ 3. To understand the behavior of large dimensional networks is one of the most interesting open problems in this field.

At this point we want to mention another recent study by Dimitrova and Mézard [248] on the critical behavior of the RTIM with the cavity method [249, 250]. In 1D even the simple mean-field cavity method is shown to recover some of the exact results, such as infinite disorder scaling at the critical point. On the contrary, results on the Bethe lattice indicate the presence of a conventional random fixed point with a finite dynamical exponent. This result is probably due to the fact that the local topology of the Bethe lattice is different from that of the hypercubic lattices. The local topology has already been found to have an important effect on the critical behavior of random quantum systems [251]. For example in the Bethe lattice it seems to be impossible to define an isotropic and quasi-one-dimensional cluster, which could be relevant for the low-energy excitations and thus for infinite disorder scaling. A direct SDRG study of RTIM on a Bethe lattice could clarify some of the open questions.

Appendix A

The cluster counting problem

Although we can directly measure $\mathcal{S}_D^{(d)}$ in d dimensions by a simple cluster counting algorithm, it is generally a more time consuming process, than the underlying SDRG method, which needs only $\mathcal{O}(N \log N)$ time in any dimensions. With subsystems spanning the system in D directions, the corresponding D coordinates of the spins are irrelevant. Having the coordinates of the sites in a cluster, the first step is the projection of these coordinates to the relevant $d-D$ directions, after which we analyze the $d-D$ dimensional problem of a hypercubic subsystem. Thus for each orientation of the subsystem the problem is technically equivalent to the case of calculating $\mathcal{S}_0^{(d-D)}$. Although the entropy can be measured for each position in asymptotically ℓ^{d-D-1} time, this should be done for each subsystem size and L^{d-D} position of the subsystem yielding a running time of $\mathcal{O}(L^{2(d-D)}) = \mathcal{O}(N^{2(1-D/d)})$. In the following we show, how the problem can be solved in some cases analytically and treated effectively numerically in the other cases. In all cases the von Neumann entropy is calculated as the sum of the entropies of individual clusters.

A.1 Quasi-1D case of $\mathcal{S}_{d-1}^{(d)}$

In this case the entanglement entropy can be written in a simple closed form as the function of the cluster structure. Here we present only our result, which can be derived by a direct geometrical analysis, or also as a special case of our general formula presented later. It turned out that the entropy can be calculated from the size-distribution of the holes inside the clusters. First, we measure the h sizes of the holes as relative coordinates between consecutive points inside a cluster, and transform it to $h = \min(H, L-H)$. This later step is the consequence of the periodic boundary conditions, ensuring that $\mathcal{S}_{d-1}^{(d)}(\ell) = \mathcal{S}_{d-1}^{(d)}(L-\ell)$. Now we build up a statistics about the h values in all clusters in all realizations: $n(j)$ = number of distances with: $h = j$. The space-averaged entanglement entropy for $\ell \leq L/2$ is given by:

$$\mathcal{S}_{d-1}^{(d)}(\ell) = \frac{1}{L} \sum_{i=1}^{\ell} N(i) \,, \tag{A.1}$$

where $1/L$ corresponds to the average over the subsystems position, and $N(i)$ is given by the cumulative statistics:

$$N(i) = \sum_{i=j}^{L/2} n(j). \tag{A.2}$$

A similar expression to (A.1) holds also for the general case of $\mathcal{S}_D^{(d)}$ with a space averaging factor of $1/L^{d-D}$ and an $N(i)$ function corresponding to the finite derivative of the entropy, see (A.6). The difficulty lies in the expression of $N(i)$, which gets exponentially complicated, in the general case, as the size of the cluster grows. In the case of $\mathcal{S}_{d-1}^{(d)}$ we already have a significant gain in the running time, having a performance of $\mathcal{O}(L)$ instead of the $\mathcal{O}(L^2)$ time complexity of the cluster counting approach.

A.2 Quasi-2D case of $\mathcal{S}_{d-2}^{(d)}$

The entropy of the simplest nontrivial case of a cluster having $k = 2$ points can be straightforwardly derived by a direct, but tedious geometrical analysis, or it can be equivalently obtained from our general formula, as given in the next section. According to our results, the space-averaged entropy-contribution of a 2-point cluster is

$$S_{d-2,(2\mathrm{p})}^{(d)}(\ell) = \frac{1}{L^2} \sum_{i=1}^{\ell} N(i), \tag{A.3}$$

where $N(i)$ is expressed with the $0 \le y \le x \le L/2$ relative coordinates of the cluster points (in the relevant 2 directions) as:

$$N(i) = 2 \begin{cases} 2i - 1, & 1 \le i \le x \\ x + y, & x < i \le L - x \\ L - 2i + 2y + 1, & L - x < i \le L - y \\ 4L - 6i + 3, & L - y < i \le L \end{cases} \tag{A.4}$$

If the ground state of our system consists only two-point clusters (e.g. singlets), then we only need to make a statistics about the form of the clusters and apply these expressions. However, in the quantum Ising model the ground state also consists clusters having $k > 2$ points, the probability of which decreases at the critical point as $k^{-(1+d/d_f)}$ for large k, where d_f denotes the fractal dimension of the ground state (for numerical values see Table 9.1).

For a cluster with k points $N_k(i)$ has a much more complicated form. However, even in the general case, $N_k(i)$ has a similar constant part:

$$N_k(i) = \ 2(h_1 + h_2), \quad h_> < i \le L - h_>, \tag{A.5}$$

where the cluster can be minimally involved into a rectangle of size $(h_1+1)\times(h_2+1)$ and $h_<$ ($h_>$) denotes the smaller (larger) h value. In practice we used Eq. (A.5) for $h_> < i \le L - h_>$, and the methods presented in the next section otherwise. This way our implementation achieved

typically an $\mathcal{O}(L^2 \log L)$ running time for the available system sizes at the critical point instead of the $\mathcal{O}(L^4)$ performance of the naïve algorithm.

A.3 General case of $\mathcal{S}_D^{(d)}$

In the general case we have two possibilities, either calculating the entropy contribution of each cluster numerically or using an analytical expression, whose complexity grows exponentially with the clusters size. In practice, for clusters containing less, than 8 points, we applied analytical expressions in all dimensions, while for larger clusters we used a combined analytical-numerical algorithm, discussed below.

The entropy comes from the clusters shared by the subsystem and the rest of the system. Thus, the entropy of a given cluster is given by the normalized number of positions in which the subsystem contains at least one site of the cluster, minus the normalized number of positions in which the subsystem contains the whole cluster. If a given position of the subsystem contains some part of the cluster (or the whole cluster) for ℓ_0, it preserves this property also for larger sizes $\ell > \ell_0$. Thus it is sufficient to study the number of new positions at a given ℓ subsystem size, which contain some part of the cluster $P(\ell)$ or the total cluster $T(\ell)$. With these quantities the space-averaged entropy of a cluster is given by

$$S_D^{(d)}(\ell) = \frac{1}{L^{d-D}} \sum_{i=1}^{\ell} N(i) \ , \tag{A.6}$$

where

$$N(i) = P(i) - T(i) \ . \tag{A.7}$$

$P(i)$ can be determined numerically by a label spreading process starting from the k sites of the cluster. As the position of a subsystem, we use the position of its 'upper corner' (considering all $d - D$ directions). For $\ell = 1$ the subsystem contains only one site, thus $P(1) = k$, and we assign a label of 1 to the points of the cluster. Generally $P(i)$ is given by the number of sites with label i. If we already determined the sites with label i, all such non-labelled neighbors of these sites, which lie in upper or the same positions in all directions will get the label $i+1$. We follow this process until all sites are labeled in the system.

$T(i)$ is given by the number of positions, at which the subsystem contains the whole cluster. If such a site is known already, the same label spreading process can be applied as in the case of $P(i)$. However, $T(i)$ can be also determined explicitly based on the structure of the cluster, more precisely on the structure of the holes inside the cluster. If the subsystem at a given position contains the whole cluster, then the rest of the system is everywhere empty, corresponding to a hole in each directions. In order to locate these empty regions, we build up a statistics about the relative coordinates of the points of the cluster in each $d - D$ directions. These relative coordinates are the linear sizes of the holes in the cluster in each direction. From these one-dimensional values we combine the $d - D$ dimensional holes in the cluster, the multiplicity of which is given by the product of the number of the chosen one-dimensional holes.

For example, in quasi-2D ($d - D = 2$) all holes in the x-direction are combined with all holes in the y-direction yielding the shape and multiplicity of the two-dimensional holes.

Having a hole with linear extents of $h_1 \geq h_2 \geq \cdots \geq h_{d-D}$, its contribution is $t(i) = 0$ for $i \leq L - h_{d-D}$, while $t(i) \geq 0$ for $i > L - h_{d-D}$, given by

$$t(i) = \prod_{j=1}^{d-D}(h_j - L + i) - \prod_{j=1}^{d-D}(h_j - L + i - 1) \; . \tag{A.8}$$

The total $T(i)$ function is the sum of the $t(i)$ functions of the holes in the cluster. Based on this result, we can write down an explicit expression also for $P(i)$. By considering the independent label spreading processes from each site of the cluster, yielding

$$C(i) = k(i^{d-D} - (i-1)^{d-D}), \tag{A.9}$$

we count m-times the number of positions containing $m > 1$ sites, instead of counting only once each position. This can be compensated as follows

$$P(i) = C(i) - \sum_{m=2}^{k}(-1)^m T_m(i) \; , \tag{A.10}$$

where $T_m(i)$ stands for the contributions of the holes summarized for all $\binom{k}{m}$ possible m-point subsets of the cluster. For $m = k$, $T_k(i) = T(i)$ corresponding to the case, in which the subsystem contains the whole cluster.

As an application, we derive the result shown in (A.4) for a 2-point cluster in quasi-2D systems with relative coordinates $y \leq x \leq L/2$.

$$N(i) = 2(2i - 1) - 2T(i) \; . \tag{A.11}$$

There are 4 holes in the system, with extensions (h_1, h_2), such that $h_1 \geq h_2$, namely (x, y), $(L - x, y)$, $(L - y, x)$ and $(L - y, L - x)$, giving

$$\begin{aligned}
t^{(x,y)}(i) &= 2i - 1 + x + y - 2L \qquad i > L - y \\
t^{(L-x,y)}(i) &= 2i - 1 - x + y - L \qquad i > L - y \\
t^{(L-y,x)}(i) &= 2i - 1 + x - y - L \qquad i > L - x \\
t^{(L-y,L-x)}(i) &= 2i - 1 - x - y \qquad i > x \; .
\end{aligned}$$

With $T(i) = t^{(x,y)}(i) + t^{(L-x,y)}(i) + t^{(L-y,x)}(i) + t^{(L-y,L-x)}(i)$ we get (A.4).

A.4 Entropy of 2-point clusters

First we derive the entropy contribution of the corners at $\ell = L/2$ in a system containing only 2-point clusters in $d = 2$. For a cluster with $0 \leq y \leq x \leq L/2$ relative coordinates, (A.1) and

(A.2) gives the following simple result $\mathcal{S}_1^{(2)} = (x+y)/L$, while form (A.3) and (A.4) we obtain $\mathcal{S}_0^{(2)} = (x+y)/L - 2xyL^{-2}$. According to (8.12), the entropy contribution of the corners at $\ell = L/2$ is given by the difference of these expressions, yielding

$$\mathcal{S}_0^{(2)}(0) = -\frac{2xy}{L^2} \,. \tag{A.12}$$

This result can be directly obtained form the observation that for a 2-point cluster only the 3. configuration in the upper panel of Fig. 8.7 gives contribution to the entropy of the corners. In $d = 3$ for a cluster with $0 \le z \le y \le x \le L/2$ relative coordinates, $\mathcal{S}_2^{(3)} = (x+y+z)/(2L)$, $\mathcal{S}_1^{(3)} = (x+y+z)/(2L) - 2(xy+yz+xz)L^{-2}$, while $\mathcal{S}_0^{(3)} = 2xyzL^{-3} + (x+y+z)/(2L) - (xy+yz+xz)L^{-2}$. According to (8.12), the entropy contribution of the corners at $\ell = L/2$ is given by

$$\mathcal{S}_0^{(3)}(0) = \frac{2xyz}{L^3} \,. \tag{A.13}$$

The result can be obtained directly, because only the 4. configuration in the lower panel of Fig. 8.7 contributes to the corners in this case. A similar expression holds for a 2-point cluster in d dimensions, with $0 \le x_j \le L/2$ relative coordinates

$$\mathcal{S}_0^{(d)}(0) = \frac{2(-1)^{d+1}}{L^d} \prod_{j=1}^{d} x_j \,. \tag{A.14}$$

In order to calculate the entropy contribution of the 2-point clusters to the corners, we need to know the occurrence probability of the clusters with a given distance between its points. This is given by the average pair correlation function $C_{\rm av}(r)$. At a distance r, $C_{\rm av}(r)$ is dominated by the spins not have been decimated out until this length scale. The number of such spins is $n_r \sim r^{-d}$ at the critical point, thus for two spins their occurrence probability is given by $\sim r^{-2d}$. We saw that at $\ell = L/2$ the entropy of the subsystem is already in the asymptotic regime, thus the result is practically the same for the subsystems having the same size in a larger system. Thus, for any $\ell \ll L$,

$$\mathcal{S}_{\rm cr}^{(d)}(\ell) \sim (-1)^{d+1} \sum_{x_1=1}^{\ell} \cdots \sum_{x_d=1}^{\ell} \frac{\prod_{j=1}^{d} x_j}{r^{2d}} \,, \tag{A.15}$$

in which summations can be approximated for $1 \ll \ell$ by integrals, yielding

$$\mathcal{S}_{\rm cr}^{(d)}(\ell) \sim (-1)^{d+1} \int_{r=1}^{\ell} \frac{r^{d-1} r^d}{r^{2d}} {\rm d}r \sim (-1)^{d+1} \log \ell \,. \tag{A.16}$$

Outside the critical point, the ξ correlation length is finite and the $n_r \sim r^{-d}$ scaling is only valid until $r \approx \xi$. Thus $\mathcal{S}_{\rm cr}^{(d)}(\ell) \sim \log\left(\max\left(\ell, \xi\right)\right)$ goes to a constant value outside the critical point, while shows a logarithmic singularity at the critical point. For clusters having more, than two points, similar qualitative behavior is expected, although the technical details are much more complicated. The physical picture behind the same behavior is given by the SDRG procedure. During the calculation, effective clusters are formed by merging together two (effective) spins,

which have not been decimated yet. Around a given length scale, the structure of the ground state is given by single effective spins and two-spin clusters formed around this length scale. Thus, each multispin cluster with an extension L_c corresponds to a two-point cluster, built up from dressed, effective spins having an inner structure only on a lower $l_c \ll L_c$ length scale.

Bibliography

[1] L. Onsager. Crystal statistics. I. a two-dimensional model with an order-disorder transition. *Physical Review*, 65(3-4):117–149, 1944.

[2] R. Mélin and F. Iglói. Strongly disordered Hubbard model in one dimension: Spin and orbital infinite randomness and Griffiths phases. *Phys. Rev. B*, 74(15):155104, 2006.

[3] E. C. Andrade, E. Miranda, and V. Dobrosavljevic. Electronic Griffiths phase of the $d = 2$ Mott transition. *Phys. Rev. Lett.*, 102(20):206403, 2009.

[4] P. Le Doussal, C. Monthus, and D. S. Fisher. Random walkers in one-dimensional random environments: Exact renormalization group analysis. *Phys. Rev. E*, 59(5):4795–4840, 1999.

[5] T. Garel, D. A. Huse, S. Leibler, and H. Orland. Localization transition of random chains at interfaces. *Europhys. Lett.*, 8(1):9–13, 1989.

[6] R. Juhász, L. Santen, and F. Iglói. Partially asymmetric exclusion models with quenched disorder. *Phys. Rev. Lett.*, 94(1):4, 2005.

[7] R. Juhász, L. Santen, and F. Iglói. Partially asymmetric zero-range process with quenched disorder. *Phys. Rev. E*, 72(4):12, 2005.

[8] R. Juhász, L. Santen, and F. Iglói. Partially asymmetric exclusion processes with sitewise disorder. *Phys. Rev. E*, 74(6):10, 2006.

[9] C. Monthus. Anomalous diffusion, localization, aging, and subaging effects in trap models at very low temperature. *Phys. Rev. E*, 68(3):036114, 2003.

[10] C. Monthus. Localization properties of the anomalous diffusion phase in the directed trap model and in the Sinai diffusion with a bias. *Phys. Rev. E*, 67(4):046109, 2003.

[11] J. Hooyberghs, F. Iglói, and C. Vanderzande. Strong disorder fixed point in absorbing-state phase transitions. *Phys. Rev. Lett.*, 90(10), 2003.

[12] J. Hooyberghs, F. Iglói, and C. Vanderzande. Absorbing state phase transitions with quenched disorder. *Phys. Rev. E*, 69(6), 2004.

[13] Y. Imry and S.-k. Ma. Random-field instability of the ordered state of continuous symmetry. *Phys. Rev. Lett.*, 35(21):1399–1401, 1975.

[14] F. Iglói and C. Monthus. Strong disorder RG approach of random systems. *Physics Reports*, 412(5-6):277–431, 2005.

[15] B. M. McCoy. Theory of a two-dimensional Ising model with random impurities. III. boundary effects. *Physical Review*, 188(2):1014–1031, 1969.

[16] B. M. McCoy. Theory of a two-dimensional Ising model with random impurities. IV. generalizations. *Phys. Rev. B*, 2(7):2795–2803, 1970.

[17] B. M. McCoy and T. T. Wu. Theory of a two-dimensional Ising model with random impurities. I. thermodynamics. *Physical Review*, 176(2):631–643, 1968.

[18] B. M. McCoy and T. T. Wu. Theory of a two-dimensional Ising model with random impurities. II. spin correlation functions. *Physical Review*, 188(2):982–1013, 1969.

[19] R. Shankar and G. Murthy. Nearest-neighbor frustrated random-bond model in D=2 - some exact results. *Phys. Rev. B*, 36(1):536–545, 1987.

[20] D. S. Fisher. Random transverse field Ising spin chains. *Phys. Rev. Lett.*, 69(3):534–537, 1992.

[21] D. S. Fisher. Critical-behavior of random transverse-field Ising spin chains. *Phys. Rev. B*, 51(10):6411–6461, 1995.

[22] D. S. Fisher. Phase transitions and singularities in random quantum systems. *Physica A*, 263(1-4):222–233, 1999.

[23] D. Karevski, Y. Lin, H. Rieger, N. Kawashima, and F. Iglói. Random quantum magnets with broad disorder distribution. *Eur. Phys. J. B*, 20(2):267–276, 2001.

[24] Y.-C. Lin, F. Iglói, and H. Rieger. Entanglement entropy at infinite-randomness fixed points in higher dimensions. *Phys. Rev. Lett.*, 99(14), 2007.

[25] Y.-C. Lin, N. Kawashima, F. Iglói, and H. Rieger. Numerical renormalization group study of random transverse Ising models in one and two space dimensions. *Progress of Theoretical Physics Supplement*, 138:479–488, 2000.

[26] O. Motrunich, S. Mau, D. Huse, and D. Fisher. Infinite-randomness quantum Ising critical fixed points. *Phys. Rev. B*, 61(2):1160–1172, 2000.

[27] R. Yu, H. Saleur, and S. Haas. Entanglement entropy in the two-dimensional random transverse field Ising model. *Phys. Rev. B*, 77(14), 2008.

[28] C. Pich, A. Young, H. Rieger, and N. Kawashima. Critical behavior and Griffiths-McCoy singularities in the two-dimensional random quantum Ising ferromagnet. *Phys. Rev. Lett.*, 81(26):5916–5919, 1998.

[29] T. Vojta, A. Farquhar, and J. Mast. Infinite-randomness critical point in the two-dimensional disordered contact process. *Phys. Rev. E*, 79(1), 2009.

[30] L. Amico, R. Fazio, A. Osterloh, and V. Vedral. Entanglement in many-body systems. *Rev. Mod. Phys.*, 80(2):517–576, 2008.

[31] P. Calabrese and J. Cardy. Entanglement entropy and quantum field theory. *J. Stat. Mech.*, 2004.

[32] C. Holzhey, F. Larsen, and F. Wilczek. Geometric and renormalized entropy in conformal field-theory. *Nucl. Phys. B*, 424(3):443–467, 1994.

[33] G. Vidal, J. I. Latorre, E. Rico, and A. Kitaev. Entanglement in quantum critical phenomena. *Phys. Rev. Lett.*, 90(22), 2003.

[34] G. Refael and J. Moore. Entanglement entropy of random quantum critical points in one dimension. *Phys. Rev. Lett.*, 93(26), 2004.

[35] E. Carlon, P. Lajkó, and F. Iglói. Disorder induced cross-over effects at quantum critical points. *Phys. Rev. Lett.*, 87(27):4, 2001.

[36] T. Senthil and S. N. Majumdar. Critical properties of random quantum potts and clock models. *Phys. Rev. Lett.*, 76(16):3001–3004, 1996.

[37] T. E. Harris. Contact interactions on a lattice. *The Annals of Probability*, 2(6):969–988, 1974.

[38] I. A. Kovács and F. Iglói. Critical behavior and entanglement of the random transverse-field Ising model between one and two dimensions. *Phys. Rev. B*, 80(21), 2009.

[39] I. A. Kovács and F. Iglói. Renormalization group study of the two-dimensional random transverse-field Ising model. *Phys. Rev. B*, 82(5):13, 2010.

[40] I. A. Kovács and F. Iglói. Infinite-disorder scaling of random quantum magnets in three and higher dimensions. *Phys. Rev. B*, 83(17):5, 2011.

[41] I. A. Kovács and F. Iglói. Renormalization group study of random quantum magnets. *J. Phys.: Condens. Matter*, 23(40):12, 2011.

[42] I. A. Kovács and F. Iglói. Universal logarithmic terms in the entanglement entropy of 2d, 3d and 4d random transverse-field Ising models. *Europhys. Lett.*, 97:67009, 2011.

[43] A. Pelissetto and E. Vicari. Critical phenomena and renormalization-group theory. *Physics Reports*, 368(6):549–727, 2002.

[44] S. Sachdev. Quantum criticality: Competing ground states in low dimensions. *Science*, 288(5465):475–480, 2000.

[45] T. Vojta, K. H. Hoffmann, and M. Schreiber, editors. *Computational Statistical Physics*. Springer, Berlin, 2002.

[46] D. Bitko, T. F. Rosenbaum, and G. Aeppli. Quantum critical behavior for a model magnet. *Phys. Rev. Lett.*, 77(5):940–943, 1996.

[47] P. Coleman. Theories of non-fermi liquid behavior in heavy fermions. *Physica B*, 259-61:353–358, 1999.

[48] H. von Löhneysen. Non-Fermi-liquid behaviour in the heavy-fermion system $CeCu_{6-x}Au_x$. *J. Phys.: Condens. Matter*, 8(48):9689–9706, 1996.

[49] E. Dagotto. Correlated electrons in high-temperature superconductors. *Rev. Mod. Phys.*, 66(3):763–840, 1994.

[50] M. B. Maple. High-temperature superconductivity. *J. Magn. Magn. Mater.*, 177:18–30, 1998.

[51] J. Orenstein and A. J. Millis. Advances in the physics of high-temperature superconductivity. *Science*, 288(5465):468–474, 2000.

[52] S. V. Kravchenko, W. E. Mason, G. E. Bowker, J. E. Furneaux, V. M. Pudalov, and M. Diorio. Scaling of an anomalous metal-insulator-transition in a 2-dimensional system in silicon at $B = O$. *Phys. Rev. B*, 51(11):7038–7045, 1995.

[53] S. L. Sondhi, S. M. Girvin, J. P. Carini, and D. Shahar. Continuous quantum phase transitions. *Rev. Mod. Phys.*, 69(1):315–333, 1997.

[54] S. H. S. F. S. P. Ferrel R. A., Menyhárd N. Dispersion in 2nd sound and anomalous heat conduction at lambda point of liquid helium. *Phys. Rev. Lett.*, 18:891, 1967.

[55] S. H. S. F. S. P. Ferrel R. A., Menyhárd N. Fluctuations and lambda phase transition in liquid helium. *Ann. Phys. (N.Y.)*, 47:565, 1968.

[56] B. I. Halperin and P. C. Hohenberg. Generalization of scaling laws to dynamical properties of a system near its critical point. *Phys. Rev. Lett.*, 19:700–703, 1967.

[57] R. Feynman. *Statistical Mechanics*. Addison-Wesley, Massachusetts, 1972.

[58] M. Suzuki. Relationship between d-dimensional quantal spin systems and (d+1)-dimensional Ising systems. *Progress of Theoretical Physics*, 56(5):1454–1469, 1976.

[59] M. Suzuki. *Quantum Monte Carlo Methods in Condensed Matter Physics*. World Scientific, 1993.

[60] J. L. Cardy. *Scaling and Renormalization in Statistical Physics*. Cambridge University Press, 1996.

[61] H. E. Stanley. *Introduction to phase transitions and critical phenomena*. Oxford University Press, 1987.

[62] A. Crisanti and F. Ritort. Violation of the fluctuation-dissipation theorem in glassy systems: basic notions and the numerical evidence. *J. Phys. A: Math. and Theor.*, 36(21):R181–R290, 2003.

[63] L. F. Cugliandolo. Dynamics of glassy systems. *Lecture notes, Les Houches, arXiv:cond-mat/0210312*, 2002.

[64] P. W. Anderson. Absence of diffusion in certain random lattices. *Physical Review*, 109(5):1492–1505, 1958.

[65] M. Guo, R. N. Bhatt, and D. A. Huse. Quantum critical behavior of a three-dimensional Ising spin glass in a transverse magnetic field. *Phys. Rev. Lett.*, 72(26):4137–4140, 1994.

[66] H. Rieger and A. P. Young. Zero-temperature quantum phase transition of a two-dimensional Ising spin glass. *Phys. Rev. Lett.*, 72(26):4141–4144, 1994.

[67] W. Cochran. *Advances in Physics*, 18:157, 1969.

[68] I. P. Kaminow and T. C. Damen. Temperature dependence of the ferroelectric mode in KH_2PO_4. *Phys. Rev. Lett.*, 20(20):1105–1108, 1968.

[69] K. K. Kobayashi. Dynamical theory of the phase transition in KH_2PO_4-type ferroelectric crystals. *J. Phys. Soc. Jpn.*, 24:497, 1968.

[70] G. A. Samara. Vanishing of the ferroelectric and antiferroelectric states in KH_2PO_2-type crystals at high pressure. *Phys. Rev. Lett.*, 27(2):103–106, 1971.

[71] R. Pirc, B. Tadic, and R. Blinc. Tunneling model of proton glasses. *Zeitschrift Fur Physik B-Condensed Matter*, 61(1):69–74, 1985.

[72] R. Coldea, D. A. Tennant, E. M. Wheeler, E. Wawrzynska, D. Prabhakaran, M. Telling, K. Habicht, P. Smeibidl, and K. Kiefer. Quantum criticality in an Ising chain: Experimental evidence for emergent E8 symmetry. *Science*, 327(5962):177–180, 2010.

[73] R. B. Stinchcombe. Ising model in a transverse field. I. basic theory. *J. Phys. C*, 6(15):2459–2483, 1973.

[74] J. Brooke, D. Bitko, T. F. Rosenbaum, and G. Aeppli. Quantum annealing of a disordered magnet. *Science*, 284(5415):779–781, 1999.

[75] D. H. Reich, B. Ellman, J. Yang, T. F. Rosenbaum, G. Aeppli, and D. P. Belanger. Dipolar magnets and glasses - neutron-scattering, dynamic, and calorimetric studies of randomly distributed ising spins. *Phys. Rev. B*, 42(7):4631–4644, 1990.

[76] W. H. Wu, D. Bitko, T. F. Rosenbaum, and G. Aeppli. Quenching of the nonlinear susceptibility at a $T = 0$ spin-glass transition. *Phys. Rev. Lett.*, 71(12):1919–1922, 1993.

[77] W. H. Wu, B. Ellman, T. F. Rosenbaum, G. Aeppli, and D. H. Reich. From classical to quantum glass. *Phys. Rev. Lett.*, 67(15):2076–2079, 1991.

[78] P. B. Chakraborty, P. Henelius, H. Kjonsberg, A. W. Sandvik, and S. M. Girvin. Theory of the magnetic phase diagram of LiHoF4. *Phys. Rev. B.*, 70:144411, 2004.

[79] A. Dutta, U. Divakaran, D. Sen, B. K. Chakrabarti, T. F. Rosenbaum, and G. Aeppli. Transverse field spin models: From statistical physics to quantum information. *arXiv:1012.0653*, 2010.

[80] M. Schechter. LiHo(x)Y(1-x)F(4) as a random-field Ising ferromagnet. *Phys. Rev. B*, 77(2):4, 2008.

[81] M. Schechter and P. C. E. Stamp. Correlated random fields in dielectric and spin glasses. *Europhys. Lett.*, 88(6):5, 2009.

[82] S. M. A. Tabei, M. J. P. Gingras, Y. J. Kao, P. Stasiak, and J. Y. Fortin. Induced random fields in the LiHoxY1-xF4 quantum Ising magnet in a transverse magnetic field. *Phys. Rev. Lett.*, 97(23):4, 2006.

[83] D. M. Silevitch, G. Aeppli, and T. F. Rosenbaum. Switchable hardening of a ferromagnet at fixed temperature. *Proc. Natl. Acad. Sci.*, 107(7):2797–2800, 2010.

[84] D. M. Silevitch, D. Bitko, J. Brooke, S. Ghosh, G. Aeppli, and T. F. Rosenbaum. A ferromagnet in a continuously tunable random field. *Nature*, 448(7153):567–570, 2007.

[85] F. Solomon. Random-walks in a random environment. *Annals of Probability*, 3(1):1–31, 1975.

[86] H. Kesten, M. V. Kozlov, and F. Spitzer. Limit law for random-walk in a random environment. *Compositio Mathematica*, 30(2):145–168, 1975.

[87] Y. G. Sinai. The limiting behavior of a one-dimensional random walk in a random medium. *Theory of Probability and its Applications*, 27(2):256–256, 1983.

[88] S. Alexander, J. Bernasconi, W. R. Schneider, and R. Orbach. Excitation dynamics in random one-dimensional systems. *Rev. Mod. Phys.*, 53(2):175–198, 1981.

[89] B. Derrida and Y. Pomeau. Classical diffusion on a random chain. *Phys. Rev. Lett.*, 48(9):627–630, 1982.

[90] B. Derrida. Velocity and diffusion constant of a periodic one-dimensional hopping model. *Journal of Statistical Physics*, 31(3):433–450, 1983.

[91] Z. Shi. Sinai's walk via stochastic calculus. *Soc. Math. de France*, 12:53, 2001.

[92] J. P. Bouchaud and A. Georges. Anomalous diffusion in disordered media - statistical mechanisms, models and physical applications. *Physics Reports*, 195(4-5):127–293, 1990.

[93] J. W. Haus and K. W. Kehr. Diffusion in regular and disordered lattices. *Physics Reports*, 150:263–406, 1987.

[94] S. Havlin and D. Benavraham. Diffusion in disordered media. *Advances in Physics*, 36(6):695–798, 1987.

[95] D. K. Lubensky and D. R. Nelson. Pulling pinned polymers and unzipping DNA. *Phys. Rev. Lett.*, 85(7):1572–1575, 2000.

[96] D. K. Lubensky and D. R. Nelson. Single molecule statistics and the polynucleotide unzipping transition. *Phys. Rev. E*, 65(3):031917, 2002.

[97] D. R. Nelson. Statistical physics of unzipping DNA. *Forces, Growth and Form in Soft Condensed Matter: At the Interface between Physics and Biology NATO Science Series, arXiv:cond-mat/0309559*, 160:65–92, 2005.

[98] Y. Kafri, D. K. Lubensky, and D. R. Nelson. Dynamics of molecular motors and polymer translocation with sequence heterogeneity. *Biophys. J.*, 86(6):3373–3391, 2004.

[99] I. A. Kovács. Critical and off-critical behavior of disordered quantum spin chains (rendezetlen kvantum spinláncok kritikus viselkedésének vizsgálata). Master's thesis, 2008.

[100] A. O. Golosov. Localization of random walks in one-dimensional random environments. *Communications in Mathematical Physics (1965-1997)*, 92(4):491–506, 1984.

[101] K. Binder and A. P. Young. Spin-glasses - experimental facts, theoretical concepts, and open questions. *Rev. Mod. Phys.*, 58(4):801–976, 1986.

[102] Mezard, M, Parisi, G, Virasoro, and M. *Spin Glass Theory and Beyond*. World Scientific, Singapore, 1987.

[103] A. Crisanti, G. Paladin, and A. Vulpiani. *Products of Random Matrices: in Statistical Physics*. Springer Series in Solid-State Sciences. Springer Verlag, 1993.

[104] A. P. Young, editor. *Spin glasses and random fields*, volume 12. World Scientific, Singapore, 1998.

[105] N. Kawashima and H. Rieger. *Recent progress in spin glasses*, pages 491–596. World Scientific, Singapore, 2005.

[106] F. J. Dyson. The dynamics of a disordered linear chain. *Physical Review*, 92(6):1331–1338, 1953.

[107] H. Schmidt. Disordered one-dimensional crystals. *Physical Review*, 105(2):425–441, 1957.

[108] F. Iglói and I. A. Kovács. Griffiths-McCoy singularities in random quantum spin chains: Exact results. *Phys. Rev. B*, 77(14):144203, 2008.

[109] J. Kurchan. Supersymmetry, replica and dynamic treatments of disordered systems: a parallel presentation. *arXiv:cond-mat/0209399*, 2002.

[110] K. Efetov. *Supersymmetry in Disorder and Chaos*. Cambridge University Press, 1997.

[111] J.-P. Bouchaud, L. F. Cugliandolo, J. Kurchan, and M. Mezard. Out of equilibrium dynamics in spin-glasses and other glassy systems. *arXiv:cond-mat/9702070*, 1997.

[112] A. J. Bray. Nature of the Griffiths phase. *Phys. Rev. Lett.*, 59(5):586–589, 1987.

[113] A. J. Bray. Dynamics of dilute magnets above Tc. *Phys. Rev. Lett.*, 60(8):720–723, 1988.

[114] M. Randeria, J. P. Sethna, and R. G. Palmer. Low-frequency relaxation in Ising spin-glasses. *Phys. Rev. Lett.*, 54(12):1321–1324, 1985.

[115] R. B. Griffiths. Nonanalytic behavior above the critical point in a random Ising ferromagnet. *Phys. Rev. Lett.*, 23(1):17–19, 1969.

[116] T. Vojta. Rare region effects at classical, quantum and nonequilibrium phase transitions. *J. Phys. A: Math. and Gen.*, 39(22):R143–R205, 2006.

[117] M. Bramson, R. Durrett, and R. H. Schonmann. The contact process in a random environment. *Annals of Probability*, 19(3):960–983, 1991.

[118] R. Cafiero, A. Gabrielli, and M. A. Muñoz. Disordered one-dimensional contact process. *Phys. Rev. E*, 57(5):5060–5068, 1998.

[119] R. Dickman and A. G. Moreira. Violation of scaling in the contact process with quenched disorder. *Phys. Rev. E*, 57(2):1263–1268, 1998.

[120] H. K. Janssen. Renormalized field theory of the Gribov process with quenched disorder. *Phys. Rev. E*, 55(5):6253–6256, 1997.

[121] A. G. Moreira and R. Dickman. Critical dynamics of the contact process with quenched disorder. *Phys. Rev. E*, 54(4):R3090–R3093, 1996.

[122] A. J. Noest. New universality for spatially disordered cellular automata and directed percolation. *Phys. Rev. Lett.*, 57(1):90–93, 1986.

[123] I. Webman, D. Ben-Avraham, A. Cohen, and S. Havlin. Dynamical phase transitions in a random environment. *Philosophical Magazine B*, 77(5):1401–1412, 1998.

[124] B. M. McCoy. Incompleteness of the critical exponent description for ferromagnetic systems containing random impurities. *Phys. Rev. Lett.*, 23(7):383–386, 1969.

[125] T. M. Nieuwenhuizen. Griffiths singularities in two-dimensional random-bond Ising-models - relation with Lifshitz band tails. *Phys. Rev. Lett.*, 63(17):1760–1763, 1989.

[126] I. M. Lifshitz. The energy spectrum of disordered systems. *Advances in Physics*, 13(52):483–536, 1964.

[127] I. M. Lifshitz. Energy spectrum and quantum states of disordered condensed systems. *Sov. Phys. Usp. 7*, 7:549, 1965.

[128] I. M. Lifshitz, S. A. Gredeskul, and L. A. Pastur. *Introduction to the Theory of Disordered Systems*. John Wiley and Sons, 1988.

[129] T. Vojta. Quantum Griffiths effects and smeared phase transitions in metals: Theory and experiment. *J. Low Temp. Phys.*, 161(1):299–323, 2010.

[130] T. Vojta and J. A. Hoyos. Smeared quantum phase transition in the dissipative random quantum Ising model. *Physica E*, 42(3):383–387, 2010.

[131] F. Vazquez, J. A. Bonachela, C. López, and M. A. Muñoz. Temporal griffiths phases. *Phys. Rev. Lett.*, 106(23):235702, 2011.

[132] Y. Imry. Random external fields. *Journal of Statistical Physics*, 34(5-6):849–862, 1984.

[133] A. Aharony, Y. Imry, and S. K. Ma. Lowering of dimensionality in phase-transitions with random fields. *Phys. Rev. Lett.*, 37(20):1364–1367, 1976.

[134] J. Villain. Failure of perturbation-theory in random field models. *J. Phys. A: Math. and Gen.*, 21(22):L1099–L1105, 1988.

[135] G. Parisi and N. Sourlas. Random magnetic fields, supersymmetry, and negative dimensions. *Phys. Rev. Lett.*, 43(11):744–745, 1979.

[136] J. Bricmont and A. Kupiainen. Lower critical dimension for the random-field Ising-model. *Phys. Rev. Lett.*, 59(16):1829–1832, 1987.

[137] J. Z. Imbrie. Lower critical dimension of the random-field Ising-model. *Phys. Rev. Lett.*, 53(18):1747–1750, 1984.

[138] M. Aizenman and J. Wehr. Rounding of first-order phase transitions in systems with quenched disorder. *Phys. Rev. Lett.*, 62(21):2503–2506, 1989.

[139] J. T. Chayes, L. Chayes, D. S. Fisher, and T. Spencer. Finite-size scaling and correlation lengths for disordered-systems. *Phys. Rev. Lett.*, 57(24):2999–3002, 1986.

[140] A. B. Harris. Effect of random defects on the critical behaviour of Ising models. *J. Phys. C*, 7(9):1671, 1974.

[141] D. S. Fisher. Sliding charge-density waves as a dynamic critical phenomenon. *Phys. Rev. B*, 31(3):1396–1427, 1985.

[142] J. Priour, D. J. and S. Das Sarma. Critical behavior of diluted magnetic semiconductors: Apparent violation and eventual restoration of the Harris criterion for all regimes of disorder. *Phys. Rev. B*, 81(22):224403, 2010.

[143] D. X. Yao, J. Gustafsson, E. W. Carlson, and A. W. Sandvik. Quantum phase transitions in disordered dimerized quantum spin models and the Harris criterion. *Phys. Rev. B*, 82(17):4, 2010.

[144] L. P. Kadanoff. Notes on Migdal's recursion formulas. *Annals of Physics*, 100:359–394, 1976.

[145] A. A. Migdal. Phase transitions in gauge and spin-lattice systems. *Soviet Journal of Experimental and Theoretical Physics*, 42:743–743, 1975.

[146] W. Kinzel and E. Domany. Critical properties of random Potts models. *Phys. Rev. B*, 23(7):3421–3434, 1981.

[147] C. Jayaprakash, E. K. Riedel, and M. Wortis. Critical and thermodynamic properties of randomly dilute Ising-model. *Phys. Rev. B*, 18(5):2244–2255, 1978.

[148] J. E. Hirsch. Low-temperature thermodynamic properties of a random anisotropic antiferromagnetic chain. *Phys. Rev. B*, 22(11):5355–5365, 1980.

[149] J. E. Hirsch and J. V. Jose. Low-temperature thermodynamic properties of a random heisenberg anti-ferromagnetic chain ($S = 1/2$). *J. Phys. C*, 13(3):L53–L60, 1980.

[150] J. E. Hirsch and J. V. Jose. Singular thermodynamic properties in random magnetic chains. *Phys. Rev. B*, 22(11):5339–5354, 1980.

[151] J. Hooyberghs. *A renormalization group study of one-dimensional contact processes*. PhD thesis, Limburgs Universitair Centrum, 2002.

[152] T. Aspelmeier, A. J. Bray, and M. A. Moore. Why temperature chaos in spin glasses is hard to observe. *Phys. Rev. Lett.*, 89(19):4, 2002.

[153] H. Bokil, B. Drossel, and M. A. Moore. Influence of critical behavior on the spin-glass phase. *Phys. Rev. B*, 62(2):946–951, 2000.

[154] A. J. Bray and S. Feng. Percolation of order in frustrated systems: The dilute +/-J spin glass. *Phys. Rev. B*, 36(16):8456–8460, 1987.

[155] B. Drossel, H. Bokil, M. A. Moore, and A. J. Bray. The link overlap and finite size effects for the 3D Ising spin glass. *Eur. Phys. J. B*, 13(2):369–375, 2000.

[156] B. Drossel and M. A. Moore. The +/- J spin glass in Migdal-Kadanoff approximation. *Eur. Phys. J. B*, 21(4):589–594, 2001.

[157] A. J. B. Moore and M. A. Lower critical dimension of Ising spin glasses: a numerical study. *J. Phys. C*, 17(18):L463, 1984.

[158] M. A. Moore, H. Bokil, and B. Drossel. Evidence for the droplet picture of spin glasses. *Phys. Rev. Lett.*, 81(19):4252–4255, 1998.

[159] M. Sasaki and O. C. Martin. Temperature chaos, rejuvenation, and memory in Migdal-Kadanoff spin glasses. *Phys. Rev. Lett.*, 91(9):4, 2003.

[160] B. Southern and A. P. Young. Real space rescaling study of spin glass behaviour in three dimensions. *J. Phys. C*, 10:2179, 1977.

[161] M. J. Thill and H. J. Hilhorst. Theory of the critical state of low-dimensional spin glass. *Journal De Physique I*, 6(1):67–95, 1996.

[162] A. P. Young and R. B. Stinchcombe. Real-space renormalization group calculations for spin-glasses and dilute magnets. *J. Phys. C*, 9(24):4419–4431, 1976.

[163] J. R. Banavar and A. J. Bray. Chaos in spin-glasses - a renormalization-group study. *Phys. Rev. B*, 35(16):8888–8890, 1987.

[164] A. J. Bray and M. A. Moore. Chaotic nature of the spin-glass phase. *Phys. Rev. Lett.*, 58(1):57–60, 1987.

[165] S. R. McKay, A. N. Berker, and S. Kirkpatrick. Spin-glass behavior in frustrated Ising-models with chaotic renormalization-group trajectories. *Phys. Rev. Lett.*, 48(11):767–770, 1982.

[166] M. Ney-Nifle and H. J. Hilhorst. Chaos exponents in spin-glasses. *Physica A*, 193(1):48–78, 1993.

[167] M. Ney-Nifle and H. J. Hilhorst. Renormalization theory and chaos exponents in random-systems. *Physica A*, 194(1-4):462–470, 1993.

[168] M. Nifle and H. J. Hilhorst. New critical-point exponent and new scaling laws for short-range Ising spin-glasses. *Phys. Rev. Lett.*, 68(20):2992–2995, 1992.

[169] D. S. Fisher. Interface fluctuations in disordered-systems - 5-epsilon expansion and failure of dimensional reduction. *Phys. Rev. Lett.*, 56(18):1964–1967, 1986.

[170] D. Carpentier and P. Le Doussal. Disordered XY models and coulomb gases: Renormalization via traveling waves. *Phys. Rev. Lett.*, 81(12):2558–2561, 1998.

[171] D. S. Fisher and D. A. Huse. Ordered phase of short-range Ising spin-glasses. *Phys. Rev. Lett.*, 56(15):1601–1604, 1986.

[172] D. S. Fisher and D. A. Huse. Equilibrium behavior of the spin-glass ordered phase. *Phys. Rev. B*, 38(1):386–411, 1988.

[173] D. S. Fisher and D. A. Huse. Nonequilibrium dynamics of spin glasses. *Phys. Rev. B*, 38(1):373–385, 1988.

[174] W. L. McMillan. Scaling theory of Ising spin-glasses. *J. Phys. C*, 17(18):3179–3187, 1984.

[175] A. J. Bray and M. A. Moore. *Scaling theory of the ordered phase of spin glasses*, volume 275. Springer Verlag, 1986.

[176] C. Dasgupta and S. Ma. Low-temperature properties of the random Heisenberg antiferromagnetic chain. *Phys. Rev. B*, 22(3):1305–1319, 1980.

[177] S. K. Ma, S., C. Dasgupta, and C. K. Hu. Random anti-ferromagnetic chain. *Phys. Rev. Lett.*, 43(19):1434–1437, 1979.

[178] D. S. Fisher. Random antiferromagnetic quantum spin chains. *Phys. Rev. B*, 50(6):3799–3821, 1994.

[179] J. B. Kogut. Introduction to lattice gauge-theory and spin systems. *Rev. Mod. Phys.*, 51(4):659–713, 1979.

[180] P. Pfeuty. Exact result for the 1D random Ising-model in a transverse field. *Phys. Lett. A*, 72(3):245–246, 1979.

[181] F. Iglói. Exact renormalization of the random transverse-field Ising spin chain in the strongly ordered and strongly disordered Griffiths phases. *Phys. Rev. B*, 65(6), 2002.

[182] F. Iglói and H. Rieger. Density profiles in random quantum spin chains. *Phys. Rev. Lett.*, 78(12):2473–2476, 1997.

[183] F. Iglói and H. Rieger. Random transverse Ising spin chain and random walks. *Phys. Rev. B*, 57(18):11404–11420, 1998.

[184] A. P. Young and H. Rieger. Numerical study of the random transverse-field Ising spin chain. *Phys. Rev. B*, 53(13):8486–8498, 1996.

[185] E. W. Dijkstra. A note on two problems in connexion with graphs. *Numerische Mathematik*, 1(1):269–271, 1959.

[186] I. A. Kovács. `http://people.bolyai.elte.hu/~steve3281/thesis/`.

[187] E. Altman, Y. Kafri, A. Polkovnikov, and G. Refael. Phase transition in a system of one-dimensional bosons with strong disorder. *Phys. Rev. Lett.*, 93(15):4, 2004.

[188] E. Altman, Y. Kafri, A. Polkovnikov, and G. Refael. Superfluid-insulator transition of disordered bosons in one dimension. *Phys. Rev. B*, 81(17):16, 2010.

[189] S. Iyer, D. Pekker, and G. Refael. A Mott glass to superfluid transition for random bosons in two dimensions. *arXiv:1110.3338*, 2011.

[190] R. Dickman. *Nonequilibrium statistical mechanics in one dimension*. Cambridge University Press, 1997.

[191] P. Grassberger and A. de la Torre. Reggeon field-theory (Schlogl 1st model) on a lattice - Monte-Carlo calculations of critical behavior. *Ann. Phys. (N.Y.)*, 122:373, 1979.

[192] R. Ziff, E. Gulari, and Y. Barshad. Kinetic phase transitions in an irreversible surface-reaction model. *Phys. Rev. Lett.*, 56:2553, 1986.

[193] A. Barabási and H. Stanley. *Fractal concepts in surface growth*. Cambridge University Press, 1995.

[194] A. Daerr and S. Douady. Two types of avalanche behaviour in granular media. *Nature*, 399:241, 1999.

[195] H. Hinrichsen, A. Jimenez-Dalmaroni, Y. Rozov, and E. Domany. Flowing sand: A physical realization of directed percolation. *Phys. Rev. Lett.*, 83:4999, 1999.

[196] K. A. Takeuchi, M. Kuroda, H. Chaté, and M. Sano. Directed percolation criticality in turbulent liquid crystals. *Phys. Rev. Lett.*, 99(23):234503, 2007.

[197] H. Hinrichsen. On possible experimental realizations of directed percolation. *Braz. J. Phys.*, 30:69–82, 2000.

[198] J. A. Hoyos. Weakly disordered absorbing-state phase transitions. *Phys. Rev. E*, 78:032101, 2008.

[199] M. Kafatos, editor. *Bell's Theorem, Quantum Theory and Conceptions of the Universe*. Springer, 1989.

[200] C. F. Majkrzak, J. Kwo, M. Hong, Y. Yafet, D. Gibbs, C. L. Chien, and J. Bohr. Magnetic rare-earth superlattices. *Advances in Physics*, 40(2):99–189, 1991.

[201] E. Dagotto and T. Rice. Surprises on the way from one- to two-dimensional quantum magnets: The ladder materials. *Science*, 271(5249):618–623, 1996.

[202] M. E. Fisher and M. N. Barber. Scaling theory for finite-size effects in the critical region. *Phys. Rev. Lett.*, 28(23):1516–1519, 1972.

[203] N. M. Barber. *Phase Transitions and Critical Phenomena*, volume 8. Academic Press, New York, 1983.

[204] E. P. and R. A. *Publicationes Mathematicae*, 6:290, 1959.

[205] F. Pazmandi, R. Scalettar, and G. Zimanyi. Revisiting the theory of finite size scaling in disordered systems: nu can be less than 2/d. *Phys. Rev. Lett.*, 79(25):5130–5133, 1997.

[206] S. Wiseman and E. Domany. Finite-size scaling and lack of self-averaging in critical disordered systems. *Phys. Rev. Lett.*, 81(1):22–25, 1998.

[207] S. Wiseman and E. Domany. Self-averaging, distribution of pseudocritical temperatures, and finite size scaling in critical disordered systems. *Phys. Rev. E*, 58(3):2938–2951, 1998.

[208] A. Aharony, A. Harris, and S. Wiseman. Critical disordered systems with constraints and the inequality $\nu > 2/d$. *Phys. Rev. Lett.*, 81(2):252–255, 1998.

[209] K. Bernardet, F. Pazmandi, and G. Batrouni. Disorder averaging and finite-size scaling. *Phys. Rev. Lett.*, 84(19):4477–4480, 2000.

[210] M. T. Mercaldo, J. C. A. d'Auriac, and F. Iglói. Disorder-induced rounding of the phase transition in the large-q-state Potts model. *Phys. Rev. E*, 69(5), 2004.

[211] C. Monthus and T. Garel. Distribution of pseudo-critical temperatures and lack of self-averaging in disordered Poland-Scheraga models with different loop exponents. *Eur. Phys. J. B*, 48(3):393–403, 2005.

[212] F. Iglói, Y.-C. Lin, H. Rieger, and C. Monthus. Finite-size scaling of pseudocritical point distributions in the random transverse-field Ising chain. *Phys. Rev. B*, 76(6), 2007.

[213] E. Lieb, T. Schultz, and D. Mattis. Two soluble models of an antiferromagnetic chain. *Annals of Physics*, 16(3):407–466, 1961.

[214] A. A. D. Stauffer, editor. *Introduction to Percolation Theory*. Taylor and Francis, London, 1992.

[215] R. Juhász and Y. C. Lin. Strong Griffiths singularities in random systems and their relation to extreme value statistics. *Phys. Rev. B*, 73(22):10, 2006.

[216] J. Galambos. *The Asymptotic Theory of Extreme Order Statistics*. John Wiley & Sons, New York, 1978.

[217] P. B. Chakraborty, P. Henelius, H. Kjonsberg, A. W. Sandvik, and S. M. Girvin. Theory of the magnetic phase diagram of LiHoF4. *Phys. Rev. B*, 70(14):14, 2004.

[218] M. A. Muñoz, R. Juhász, C. Castellano, and G. Ódor. Griffiths phases on complex networks. *Phys. Rev. Lett.*, 105(12):4, 2010.

[219] P. Calabrese, J. Cardy, and B. Doyon. Entanglement entropy in extended quantum systems. *J. Phys. A: Math. and Theor.*, 42(50):500301–500301, 2009.

[220] P. Calabrese and J. Cardy. Entanglement entropy and conformal field theory. *J. Phys. A: Math. and Theor.*, 42(50):36, 2009.

[221] P. Calabrese and A. Lefevre. Entanglement spectrum in one-dimensional systems. *Phys. Rev. A*, 78(3), 2008.

[222] J. Eisert, M. Cramer, and M. B. Plenio. Colloquium: Area laws for the entanglement entropy. *Rev. Mod. Phys.*, 82(1):277–306, 2010.

[223] T. Barthel, M. C. Chung, and U. Schollwöck. Entanglement scaling in critical two-dimensional fermionic and bosonic systems. *Phys. Rev. A*, 74(2), 2006.

[224] M. Cramer, J. Eisert, and M. B. Plenio. Statistics dependence of the entanglement entropy. *Phys. Rev. Lett.*, 98(22), 2007.

[225] M. M. Wolf. Violation of the entropic area law for fermions. *Phys. Rev. Lett.*, 96(1), 2006.

[226] D. Gioev and I. Klich. Entanglement entropy of fermions in any dimension and the Widom conjecture. *Phys. Rev. Lett.*, 96(10), 2006.

[227] L. Tagliacozzo, G. Evenbly, and G. Vidal. Simulation of two-dimensional quantum systems using a tree tensor network: entropic area law at work. *Phys. Rev. B*, 80:235127, 2009.

[228] H. F. Song, N. Laflorencie, S. Rachel, and K. Le Hur. Entanglement entropy of the two-dimensional Heisenberg antiferromagnet. *Phys. Rev. B*, 83(22), 2011.

[229] A. B. Kallin, M. B. Hastings, R. G. Melko, and R. R. P. Singh. Anomalies in the entanglement properties of the square lattice Heisenberg model. *Phys. Rev. B*, 84:165134, 2011.

[230] D. S. Rokhsar and S. A. Kivelson. Superconductivity and the quantum hard-core dimer gas. *Phys. Rev. Lett.*, 61(20):2376–2379, 1988.

[231] E. Fradkin and J. E. Moore. Entanglement entropy of 2D conformal quantum critical points: Hearing the shape of a quantum drum. *Phys. Rev. Lett.*, 97(5), 2006.

[232] J.-M. Stéphan, S. Furukawa, G. Misguich, and V. Pasquier. Shannon and entanglement entropies of one- and two-dimensional critical wave functions. *Phys. Rev. B*, 80(18):184421, 2009.

[233] M. P. Zaletel, J. H. Bardarson, and J. E. Moore. Logarithmic terms in entanglement entropies of 2D quantum critical points and shannon entropies of spin chains. *Phys. Rev. Lett.*, 107(1), 2011.

[234] G. Refael and J. E. Moore. Criticality and entanglement in random quantum systems. *J. Phys. A: Math. and Theor.*, 42(50):31, 2009.

[235] N. Laflorencie. Scaling of entanglement entropy in the random singlet phase. *Phys. Rev. B*, 72(14), 2005.

[236] F. Iglói and Y.-C. Lin. Finite-size scaling of the entanglement entropy of the quantum Ising chain with homogeneous, periodically modulated and random couplings. *J. Stat. Mech.*, 2008.

[237] J. Sólyom and P. Pfeuty. Renormalization-group study of the hamiltonian version of the potts model. *Phys. Rev. B*, 24:218, 1981.

[238] P. R. Elitzur S. and S. J. Phase structure of discrete abelian spin and gauge systems. *Phys. Rev. D*, 19:3698, 1979.

[239] D. A. Abanin and E. Demler. Measuring entanglement entropy of a generic many-body system with a quantum switch. *arXiv:1204.2819v1*, 2012.

[240] T. Senthil and S. Sachdev. Higher dimensional realizations of activated dynamic scaling at random quantum transitions. *Phys. Rev. Lett.*, 77(26):5292–5295, 1996.

[241] F. Iglói, Z. Szatmári, and Y.-C. Lin. Entanglement entropy dynamics of disordered quantum spin chains. *Phys. Rev. B.*, 85:094417, 2012.

[242] C. Monthus and T. Garel. Random transverse field Ising model in dimensions $d = 2, 3$: infinite disorder scaling via a non-linear transfer approach. *Journal of Statistical Mechanics: Theory and Experiment*, 2012(01):P01008–P01008, 2012.

[243] M. Karsai, I. A. Kovács, J. C. Angles d'Auriac, and F. Iglói. Density of critical clusters in strips of strongly disordered systems. *Phys. Rev. E*, 78(6):061109, 2008.

[244] C. Monthus and T. Garel. Random transverse field Ising model in dimension $d > 1$: scaling analysis in the disordered phase from the directed polymer model. *J. Phys. A: Math. and Theor.*, 45(9):095002–095002, 2012.

[245] C. Monthus and T. Garel. Strong disorder RG principles within a fixed cell-size real space renormalization : application to the random transverse field Ising model on various fractal lattices. *arXiv:1201.6136*, 2012.

[246] C. R. Laumann, D. A. Huse, A. W. W. Ludwig, G. Refael, S. Trebst, and T. M. Strong-disorder renormalization for interacting non-abelian anyon systems in two dimensions. *arxiv:1203.3752*, 2012.

[247] I. Benjamini and N. Berger. The diameter of long-range percolation clusters on finite cycles. *Random Structures and Algorithms*, 19(2):102–111, 2001.

[248] O. Dimitrova and M. Mezard. The cavity method for quantum disordered systems: from transverse random field ferromagnets to directed polymers in random media. *J. Stat. Mech.*, page 22, 2011.

[249] L. B. Ioffe and M. Mezard. Disorder-driven quantum phase transitions in superconductors and magnets. *Phys. Rev. Lett.*, 105(3):4, 2010.

[250] M. V. Feigel'man, L. B. Ioffe, and M. Mézard. Superconductor-insulator transition and energy localization. *Phys. Rev. B*, 82(18):184534, 2010.

[251] R. Mélin, B. Doucot, and F. Iglói. Strong-disorder renormalization-group method on fractal lattices: Heisenberg models and magnetoresistive effects in tight-binding models. *Phys. Rev. B*, 72(2):17, 2005.

Acknowledgments

First of all, I would like to express my gratitude to my supervisor, Prof. Ferenc Iglói, for his valuable guidance over the last years. His deep physical insight and clear thinking had a great educational effect on me. I am also very grateful to my internal advisor, Prof. Péter Szépfalusy for his continuous support.

I am indebted to Prof. Heiko Rieger for his warm hospitality and influential discussions during my stays in Saarbrücken.

I am grateful to Péter Hartmann, who helped me to initialize our computer cluster, on which the vast majority of the calculations was carried out.

I thank to Róbert Juhász, Gábor Szuromi, Zoltán Zimborás, Prof. Yu-Cheng Lin for useful discussions and Prof. Naoki Kawashima and Prof. David Huse for helpful correspondence.

I highly appreciate the financial support provided by the Hungarian National Research Fund under grant No OTKA K62588, K75324 and K77629 and by a German-Hungarian exchange program (DFG-MTA).

Last, but not least I appreciate the support and the understanding of my family and friends.

Abstract

In this thesis we studied the critical behavior of the random transverse-field Ising model (RTIM) in higher dimensional systems. Using our very efficient numerical algorithm of the strong disorder renormalization group method we have extended the investigations about the critical behavior of the RTIM in the previously unexplored three and four dimensional lattices, as well as for Erdős-Rényi random graph, which represents the infinite dimensional lattice. In all studied cases an infinite disorder quantum critical point is identified, which ensures that the applied method is asymptotically correct and the calculated critical exponents tend to the exact values for large scales.

The main results of our investigations are the following. We have extended the finite-size scaling study for pseudo-critical points and from their distribution we have obtained precise estimate for the correlation length critical exponent, which has been shown to govern both the shift and the width of the distribution. We have obtained accurate estimates also for the magnetization and dynamical critical exponents and systematically studied — at the first time in higher dimensions — the behavior of scaling functions, both at the critical point and in the vicinity of the critical point. We have found that the critical exponents are independent of the form of (ferromagnetic) disorder - thus universal - and they vary smoothly with the dimensionality. Consequently, infinitely disordered critical behavior is expected in any dimensions for strong enough initial disorder.

We have also calculated the entanglement entropy of the RTIM in 2D, 3D and 4D hypercubic lattices for different shapes of the subregion. According to our results, the area law is always satisfied, but there are analytic corrections due to E-dimensional edges ($1 \leq E \leq d-2$). More interesting is the contribution arising from corners, which is logarithmically divergent at the critical point and its prefactor in a given dimension is universal, i.e. independent of the form of disorder.

Összefoglalás

Doktori értekezésemben a merőleges terű Ising modell kritikus viselkedését tanulmányoztam magasabb dimenziós rendszerekben. Az erősen rendezetlen renormálási csoport technika általam kidolgozott hatékony változatát alkalmazva kiterjesztettem a korábbi vizsgálatokat a feltáratlan 3 és 4 dimenziós eseten túl Erdős-Rényi véletlen gráfokra is, amelyek a végtelen dimenziós rácsnak feleltethetők meg. Minden említett esetben végtelenül rendezetlen kvantumfázisátalakulást találtam, ami biztosítja az alkalmazott módszer aszimptotikus korrektségét, azaz a kritikus exponenseknek az egzakt értékekhez való tartását nagy méretekre.

Főbb eredményeim a következők. Kiterjesztettem a véges-méret skálázást a mintafüggő kritikus pontokra, amelyeknek az eloszlásából pontos értékeket kaptam a korrelációs hossz kritikus exponensre, ami leírja az eloszlások eltolódásán túl a szélességük skálázását is. Azon túl, hogy a mágnesezettségi és a dinamikai kritikus exponensre is pontos értékeket kaptam, a kritikus pont környezetében elvégeztem a skálafüggvények első szisztematikus vizsgálatát is magasabb dimenzióban. Azt találtam, hogy a kritikus exponensek az univerzalitásuk jeleként függetlenek az alkalmazott (ferromágneses) rendezetlenség alakjától, valamint folytonosan változnak a dimenziók számának növekedtével. Következésképpen, tetszőleges dimenziós rácsokon is végtelenül rendezetlen kritikus viselkedést várunk, elegendően erős kezdeti rendezetlenség esetén.

Az eddigieken túl, különböző alakú részrendszerek összefonódási entrópiáját is meghatároztam 2, 3 és 4 dimenziós köbös rácsokon. Eredményeim szerint minden esetben teljesül a felületi törvény, amihez analitikus korrekciók járulnak a részrendszer E dimenziós élei ($1 \leq E \leq d-2$) következtében. Ezeknél is érdekesebb azonban a sarkok járuléka, ami logaritmikusan divergál a kritikus pontban, univerzális, a rendezetlenség alakjától független előfaktorral.